AD 730 577

Microwave Laboratory

W. W. HANSEN LABORATORIES OF PHYSICS

STANFORD UNIVERSITY · STANFORD · CALIFORNIA

TUNABLE LIGHT SCATTERING FROM

TRANSVERSE OPTICAL MODES

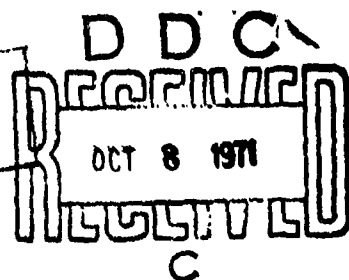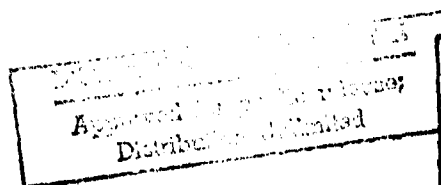IN LITHIUM NIOBATE

by

S. S. Sussman

M. L. Report No. 1851

Technical Report

Contract No. N00014(67-A-0112)0039

April 1970

Microwave Laboratory
W. W. Hansen Laboratories of Physics
Stanford University
Stanford, California

ERRATA

FOR

TUNABLE LIGHT SCATTERING FROM
TRANSVERSE OPTICAL MODES
IN LITHIUM NIOBATE

by

S. S. Sussman

M. L. Report No. <u>1851</u>

<u>Page</u>

39   Equation (3.23) (and the equation following): The right hand
term should read: ......+ $\alpha_1 \langle n_i \rangle v_i$.

Equation (3.24) -- Replace α with α_i so that the expression
should read:

$$\langle n_i \rangle \ = \ \frac{v_s}{v_i} \left(\frac{\varepsilon_3}{\varepsilon_1 + \alpha_i} \right) \langle n_s \rangle \qquad .$$

96   Equation (B.3) -- should read as follows:

$$\varepsilon_s = \frac{\omega_s |A_p|^2}{c\omega_i \eta_s} \left[\frac{1}{\sum_j \frac{\Gamma_i \Omega_{p_j}^2}{(\omega_{0_j}^2 - \omega_i^2)^2}} \right] \left(d_E' + \sum_j \frac{\Omega_{p_j}^2 \ d_{Q_j}'}{\omega_{0_j}^2 - \omega_i^2} \right)^2$$

$$\omega_{0_j} + \Gamma_j < \omega_i < \omega_{0_j} - \Gamma_j$$

ABSTRACT

This work is concerned with tunable light scattering from optical modes in crystals. The motivation for this study is the generation of tunable optical and infrared emission, an improved understanding of the scattering process, and a study of material properties.

The process involved is a combination of the Raman and parametric effects in a crystal with infrared absorbing optical modes. The input (pump) photon excites a lattice vibration and a signal photon is emitted at the difference frequency between the pump photon and the lattice vibration. Simultaneously, idler radiation is generated at the vibration frequency due to the infrared activity of the scattering optical mode. The dispersion of the idler propagation characteristic produces tuning of the signal and idler radiation as the angle between the pump and signal beam is varied.

A classical analysis of the stimulated process is presented. The analysis uses an energy density formulation and follows the approach of Henry and Garrett. The contribution of the present work in this regard is to extend their results to multimode materials and to derive a gain expression which is valid for all idler frequencies. A quantum mechanical analysis of the spontaneous scattering process is given. Expressions for the scattered signal and idler powers are derived and techniques for computing the material nonlinear coefficients are presented. Since the experiments performed in this study involved interactions with the transverse optical modes of lithium niobate ($LiNbO_3$), the results of these calculations are applied in detail to this case.

The most significant experimental results of this work were obtained in stimulated scattering from the 248 cm^{-1} mode in $LiNbO_3$. A 1 MW Q-switched ruby laser was used as a pump, and tunable stimulated signal and idler outputs were observed without the use of an external resonator. The crystal surfaces were polished flat and parallel to each other to provide for several passes of the signal radiation

- iii -

through the pump beam. Tuning was obtained simply by rotating the normal to the crystal surfaces with respect to the pump beam. Conversion efficiencies of the pump to the signal of greater than 50% were measured. While the tuning range of the signal was relatively small (6965 Å - 7045 Å), the idler wavelength was tuned from 50 μ to 250 μ, with a peak power output of about 5 watts. The experimental results were found to be in reasonable agreement with predicted values.

Spontaneous scattering measurements were also performed. A significant part of the experimental effort in this area was devoted to the construction of an argon laser and the assembly of a phase-sensitive detection system. This scattering test set is adaptable to a wide variety of spontaneous scattering experiments. It was used to investigate the properties of the spontaneously scattered signal power which is generated in scattering from the 248 cm^{-1} mode in LiNbO$_3$. The frequency and magnitude of the signal were measured as a function of the scattering angle. Again, the results were found to agree closely with calculations.

ACKNOWLEDGEMENTS

To my mother and late father, I express my appreciation for their unwavering devotion and encouragement in all of my endeavors.

Finally, I acknowledge the contributions of my wife, Steffi, whose love, understanding and inspiration made the frustrating moments more bearable and the successful times more rewarding, and my daughter, Sharon, who was a source of pleasant diversion and enrichment during the Stanford years.

TABLE OF CONTENTS

LIST OF FIGURES

CHAPTER I

INTRODUCTION

A. OBJECT OF THIS WORK

The object of this work is the study of tunable light
scattering from optical modes in crystals. The motivation for
this effort is the generation of tunable optical and infrared
emission, an improved understanding of the scattering process, and
a study of material properties. Spontaneous and stimulated scat-
tering are analyzed theoretically and the results of these calcula-
tions are compared to experimental observations. The analysis and
experiments are specifically concerned with interactions with the
transverse optical modes of lithium niobate $(LiNbO_3)$.

B. HISTORICAL BACKGROUND

The pioneering study of this type of light scattering was done
in 1928 by Raman and Krishnan.[1] They observed that a small fraction
of the light transmitted through liquids and gases emerged with a
frequency shifted from that of the incident source by the vibrational
resonant frequency of the scattering medium. This phenomenon is
called the Raman effect. The stimulated Raman effect was discovered
unexpectedly in 1962 by Woodbury and Ng,[2] in the output of a Q-
switched ruby laser. This discovery was quickly followed by the
observation of stimulated Raman emission from other materials[3-6] and
the theoretical explanation of the effect was soon developed.[3,7-10]

C. TUNABLE RAMAN SCATTERING

Raman and parametric scattering are examples of processes in
which an input wave (pump), passing through a material, generates
waves at new frequencies (signal and idler). Conservation of energy

requires that $\omega_p = \omega_s + \omega_i$, where ω is the frequency and p ,
s , and i refer to pump, signal and idler respectively. Materials
which exhibit this property are in a class of materials which is
termed nonlinear.

In parametric scattering, the idler wave is purely electro-
magnetic in nature and the nonlinearity which produces the signal polari-
zation is due solely to the motion of electrons in the material, since,
in general, the idler frequency is far above the highest vibrational
resonant frequency. This process produces radiation at both signal
and idler.

In nontunable Raman scattering, the idler frequency corresponds
to a vibrational resonance of the nonlinear material. The idler wave
consists of a mechanical vibration and the nonlinearity associated with
the signal polarization is due to ionic motion. Therefore, radiation
is generated at only the signal frequency. Vibrations which exhibit
this effect are termed Raman active.

If separation of electrical charge occurs during the optical
vibration of a crystal lattice, a dipole moment at the vibration fre-
quency is generated. The material can then both absorb and generate
electromagnetic radiation at this frequency and is called infrared
active. (The optical vibrations are at infrared frequencies.) The
dispersion curve for an infrared active crystal is strongly affected
by this coupling between electromagnetic radiation and the optical modes
of the material.[11] The dispersion curve, which is shown in Fig. 1.1,
is partly phonon-like, partly photon-like, and partly phonon-photon-
like.[12,13] The quanta associated with the mixed system are sometimes
called polaritons.[14]

The possibility of generating tunable radiation from materials
which are simultaneously infrared and Raman active was suggested inde-
pendently by Loudon[15] and Pantell and Puthoff.[16] Briefly stated, the
tuning is accomplished by controlling the idler propagation constant
k , which, in turn, determines the idler frequency through the disper-
sion curve. As the propagation constant is varied, the idler frequency
moves from the phonon-like region of the dispersion curve (near the
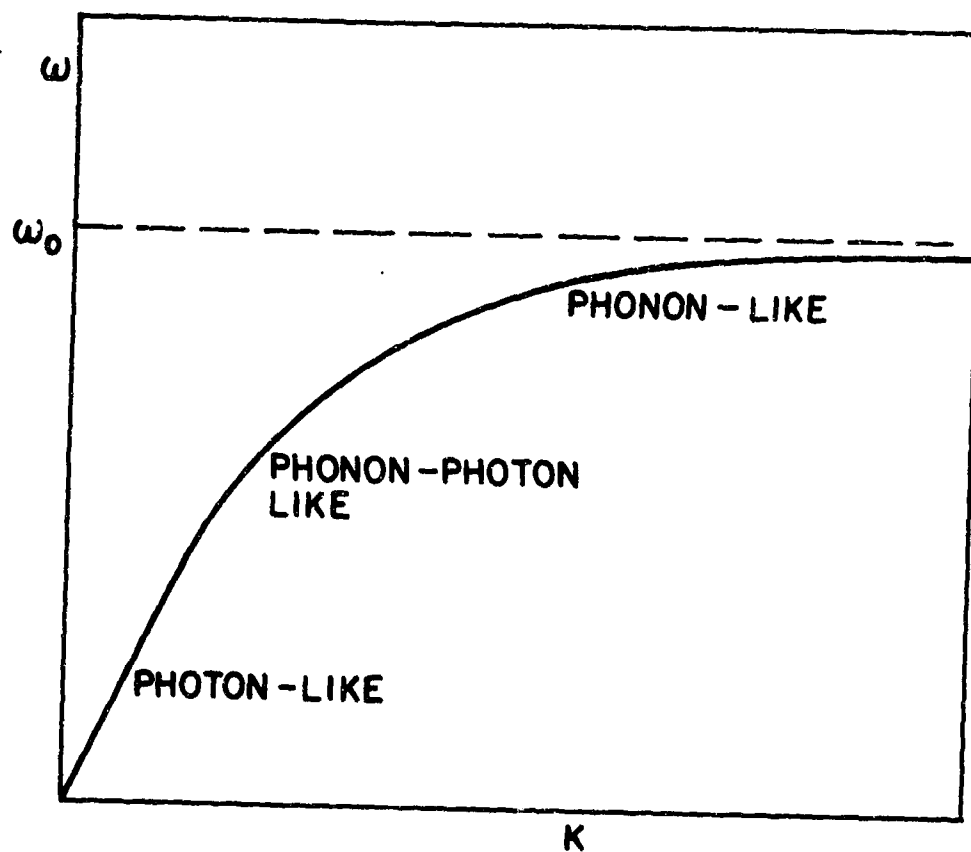
FIG. 1.1--Dispersion curve of an infrared active optical vibrational mode of a crystal, in the region below the vibrational resonant frequency, ω_0 ; k is the wave propagation constant.

resonant frequency) to a mixed region, where the idler wave is both mechanical and electromagnetic in nature. In this region, both electronic and vibrational nonlinearities can contribute to the process, and radiation at both signal and idler frequencies is generated. The idler propagation constant is varied by adjusting the angle between the pump and signal beams which, through wave vector conservation, controls the idler propagation constant. Thus, tunable signal and idler outputs can be obtained in interactions with crystal vibrations which are Raman and infrared active.

D. SUMMARY OF RESEARCH EFFORT

At the inception of the experimental program, stimulated scattering from $LiNbO_3$ had not as yet been observed. Therefore, the study of the tunable idler power generated in spontaneous scattering from the 628 cm^{-1} optical mode in $LiNbO_3$ was selected as an initial goal. This was a continuation of the work of Puthoff, et al.,[17] who had examined the signal power generated in this scattering process. The detection of the idler would have been significant for two reasons. First, it would have provided a simple tunable source in the 16-20 μ wavelength region. Second, its detection would have verified for the first time, the theoretical prediction of its existence.[15,18-21] For the purpose of the experiment, an argon laser was constructed for use as a pump, and a phase-sensitive detection system, incorporating a Ge:Cu infrared detector, was assembled. The laser and detection system form a test set for spontaneous scattering measurement which is useful for a broad range of such measurements, with only minor modifications.

During the course of this work, however, the first observation of stimulated scattering from $LiNbO_3$ was reported[22] and was quickly followed by the detection of tunable stimulated outputs (using an external resonator) from the same material.[23] The effort on this

program was therefore shifted to an investigation of the stimulated Raman effect. In the course of these experiments, tunable, stimulated, optical scattering from the 248 cm^{-1} mode, which did <u>not</u> require an external resonator, was observed. In addition, the idler radiation accompanying this process was detected.[24]

Finally, measurements of the spontaneous scattering from the 248 cm^{-1} mode were performed.

Theoretical calculations were carried out in conjunction with the experimental effort. The results of these calculations were in good agreement with the experimental results for both the stimulated and spontaneous cases.

In summary, the highlights of this work are:

(1) The elaboration and extension of the theory of stimulated and spontaneous scattering and its application to the A_1-symmetry modes of $LiNbO_3$.

(2) The observation of tunable, stimulated optical and infra-red outputs in scattering from the 248 cm^{-1} mode of $LiNbO_3$, without the use of an external resonator.

(3) The measurement of spontaneous scattering from the 248 cm^{-1} mode, whose frequency tuning accurately confirmed the calculated dispersion characteristic, and whose magnitude variation with frequency agreed closely with that predicted by the developed theory.

(4) The construction of a spontaneous scattering test set, consisting of an argon laser and a phase-sensitive detection system.

Chapter II of this report contains a discussion of vibrational modes in crystals and the derivation of the polariton dispersion curve for infrared active media. A brief discussion of phase matching on the polariton modes is followed by a presentation of a simple, physical picture of the Raman process. Finally, a qualitative comparison of spontaneous and stimulated scattering is presented.

Chapter III contains the theoretical analysis and calculations. First, a classical analysis of the stimulated process is given. Using an energy density approach,[24,25] it closely follows the method of Henry and Garrett,[21] extending their results to a material with more than one vibrational mode and removing the "high-loss" restriction made in their paper. Then, a quantum mechanical calculation, using rate equations, is performed, yielding the spontaneous scattering cross sections. These results are then related to the stimulated gain coefficient. This gives the expressions needed for the calculations of the nonlinear constants of a material.

In Chapter IV, the results of the previous chapter are applied to $LiNbO_3$. After the calculation of the nonlinear constants for the A_1-symmetry modes, the stimulated gain and idler power are determined for the two major modes (248 cm^{-1} and 628 cm^{-1}). The spontaneous scattering parameters (for both signal and idler) for these two modes are also calculated.

In Chapter V, three sets of experiments are reported. First, the argon laser and phase-sensitive detection system are described, along with the study of the idler power generated in spontaneous scattering from the 628 cm^{-1} mode in $LiNbO_3$. Then, the observation of tunable, stimulated optical and infrared emission in scattering from the 248 cm^{-1} mode is discussed and compared to theory. Finally, spontaneous scattering measurements, which agreed with the results of the developed theory, are described.

Chapter VI summarizes the highlights of this work. The calculations performed in this work are done in esu units. The choice of this system was made because the two major references for this work use esu units. The comparison between the theory developed in this work and that of these two references would have been more difficult if a different system had been used. For those interested in converting the results to MKS units, the author recommends the use of Table 4 in the Appendix of Jackson.[27]

Extensive use is made of the designation of frequency, energy and propagation constant in terms of wave numbers (cm^{-1}). Conversion of these quantities in cm^{-1} to other units may be accomplished with the aid of the Nomograph of Electromagnetic Conversions of Pantell and Puthoff[42] (p. 361).

The labeling of the frequencies of the three waves is done with the subscripts p, s, and i for the pump, signal, and idler, respectively.

CHAPTER II

TECHNICAL BACKGROUND

A. VIBRATIONAL MODES IN CRYSTALS

Since this work is concerned with light scattering from crystals, we begin with a brief discussion of the vibrational modes in crystals. The main result of this section will be the calculation of the dispersion curve for crystals with infrared-active modes.

The solution for the propagation of a transverse vibrational wave through a diatomic lattice yields a dispersion characteristic with two branches.[28] This is shown schematically in Fig. 2.1. The lower branch, which intercepts the origin, is called the acoustic branch, since the frequencies associated with it are approximately those of sound waves. The upper branch is called the optical branch for the analogous reason. If the results for the diatomic lattice are generalized to a material with p atoms in a primitive cell, the dispersion curve for transverse vibrations in one direction is composed of one acoustic branch and (p-1) optical branchnes.

It can also be shown[28] that, on the optical branch, alternate planes of atoms vibrate against each other, while the center of mass of the primitive cell remains fixed. If the atoms in alternate planes carry opposite charges, then vibrations of this type are capable of absorbing and radiating electromagnetic energy at the vibration frequency.

The presence of infrared activity alters the dispersion curve of the material in the region of the vibration frequency due to coupling to the electromagnetic wave. This will now be derived since this calculation introduces some of the concepts and quantities which will be used extensively later.

- 8 -
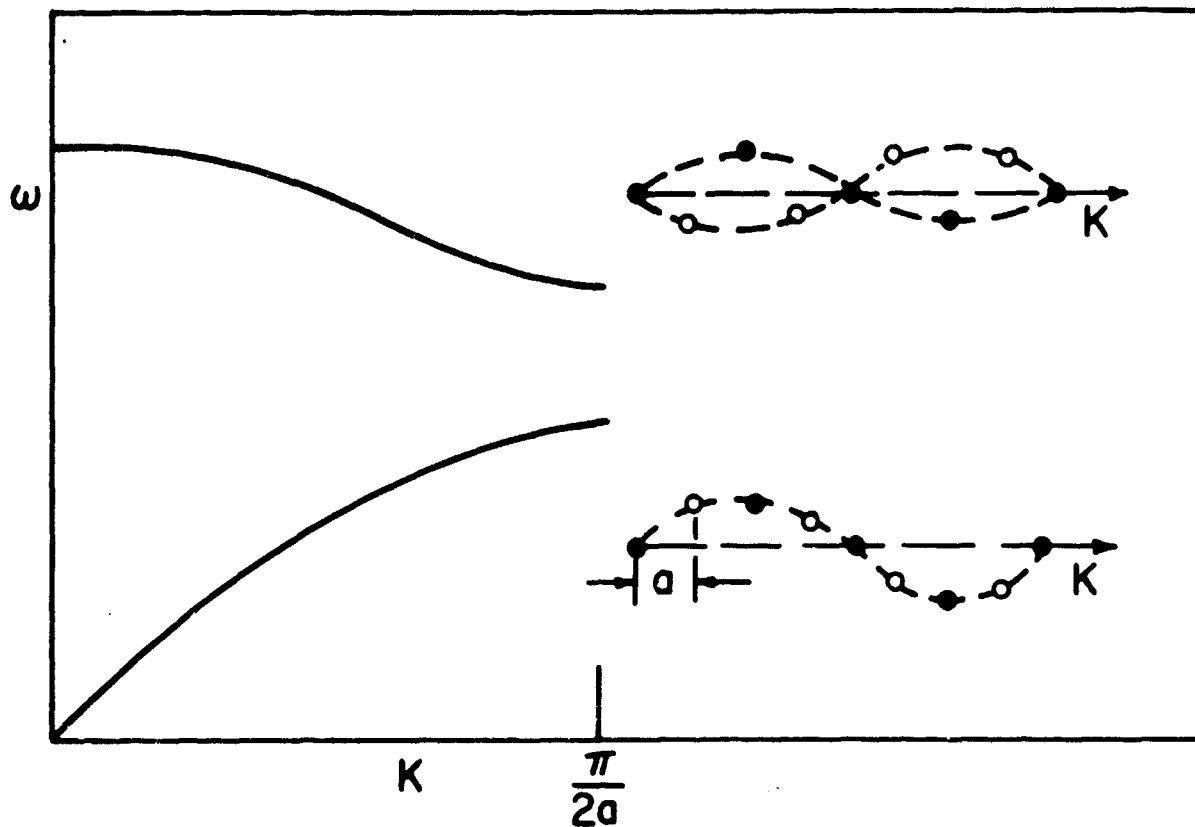
FIG. 2.1--Dispersion curve for transverse vibrations of a diatomic lattice. The lower curve is the acoustic branch; the upper one is the optical branch. A sketch of the motion of the atoms during vibration is shown next to each branch.

- 9 -

We start with the coupled-wave equation:

$$\nabla \times [\nabla \times E(\omega)] + \frac{1}{c^2} \epsilon_\infty \frac{\partial^2 E(\omega)}{\partial t^2} = -\frac{4\pi}{c^2} \frac{\partial^2 P(\omega)}{\partial t^2} \quad , \quad (2.1)$$

where $E(\omega)$ and $P(\omega)$ are the electric field and polarization oscillating at frequency ω , c is the velocity of light and ϵ_∞ is the dielectric constant on the high frequency side of the vibration. For simplicity, the problem for a material with a single mode is solved and the results are then extended to the multimode case.

The polarization results from mechanical vibration, which, in turn, is related to the electric field through the equation for the driven harmonic oscillator; thus,

$$P(\omega) = NeQ(\omega) \quad , \quad (2.2)$$

where e is the charge assoicated with the transverse vibration; N is the number of primitive cells per unit volume; Q is the non-equilibrium separation of the vibrating particles within the primitive cell, and

$$\mu[\ddot{Q}(\omega) + \Gamma\dot{Q}(\omega) + \omega_0^2 Q(\omega)] = eE(\omega) \quad , \quad (2.3)$$

where μ is the reduced mass of the vibrating particles; ω_0 is the resonant frequency of the vibration; and $\mu\Gamma$ is the damping coefficient.

Now, with the assumption that $E(\omega)$, $P(\omega)$ and $Q(\omega)$ vary as $e^{i(\vec{k}\cdot\vec{r}-\omega t)}$, Eqs. (2.1) and (2.3) become respectively,

$$\left(-k^2 + \frac{\omega^2}{c^2}\epsilon_\infty\right)E(\omega) = -\frac{4\pi\omega^2}{c^2}P(\omega) \quad (2.4)$$

and

$$\mu D(\omega)Q(\omega) = eE(\omega) \quad , \quad (2.5)$$

where

$$D(\omega) \equiv \omega_0^2 - \omega^2 - i\Gamma\omega \quad . \quad (2.6)$$

- 10 -

Solving for $Q(\omega)$ and substituting into Eq. (2.2), we obtain

$$P(\omega) = \frac{Ne^2}{\mu D(\omega)} E(\omega) \quad . \tag{2.7}$$

Substitution of Eq. (2.7) into Eq. (2.4) gives the result:

$$k^2 = \frac{\omega^2}{c^2} \left(\epsilon_\infty + \frac{4\pi Ne^2}{\mu D(\omega)} \right) \quad .$$

And finally the definition of

$$\Omega_p^2 = \frac{4\pi Ne^2}{\mu}$$

puts the result in the form:

$$k^2 = \frac{\omega^2}{c^2} \left(\epsilon_\infty + \frac{\Omega_p^2}{D(\omega)} \right) = \frac{\omega^2}{c^2} \epsilon(\omega) \quad . \tag{2.8}$$

This is sketched in Fig. 2.2 with the real part and imaginary part of k plotted versus ω, where $k = k' + ik''$. The real part of k, k', determines the propagation constant, while the imaginary part, k'', specifies the absorption.

A second, perhaps more physical way of visualizing the coupling effect is shown in Fig. 2.3 for the lossless case. Dashed lines represent the separate propagation curves for the electromagnetic and vibrational waves. The slope of the electromagnetic wave dispersion curve is constant and inversely proportional to the index of refraction. For simplicity, the lattice optical branch is drawn as a straight line. "Far" from the resonant frequency ω_0 (below point A) the dispersion curve follows that of the pure electromagnetic wave and the curve is photon-like. In this region, the magnitude of the vibrational displacement is negligible and most of the energy of the coupled system is electromagnetic. As the resonant frequency is
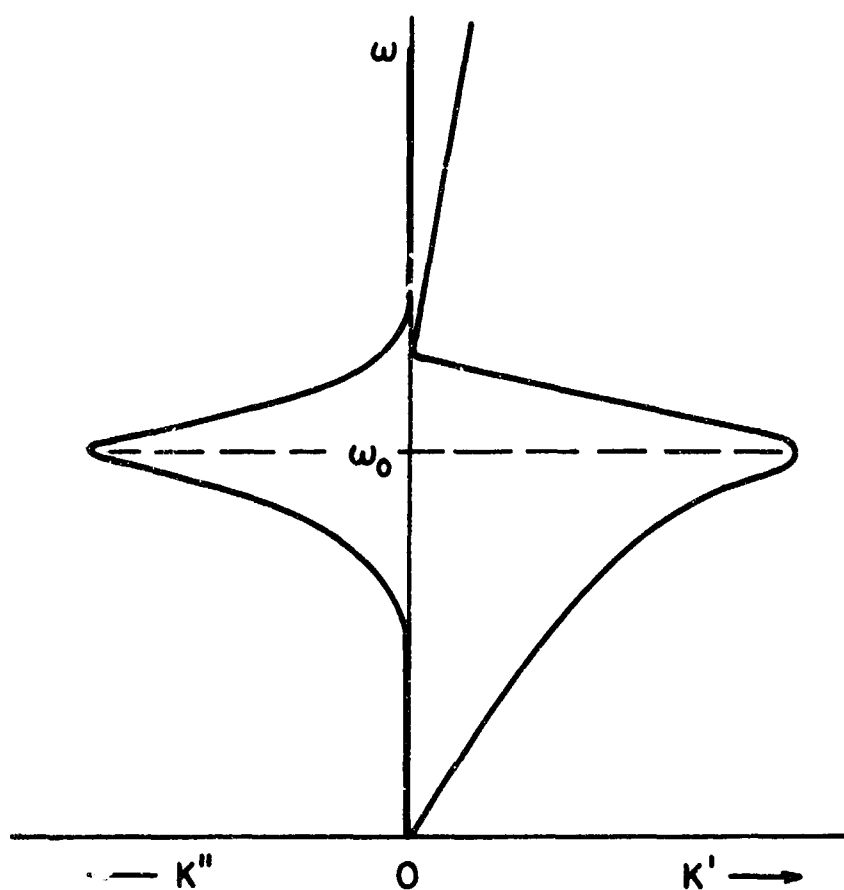
FIG. 2.2--Frequency plotted against the propagation constant, k′, and the electric field absorption constant, k″, for an infrared active material with a single mode. The right hand figure is the dispersion curve.
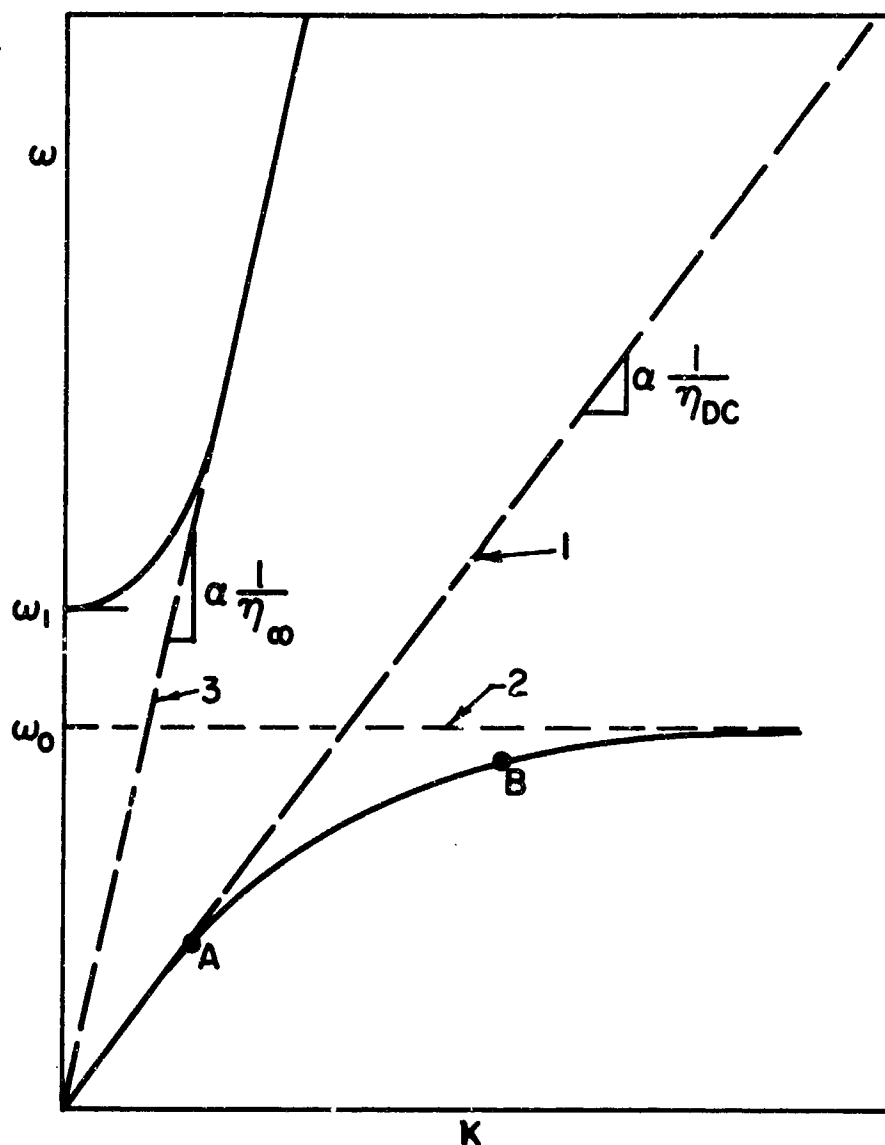
FIG. 2.3--The dispersion curve can be visualized as being formed by the coupling of electromagnetic dispersion characteristics with the optical branch of a lattice mode. Curve 1 and Curve 3 are the electromagnetic characteristics, with slopes determined by the dc and high frequency refractive indices, respectively. Curve 2 is an optical branch of the lattice dispersion curve, drawn as a straight line for convenience. The details of the coupling are described in the text.

approached, (between points A and B), coupling between the electro-magnetic and vibrational wave increases and the curve bends sharply. In this region, the energy of the system is divided nearly equally between mechanical and electromagnetic energy. We will call this the coupled region of the curve. Beyond point B , the curve is phonon-like and most of the energy is mechanical. In the lossless case, $k \to \infty$ as $\omega \to \omega_0$.

In the frequency limit $\omega \gg \omega_0$, the electromechanical coupling is negligible and the dispersion curve is that of the electromagnetic wave. As ω is reduced from this limit, the coupling increases and the curve flattens out again, becoming phonon-like. The solution for $k = 0$ is easily obtained by setting $\epsilon(\omega) = 0$ in Eq. (2.8) and it is found that

$$\omega_1 = \sqrt{\frac{\epsilon_{DC}}{\epsilon_\infty}}\, \omega_0 \qquad ,$$

where

$$\epsilon_{DC} = \epsilon_\infty + \frac{\Omega_p^2}{\omega_0^2} \qquad . \tag{2.9}$$

It can be shown[29] by considering longitudinal wave solutions to Eq. (2.1) that the longitudinal mode frequency is also determined by $k = 0$ and therefore

$$\omega_{LO} = \omega_1 = \sqrt{\frac{\epsilon_{DC}}{\epsilon_\infty}}\, \omega_0 \qquad . \tag{2.10}$$

This is the familiar Lydanne-Sachs-Teller relationship for the lossless case. The equivalent relationship for a lossy material has been derived by Barker.[30]

The extension to a material with more than one vibration frequency is straightforward. In this case,

$$P(\omega) = \left[\sum_j \frac{N_j e_j^2}{\mu_j D_j(\omega)} \right] E(\omega) \qquad ,$$

and

$$k^2 = \frac{\omega^2}{c^2} \left(\epsilon_\infty + \sum_j \frac{\Omega_{p_j}^2}{D_j(\omega)} \right) = \frac{\omega^2}{c^2} \epsilon(\omega) \quad , \qquad (2.11)$$

where

$$\Omega_{p_j}^2 = \frac{4\pi N_j e_j^2}{\mu_j} \quad , \quad D_j(\omega) = \omega_{0_j}^2 - \omega^2 - i\Gamma_j \omega \quad .$$

Thus, the dispersion curve for such a material has a "bump" at each vibration frequency ω_{0_j}, the magnitude of the bump being proportional to Ω_{p_j} for that mode.[*]

The division of the dispersion curve into three regions as shown in Fig. 2.3, will take on additional significance in Chapter III, where the scattering theory is developed. There, the photon-like, coupled, and phonon-like portions are relabeled as the parametric, vibrational and Raman regions. This is done to point out the regions in which different terms in the nonlinear polarizations play a predominant role.

B. THE SCATTERING PROBLEM—GENERAL CONSIDERATIONS

The two conditions which must be satisfied in a scattering process are conservation of energy and momentum. We consider specifically the three-wave process described in Chapter I, where a pump wave is scattered from an optical mode in a crystal, generating signal and

---

[*]Barker[30] and Barker and Loudon[31] use a slightly $\alpha_\perp$ ⊥t notation. They define $S_j \omega_{0_j}^2 \equiv \Omega_{p_j}^2$, where S_j is called the oscillator strength for the mode. This form yields the result

$$\epsilon_{DC} = \epsilon_\infty + \sum_j S_j \quad . \qquad (2.12)$$

idler waves. The appropriate equations for the interaction are

$$\omega_p = \omega_s + \omega_i \qquad (2.13a)$$

$$\vec{k}_p' = \vec{k}_s' + \vec{k}_i' \quad , \qquad (2.13b)$$

where

$$k' = \frac{\omega \eta}{c} \qquad .$$

The vector diagram for Eq. (2.13b) is shown in Fig. 2.4, where θ is the angle between $\vec{k}_p$ and $\vec{k}_s$ and varies from 0° for the col-linear forward scattering to 180° for collinear backward scattering. This work is mainly concerned with scattering for $\theta \lesssim 10^o$ which is generally referred to as near-forward scattering.

Solution of Eq. (2.13b) together with Eq. (2.13a) yields a family of k_i' vs ν_i curves for different values of θ. These curves are obtained from Eq. (2.14), with the substitution $\nu_i = \nu_p - \nu_s$. The intersections of these curves with the dispersion curve indicate the frequency and wave vector of the idler which will take part in the scattering process for each angle. This is shown schematically in Fig. 2.5.

C. THE RAMAN EFFECT - A SIMPLE PHYSICAL PICTURE[33]

In this section, a simple physical picture of the interaction of light with a vibrational mode is given.

The pump is at frequency ω_p which is assumed to be far above the highest vibrational resonance of the molecular ions (i.e., $\omega_p \gg \omega_{0_j}$). To zero order, therefore, the ions do not respond to the applied field and only the electrons contribute to the polariza-bility. Neglecting the dispersive effect of the "tails" of the elec-tronic resonances, the polarizability, α , will be independent of frequency. The polarization, given by

$$P = \alpha E = \alpha \bar{E}_p \cos \omega_p t \quad , \qquad (2.15)$$
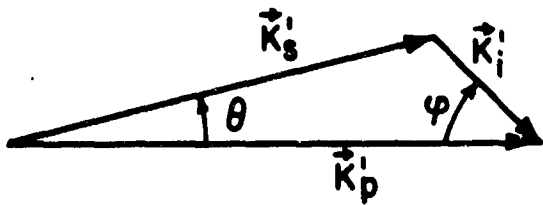
$$\vec{K}'_i = \vec{K}'_p - \vec{K}'_s$$

$$K'^2_i = K'^2_p + K'^2_s - 2K'_p K'_s \cos\theta$$

$$= 4\pi^2(\nu_p\eta_p - \nu_s\eta_s)^2 + 8\pi^2\nu_p\nu_s\eta_p\eta_s(1-\cos\theta) \quad (2.14)$$

WHERE ν IS THE FREQUENCY IN cm^{-1}
AND η IS THE REFRACTIVE INDEX

FIG. 2.4--Momentum conservation triangle. The angle θ is the phase-matching angle. The solutions of (2.13b), together with the energy conservation condition $(\nu_i = \nu_p - \nu_s)$, are a family of curves of k_i vs ν_i. These curves are referred to as phase-matching lines.
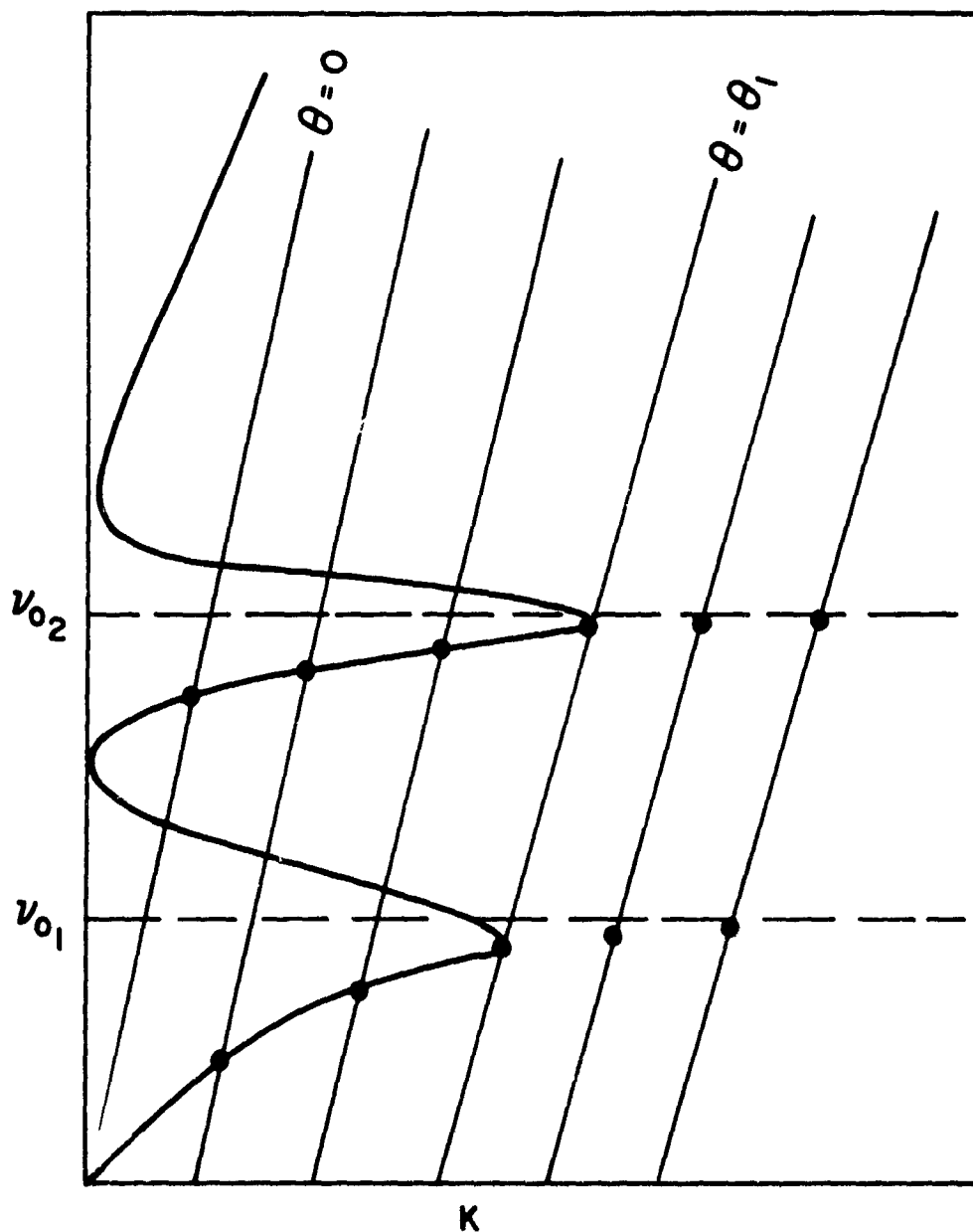
FIG. 2.5--Schematic representation of the phase-matching lines,
superimposed on the dispersion curve for a two-mode
material. The points of intersection indicate the
idler frequencies participating in the scattering
process. For $\theta > \theta_1$, the phase-matching lines do
not intersect the dispersion curve, and the idler
is of phonon nature in this region. The idler frequency
asymptotically approaches the resonant vibration
frequency for large θ . This has been verified
experimentally.[17,32]

- 18 -

will therefore contain only a term at ω_p .

. There is some energy transfer, however, between the electron cloud and the ions, causing small ionic vibrations. In this case, the electronic polarizability is a function of the coord'nates of the ions. If the polarizability is written as an expansion in the normal modes of vibration about the equilibrium position, we get

$$\alpha = \alpha_0 + \sum_j \frac{\partial \alpha}{\partial Q_j} Q_j + \text{higher order terms} \quad , \qquad (2.16)$$

where

$$Q_j = \bar{Q}_j \cos \omega_{i_j} t \quad .$$

Now, substitution of Eq. (2.16) into Eq. (2.15) yields (to first order)

$$P = \alpha_0 E + \sum_j \frac{\partial \alpha}{\partial Q_j} Q_j E$$

$$= \alpha_0 \bar{E}_p \cos \omega_p t + \sum_j \frac{\partial \alpha}{\partial Q_j} \bar{Q}_j \bar{E}_p \cos (\omega_p - \omega_{i_j})t$$

$$+ \sum_j \frac{\partial \alpha}{\partial Q_j} \bar{Q}_j \bar{E}_p \cos (\omega_p + \omega_{i_j})t \qquad . \qquad (2.17)$$

Thus polarizations are generated at the sum and difference frequencies. Historically, the line at the difference frequency (ω_s) is called the "Stokes" output and the line at the sum frequency (ω_s') is called the "anti-Stokes" output. In spontaneous scattering and under most conditions in stimulated scattering, the Stokes output is stronger than the corresponding anti-Stokes output.

In this discussion, ω_i has been taken to be the resonant frequency of a normal mode of vibration. As described previously, in infrared-active media, the vibrations can be driven off resonance. Hence, ω_i

can be generalized to represent any frequency on the dispersion curve for the material. As long as the wave vector and frequency conservation conditions are satisfied, tunable outputs at ω_s and ω_i can be generated.

D. QUALITATIVE COMPARISON OF STIMULATED AND SPONTANEOUS SCATTERING

While both stimulated and spontaneous scattering arise from the same physical process (described briefly in the previous section), there are differences between them. Qualitatively, some of the important differences are as follows:

a. Stimulated scattering is a threshold process,[*] requiring power densities on the order of 10^8 W/cm^2 to initiate the process. Power densities of this magnitude are available only from Q-switched lasers. It is for this reason that stimulated scattering was not observed until after the development of the Q-switched laser.

b. Signals generated in stimulated scattering are of narrow spectral width and are well collimated. In contrast, spontaneous scattering outputs are scattered into all directions and possess the spectral width of the scattering vibrational mode.

c. The conversion efficiency (generated signal power divided by input pump power) of spontaneous scattering is about 10^{-6}, while the stimulated scattering conversion efficiency is typically 1-30% and theoretically can approach 100%.

These and other properties of the two processes are presented for comparison in Fig. 2.6. Many of these will be discussed quantitatively in later chapters.

---

[*]For the case we are considering, the terms stimulated and threshold are defined as follows: the signal emission is stimulated when the exponential growth term predominates over the linear growth term. The power density which produces this is the threshold power density.

- 20 -

STIMULATED SCATTERING	SPONTANEOUS SCATTERING
Spatial coherence of pump	Scattered into all directions
Narrow spectral linewidth	Spectral width of vibrational mode
Threshold process	Nonthreshold process
Conversion eff. of ~ 100% is theoretically possible	Conversion eff. is typically 10^{-6}
Exponential growth of signal	Linear growth of signal
Large quantum nos. classical-like process	Small quantum nos. requires quantum-mechanical analysis

FIG. 2.6--A qualitative comparison of some of the properties of stimulated and spontaneous scattering.

CHAPTER III

THEORETICAL ANALYSIS

A. INTRODUCTION

This chapter is devoted to a theoretical analysis of stimulated and spontaneous scattering. First, a classical analysis of the stimulated scattering problem is carried out. Using the energy density approach,[25],[26] the analysis follows the method of Henry and Garrett.[21] The significant contribution of the present work is to extend their results to a multimode material and to derive a gain expression which is not restricted, as theirs is, to either the collinear case or the "high-loss" case.

A quantum mechanical calculation, using rate equations, follows. When applied to the stimulated process, the results of this analysis agree with the classically derived expressions as expected. In addition, the scattering parameters of the spontaneous process, which can not be arrived at classically, are derived. Finally, the procedures for computing the material nonlinear coefficients are determined.

B. STIMULATED SCATTERING - CLASSICAL ANALYSIS

A classical analysis of stimulated scattering is presented in this section. This problem has been discussed previously by Loudon,[15] Butcher, Loudon, and McLean,[18] Shen,[19] Henry and Garrett[21] and in an unpublished work by Puthoff.[34] The calculations presented in this section are based upon the work of the latter two references. In particular, the approach of Henry and Garrett, hereafter called HG , will be followed.

We begin by assuming plane waves for the pump, signal and idler electromagnetic fields (E) and for the lattice displacement field (Q).

Thus

$$E_\beta = E(\omega_\beta) + c.c. = A_\beta \, e^{i(\vec{k}_\beta \cdot \vec{r} - \omega_\beta t) + \vec{\gamma}_\beta \cdot \vec{r}} + c.c. \quad ,$$

$$(3.1)$$

where $\beta = p$, s, i for the pump, signal and idler fields respectively, $\vec{\gamma}$ is the growth (or decay) constant, and c.c. denotes complex conjugate; and

$$Q_i = Q(\omega_i) + c.c. = Q_i \, e^{i(\vec{k}_i \, \vec{r} - \omega_i t) + \vec{\gamma}_i \cdot \vec{r}} + c.c. \quad .$$

$$(3.2)$$

Before proceeding, several comments concerning the definition of the plane-wave fields are in order. A possible source of confusion is the definition of the complex amplitudes without the usual factor of $\frac{1}{2}$. This convention, first introduced by Pershan,[35] is used here because HG use it. This leads to

$$Re \, (E_\beta) = 2 \, A_\beta \, \cos(\vec{k}_\beta \cdot \vec{r} - \omega_\beta t) \quad ,$$

or a real amplitude of $2A_\beta$. This has two consequences of which one has to be aware in order to avoid the annoying "factor of two" difficulties. First, the intensity of the plane wave defined in (3.1) is

$$I_\beta = \frac{c \eta_\beta \, |A_\beta|^2}{2\pi} \quad . \qquad (3.3)$$

(The more common expression has a factor of 8 in the denominator.)

Secondly, as discussed by Bloembergen,[36] this definition leads to a factor of 2 increase in the lowest order nonlinear susceptibilities and additional factors of 2 increase in higher order ones. Thus, in the body of this work, when results are compared to those in the literature, (and to Puthoff,[34] who uses the more widespread convention), the

- 23 -

appropriate factors must be introduced. This will be noted each time
it is done to minimize confusion for the reader.

To continue with the analysis, we note that the three basic
equations used to describe the problem have already been referred to
in Chapter II. They are the coupled wave equation (2.1), (written
for the three fields of interest), the polarization equation (2.2),
and the driven oscillator equation (2.3). The significant difference
between the analysis of that chapter and the analysis here is that
in Chapter II attention was confined to the solution of the linear problem,
by using only the linear polarization term in the coupled-wave equation
and the linear force term in the oscillator equation. In this
chapter, the nonlinear driving terms will be included.

The coupled wave equation is written in (2.1). In general, with
fields polarized in more than one direction, the tensor character of
the dielectric constant must be included. In this work, however, we
are concerned with the situation where all fields are polarized in the
same direction, (along the c-axis of the crystal). Therefore, the
tensor notation is not necessary. In addition, it should be pointed
out that the polarization in (2.1) includes **both** linear and nonlinear
terms where applicable.

A generalization of the driven oscillator equation (2.3) yields

$$\mu_j \, D_j \, (\omega_i) \, Q_j(\omega_i) \; = \; F_j(\omega_i) \; = \; e_j \, E(\omega_i) + F_j^{NL}(\omega_i) \quad ,$$

$$(3.4)$$

where the equation has been written for the jth vibrational mode of
a multimode material and the total force has been divided into two
parts; the linear part, (which is the same as before), and a nonlinear
term arising from the scattering process.

There are several approaches to the calculation of the nonlinear
driving terms for (2.1) and (3.4). One approach, developed by Puthoff,[34]
is to derive the equations of motion for the dipole moments and
polarizability from quantum mechanical considerations using the density
matrix approach. These equations are then solved to yield the

polarizations in terms of susceptibilities which are, in turn, defined in terms of the matrix elements of the electric dipole moments and polarizabilities.

A second method, which is used by HG and which will be used here, assumes the existence of a phenomenological energy density function, U, from which the nonlinear driving terms can be derived directly. This approach was first suggested by Kleinman.[25] A detailed discussion of the energy density approach is presented in Appendix A.

In the problem under consideration, there are electromagnetic fields present at ω_p, ω_s and ω_i, and a lattice displacement at ω_i, with contributions to the lattice displacement from j modes. The appropriate form of the energy density fuction is shown in Appendix A to be

$$U[Q(\omega_i), E(\omega_i), E(\omega_s), E(\omega_p)]$$

$$= - [d_E \, E(\omega_p) \, E(\omega_s)^* \, E(\omega_i)^* + E(\omega_p) \, E(\omega_s)^* \, \sum_j N_j \, d_{Q_j} \, Q_j(\omega_i)^*] + c.c.$$

$$(3.5)$$

The quantities d_E and d_Q are the nonlinear coefficients for the material. It has been shown[37] that the taking of d_E and d_Q to be real and constant is consistent with experimental results. Also, it shall be demonstrated later that d_Q is related to the more familiar nonlinear susceptibility. The quantities d_E and d_Q are third rank tensors, but, as explained before, the tensor notation is not needed to describe the process of interest for this work.

As indicated in Appendix A, the nonlinear driving terms are derived from the energy density function as follows:

$$P^{NL}(\omega_\beta) = - \frac{\partial U}{\partial E(\omega_\beta)^*} \quad , \qquad (3.6a)$$

and

$$F_j^{NL}(\omega_i) = -\frac{1}{N_j} \frac{\partial U}{\partial Q_j(\omega_i)^*} \quad . \qquad (3.6b)^*$$

Taking the appropriate derivatives and substituting into (2.1) and (3.4), we obtain

$$\left(\nabla^2 + \frac{\omega_i^2}{c^2} \epsilon_{\infty_i}\right) E(\omega_i) = -\frac{4\pi\omega_i^2}{c^2}\left[d_E\, E(\omega_p)\, E(\omega_s)^* + \sum_j N_j\, e_j\, Q_j\,(\omega_i)\right]$$

$$(3.7a)$$

$$\left(\nabla^2 + \frac{\omega_s^2}{c^2} \epsilon_{\infty_s}\right) E(\omega_s) = -\frac{4\pi\omega_s^2}{c^2}\left[d_E\, E(\omega_p)\, E(\omega_i)^* + E(\omega_p)\sum_j N_j\, d_{Q_j}\, Q_j(\omega_i)^*\right]$$

$$(3.7b)$$

$$\left(\nabla^2 + \frac{\omega_p^2}{c^2} \epsilon_{\infty_p}\right) E(\omega_p) = -\frac{4\pi\omega_p^2}{c^2}\left[d_E\, E(\omega_s)\, E(\omega_i) + E(\omega_s)\sum_j N_j\, d_{Q_j}\, Q_j(\omega_i)\right]$$

$$(3.7c)$$

$$\mu_j\, D_j(\omega_i)\, Q_j(\omega_i) = e_j\, E(\omega_i) + d_{Q_j}\, E(\omega_p)E(\omega_s)^* \quad . \quad (3.7d)$$

The solution of (3.7 a-d), subject to the appropriate boundary conditions, yields a complete description of the process.

---

*Note that (3) of HG is incorrect. A simple dimensional analysis will show that the equation above is the correct one. It is appropriate to point out at this time that the middle equation of (2) of HG is also a misprint since the right-hand side should contain the total polarization (nonlinear and linear terms). Both of these misprints have been eliminated in (7) of their paper and hence their results are correct.

- 26 -

In practice, however, it is impossible to obtain a complete
solution in closed form without making some assumptions. The first
assumption is to neglect pump depletion. This is equivalent to the
statement that the polarization terms on the RHS of (3.7c) are small
and do not significantly alter the intensity of the pump field from
its initial value at the input of the crystal. Therefore, (3.7c)
is dropped, A_p is treated as a constant and $\vec{\gamma}_p = 0$. Depletion
of the pump does occur under certain conditions in the experiments
to be described later and therefore this assumption is not completely
valid in that case.

To gain more physical insight into the problem, we solve for $Q_j(\omega_i)$
in (3.7d) and substitute this result into (3.7 a,b). This yields

$$Q_j'\,(\omega_i)^* = \frac{\Omega_{p_j}^2\; E(\omega_i)^*}{D_j(\omega_i)^*} + \frac{\Omega_{p_j}^2\; d_{Q_j}'\; E(\omega_p)^*\, E(\omega_s)}{D_j\,(\omega_i)^*} \qquad (3.8a)$$

$$\left[\nabla^2 + \frac{\omega_i^2}{c^2}\epsilon_i^*\right] E(\omega_i)^* = -\frac{\omega_i^2}{c^2}\left[d_E'\; E(\omega_p)^*\, E(\omega_s) + E(\omega_p)^*\, E(\omega_s)\sum_j \frac{\Omega_{p_j}^2\; d_{Q_j}'}{D_j(\omega_i)^*}\right]^*$$

$$(3.8b)$$

$$\left[\nabla^2 + \frac{\omega_s^2}{c^2}\epsilon_{\infty_s}\right] E(\omega_s) = -\frac{\omega_s^2}{c^2}\left[d_E'\; E(\omega_p)\, E(\omega_i)^* + \left(\sum_j \frac{\Omega_{p_j}^2\; d_{Q_j}'}{D_j(\omega_i)^*}\right)E(\omega_p)\, E(\omega_i)^*\right.$$

$$\left.+\; |E(\omega_p)|^2\; E(\omega_s)\sum_j \frac{\Omega_{p_j}^2\; d_{Q_j}'^2}{D_j(\omega_i)^*}\right] \qquad .$$

$$(3.8c)$$

- 27 -

To get these equations, we have:

a) introduced the simplifying notation of HG:

$$d'_{Q_j} = \frac{d_{Q_j}}{e_j} \quad , \quad d'_E = 4\pi d_E$$

$$Q'_j = 4\pi N_j e_j Q_j \quad :$$

b) written

$$\epsilon_i = \epsilon_{\infty_i} + \sum_j \frac{\Omega^2_{p_j}}{D_j(\omega_i)} \quad :$$

and

c) taken the complex conjugates of (3.7a) and (3.7d) .

It is instructive to consider the three driving terms on the RHS of (3.8c). The first term, $d'_E \, E(\omega_p) \, E(\omega_i)^*$, is a typical polarization associated with parametric processes. It depends only on the product of two electromagnetic fields and exists independently of any vibrations. It will be largest in the region where $E(\omega_i)$ is largest. As was pointed out earlier, this will be in the photon-like portion of the dispersion curve where most of the energy of the mixed-system is electromagnetic. For this reason, the photon-like portion of the dispersion curve, (between the origin and point A of Fig. 2.3), is also called the parametric region.

The last term,

$$|E(\omega_p)|^2 \, E(\omega_s) \sum_j \frac{\Omega^2_{p_j} \, d'^2_{Q_j}}{D_j(\omega_i)^*} \quad ,$$

is the normal Raman polarization term. It originates from the product of the pump field and the lattice vibration displacement

and in no way depends upon the existence of $E(\omega_i)$, (i.e., it can exist in materials which are not infrared active). This term will predominate where $Q(\omega_i)$ is large, which is in the phonon-like portion of the dispersion curve. In addition, the resonant denominator maximizes this term at $\omega_i = \omega_{0_j}$; therefore, the "pure" Raman gain is largest at $\omega_s = \omega_p - \omega_{0_j}$ and this is the frequency at which "pure" Raman scattering is always observed. Hence the phonon-like portion of the curve, (between point B and the vibration frequency), is called the Raman region.

The middle term,

$$\left(\sum_j \frac{\Omega_{p_j}^2 \, d'_{Q_j}}{D_j(\omega_i)^*} \right) \; E(\omega_p) \; E(\omega_i)^* \quad ,$$

depends upon the existence of both a lattice vibration and an electric field at ω_i . The influence of this term is felt most strongly in the middle (or coupled) region of the dispersion curve due to the counterbalancing effects of $E(\omega_i)$ and $D_j(\omega_i)$. This term has been called the vibrational term and the corresponding region of the dispersion curve (between points A and B) has been labeled the vibrational region.

At this point we compare the coupled-wave equations for ω_i and ω_s [(3.8b) and (3.8c)] to those given by Puthoff.[38] A term-by-term comparison, taking into account the comments after (3.2), reveals the following equivalences:

Present Work		Puthoff	
$\dfrac{\Omega_{p_j}^2}{D_j(\omega_i)}$		$4\pi \; \chi_{v_j}$	(3.9a)
$\dfrac{d'^2_{Q_j} \Omega_{p_j}^2}{D_j(\omega_i)^*}$		$16\pi \; \chi_{R_j}$	(3.9b)
$d'_E + \dfrac{\Omega_{p_j}^2 \, d'_{Q_j}}{D_j(\omega_i)^*}$		$8\pi \; \chi_{p_j}$,	(3.9c)

- 29 -

where χ_V , χ_R and χ_p have been identified by Puthoff as the vibrational, Raman and parametric susceptibilities respectively. (Note that these definitions do _not_ correspond to our usage of the same terms). Referring to (4.5) and (4.6) of Puthoff,[34] we find that the vibrational and Raman susceptibilities can be written as:

$$\chi_{V_j}(\omega_i) = \frac{\Gamma_j \, \omega_{0_j} \, \chi''_{V_j}(\omega_{0_j})}{D_j(\omega_i)}$$

$$\chi_{R_j}(\omega_i) = \frac{\Gamma_j \, \omega_{0_j} \, \chi''_{R_j}(\omega_{0_j})}{D_j(\omega_i)^*} \quad ,$$

where $\chi''_j(\omega_{0_j})$ is the value of the imaginary part of the susceptibility evaluated on resonance $(\omega_i = \omega_{0_j})$. Using these expressions and (3.9a,b), we establish the following relationships:

$$\Omega^2_{p_j} = 4\pi \, \Gamma_j \, \omega_{0_j} \, \chi''_{V_j}(\omega_{0_j}) \qquad (3.10a)$$

$$d^{'2}_{Q_j} \, \Omega^2_{p_j} = 16\pi\Gamma_j \, \omega_{0_j} \, \chi''_{R_j}(\omega_{0_j}) \qquad . \qquad (3.10b)$$

The latter, in particular, will be useful in later calculations.

Returning to the solution, the plane-wave expressions for $E(\omega_i)$, $E(\omega_s)$ and $Q(\omega_i)$ [(3.1, 3.2)] are substituted into (3.7). Exponential balance of both sides of the equations requires:

$$\vec{k}_p = \vec{k}_s + \vec{k}_i \qquad (3.11a)$$

$$\vec{\gamma}_i = \vec{\gamma}_s = \vec{\gamma} \qquad . \qquad (3.11b)$$

The simple result of (3.11b) is due to the assumption of no pump depletion $(\vec{\gamma}_p = 0)$. Cancellation of the equal exponentials

reduces (3.7) to:

$$\left[-(\vec{k}_i + i\vec{\gamma})^2 + \frac{\omega_i^2}{c^2}\epsilon_i^* \right] A_i^* + \frac{\omega_i^2}{c^2}\left(d_E' + \sum_j \frac{\Omega_{p_j}^2 d_{Q_j}'}{D_j(\omega_i)^*} \right) A_p^* A_s = 0$$

$$\frac{\omega_s^2}{c^2}\left(d_E' + \sum_j \frac{\Omega_{p_j}^2 d_{Q_j}'}{D_j(\omega_i)^*} \right) A_p A_i^*$$

$$+ \left[\frac{\omega_s^2}{c^2}|A_p|^2\left(\sum_j \frac{\Omega_{p_j}^2 d_{Q_j}'}{D_j(\omega_i)^*} \right) - (\vec{k}_s - i\vec{\gamma})^2 + \frac{\omega_s^2}{c^2}\epsilon_{s_\infty} \right] A_s = 0 \quad .$$

For a solution to exist,

$$\left[-(\vec{k}_i + i\vec{\gamma})^2 + \frac{\omega_i^2}{c^2}\epsilon_i^* \right]\left[\frac{\omega_s^2}{c^2}|A_p|^2\left(\sum_j \frac{\Omega_{p_j}^2 d_{Q_j}'}{D_j(\omega_i)^*} \right) - (\vec{k}_s - i\vec{\gamma})^2 + \frac{\omega_s^2}{c^2}\epsilon_{s_\infty} \right]$$

$$= \frac{\omega_i^2 \omega_s^2}{c^4}|A_p|^2\left(d_E' + \sum_j \frac{\Omega_{p_j}^2 d_{Q_j}'}{D_j(\omega_i)^*} \right)^2 \quad . \tag{3.12}$$

We now define the gain as the intensity change along the direction of propagation, which is very nearly the direction of the Poynting vector. Thus,

$$g_i = 2\hat{k}_i \cdot \vec{\gamma} \quad , \quad g_s = 2\hat{k}_s \cdot \vec{\gamma} \quad , \tag{3.13}$$

- 31 -

where $\hat{k}_i$ and $\hat{k}_s$ are unit vectors in the $\vec{k}_i$ and $\vec{k}_s$ directions, respectively.

Expanding $(\vec{k}_i + i\vec{\gamma})^2$ and $(\vec{k}_s - i\vec{\gamma})^2$ to first order in $\vec{\gamma}$, we obtain

$$(\vec{k}_i + i\vec{\gamma})^2 = k_i^2 + 2i\,\vec{k}_i \cdot \vec{\gamma} = k_i^2 + ik_i\,g_i$$

$$(\vec{k}_s - i\vec{\gamma})^2 = k_s^2 - i\,k_s\,g_s \quad .$$

Substitution of this into (3.12), yields the final equation:

$$
\left(-k_i^2 - i\,k_i\,g_i + \frac{\omega_i^2}{c^2}\,\epsilon_i^* \right)\left(\frac{\omega_s^2}{c^2}\,|A_p|^2 \sum_j \frac{\Omega_{p_j}^2\,d'_{Q_j}}{D_j(\omega_i)^*} - k_s^2 + i\,k_s\,g_s \right.
$$
$$
\left. + \frac{\omega_s^2}{c^2}\,\epsilon_{\infty_s} \right) = \frac{\omega_i^2\,\omega_s^2}{c^4}\,|A_p|^2 \left(d'_E + \sum_j \frac{\Omega_{p_j}^2\,d'_{Q_j}}{D_j(\omega_i)} \right)^2
$$

$$(3.14)$$

Now, assuming we know all of the material parameters, (i.e., d'_E , d'_{Q_j} , Ω_{p_j}) , the frequencies and wave vectors of the interacting signals and the intensity of the pump, there are still two unknowns-g_i and g_s -and only one equation. Thus an additional equation relating g_i and g_s is necessary. HG solve the problem by treating two limiting cases:

1) <u>High-loss region</u>: In this region, (3.14) is simplified by setting $g_i = 0$. This can be justified mathematically in regions of high loss at the idler, where $k_i\,g_i$ can be neglected compared to

$$\frac{\omega_i^2}{c^2}\,\text{Im}(\epsilon_i^*)$$

in (3.14). In this region, the calculation of g_s is done separately for two regions of ω_i for a <u>multimode</u> material:

a) For ω_i outside the linewidth of each of the j modes, an analysis is given in Appendix B, which shows that:

$$g_s = \frac{\omega_s \, |A_p|^2}{c \, \omega_i \eta_s} \left(\frac{1}{\sum_j \dfrac{\Gamma_j \, \Omega_{p_j}^2}{(\omega_{0_j}^2 - \omega_i^2)^2}} \right) \left(d_E' + \sum_j \frac{\Omega_{p_j}^2 \, d_{Q_j}'}{\omega_{0_j}^2 - \omega_i^2} \right)^2 \, ; \qquad (3.15a)$$

and

b) For ω_i within the linewidth of the mode with resonant frequency ω_{0_α}, the two summations in (3.14) are dominated by a single term; i.e.,

$$\sum_j \frac{\Omega_{p_j}^2 \, d_{Q_j}^2}{D_j(\omega_i)^*} \quad \longrightarrow \quad \frac{\Omega_{p_\alpha}^2 \, d_{Q_\alpha}^2}{D_\alpha(\omega_i)^*} \quad .$$

Thus, in this region, the calculation is identical to the single-mode treatment of HG and hence:

$$g_s = \frac{\omega_s \, \Omega_{p_\alpha}^2 \, |A_p|^2}{c \, \omega_i \, \eta_s \, \Gamma_\alpha} \left(\frac{\omega_{0_\alpha}^2 - \omega_i^2}{\Omega_{p_\alpha}^2} d_E' + d_{Q_\alpha}' \right)^2 \, . \qquad (3.15b)$$

- 33 -

If $\omega_i = \omega_{0_\alpha}$ is substituted into (3.15b), the result is:

$$g_s(\omega_{0_\alpha}) = \frac{\omega_s \, \Omega_{p_\alpha}^2 \, |A_p|^2 \, d_{Q_\alpha}^2}{c \, \omega_{C_\alpha} \, \eta_s \, \Gamma_\alpha} \quad . \qquad (3.15c)$$

Using the equivalences of (3.10b), this is seen t∙ agree with the standard expression for the on resonance Raman gain.[39]

Thus, (3.15a) and (3.15b) are the extensions of (18) of HG to a multimode material in the high-loss region. As we shall see later, this assumption is not valid throughout the entire range of the experimental observations.

2) <u>Collinear Interaction</u>: For the collinear process ($\theta = 0$), $g_i = g_s = g$. The result in this case (which is a straightforward generalization of the analysis in Appendix B of HG) is

$$\boxed{g = g_i = g_s = \frac{\alpha_i}{2}\left[\left(1 + \frac{16\alpha_p^2}{\alpha_i^2}\right)^{1/2} - 1\right]} \quad ,$$

$$(3.16)$$

where $\alpha_i = 2k_i'' =$ power absorption coefficient at ω_i ; and

$$\alpha_p^2 = \frac{\omega_i \, \omega_s}{4c^2 \, \eta_i \, \eta_s} \, |A_p|^2 \, \left\{d_E' + \sum_j \frac{\Omega_{p_j}^2 \, d_{Q_j}'}{\omega_{0_j}^2 - \omega_i^2}\right\}^2 \quad ,$$

$$(3.17)$$

where η_i and η_s are the refractive indices at ω_i and ω_s , respectively. Again, phase-matching has been assumed.

It is of interest to consider limiting cases of the collinear result:

a) Low-loss region

In this region, $\alpha_i \ll \alpha_p$ and

$$g_s = 2\alpha_p \quad . \qquad (3.18a)$$

b) High-loss region

In this region, $\alpha_i \gg \alpha_p$ and

$$g_s = \frac{4\alpha_p^2}{\alpha_i} \quad . \tag{3.18b}$$

This can be shown[40] to be equivalent to the previous high-loss expressions (3.15a) and (3.15b).

The collinear asumption is obviously not strictly valid except at the point of intersection of the $\theta = 0$ phase-matching line and the dispersion curve for the material. In addition, as we shall point out in more detail later, the collinear process is not possible for the lowest frequency mode of most materials (including LiNbO$_3$), since the intersection of the $\theta = 0$ phase matching line and the dispersion curve near the lowest mode occurs at $\omega_i = 0$.

Thus far, we have derived expressions for the stimulated gain in multimode media in both the high-loss approximation and in the collinear case. To the extent that these particular constraints apply, the expressions describe the stimulated scattering process. As has been pointed out, however, neither of these conditions is valid for the entire range of experiments to be described. The analysis which follows leads to a more general gain expression, which is valid over the entire region of near-forward scattering.

The approach in this analysis is to note that if the direction of $\vec{\gamma}$ can be determined, then the desired relationship between g_i and g_s can be obtained for all phase-matching angles. This is accomplished by considering the boundary conditions at the surface of the nonlinear material. The details of the calculation, first suggested by Bloembergen and Pershan,[41] are given in Appendix C. It is also shown in this appendix that the desired relationship between g_i and g_s for small-angle scattering and near-normal incidence of the pump is given as

$$g_i = g_s \cos \varphi \quad , \tag{3.19}$$

- 35 -

where φ is the angle between the idler and pump propagation directions (see Fig. 2.4).

As shown in Appendix D, this leads to the final result for small-angle scattering:

$$g_s = \frac{\alpha_i}{2 \cos \varphi} \left[\left(1 + \frac{16\alpha_p'^2}{\alpha_i^2} \right)^{1/2} - 1 \right]$$

$$\text{where} \quad \alpha_p'^2 = \cos \varphi \, \alpha_p^2$$

. (3.20)

Examining the same limits as before, we find:

Low Loss: $\qquad g_s = \dfrac{2\alpha_p'}{\cos \varphi} = \dfrac{2\alpha_p}{(\cos \varphi)^{1/2}}$ \qquad (3.21a)

High Loss: $\qquad g_s = \dfrac{4\alpha_p'^2}{\alpha_i \cos \varphi} = \dfrac{4\alpha_p^2}{\alpha_i}$. \qquad (3.21b)

Note that for collinear scattering ($\cos \varphi = 1$), these results agree with those of the previous analysis. Also of interest is the fact that the high loss result again agrees with the previous expressions (3.15) and (3.18b). The reason for this is that, in the high-loss region, the result for g_s is independent of the value used for g_i since the term involving g_i can be neglected in (3.14).

The results of this section are summarized graphically in Fig. 3.1 where g_s is sketched as a function of ω_i using the derived expressions. Similar curves, using the calculated numerical values for $LiNbO_3$, are presented in Chapter IV.
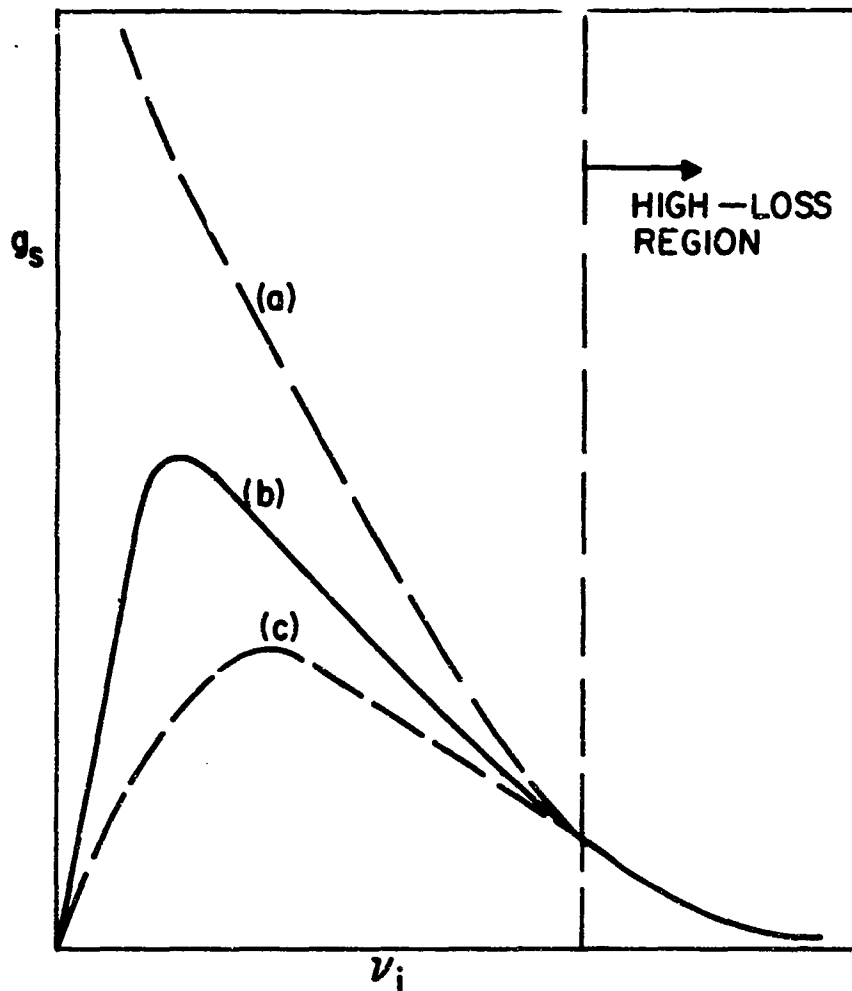
FIG. 3.1--Sketch of results of stimulated gain calculations, showing
signal gain coefficient (g_s) plotted against idler frequency.
Curve (b), drawn solid, is a plot of (3.20) and is valid over
the entire mode. Shown for comparison are Curves (a) and (c),
which are plots of (3.15) and (3.16), respectively. These are
not valid over the entire mode. Note that the three curves
coincide in the high-loss region; the reason for this is
explained in the text.

C. QUANTUM MECHANICAL ANALYSIS - STIMULATED AND SPONTANEOUS SCATTERING

The previous section contains a classical analysis, which is valid for the stimulated process since the quantum numbers are large. To include spontaneous effects, however, a quantum mechanical analysis is required. This is considered in this section.

We begin with the rate equations[42]

$$\frac{d\langle n_s \rangle}{dt} = K(\langle n_i \rangle + 1)(\langle n_p \rangle)(\langle n_s \rangle + 1) - K\langle n_i \rangle \langle n_s \rangle (\langle n_p \rangle + 1)$$

$$(3.22a)$$

$$\frac{d\langle n_s \rangle}{dt} = -\frac{d\langle n_p \rangle}{dt} = \frac{d\langle n_i \rangle}{dt} + \frac{\langle n_i \rangle}{\tau} \quad , \qquad (3.22b)$$

where $\langle n \rangle$ is the number of photons in a single mode, and the subscripts refer to the frequencies. Note that losses at the pump and signal have been neglected and loss at the idler has been accounted for by including the term $\langle n_i \rangle / \tau$. We have also defined

$$\frac{1}{\tau} \equiv v_i \, \alpha_i \quad ,$$

where v_i is the wave velocity at ω_i and α_i is the absorption coefficient at ω_i .

These equations are now applied to stimulated and spontaneous scattering.

1. Stimulated Scattering

In steady state,

$$\frac{d}{dt} \equiv \frac{\partial}{\partial t} + \vec{v} \cdot \nabla = v \cdot \nabla \quad .$$

Therefore, (3.22b) becomes

$$\vec{v}_s \cdot \nabla \langle n_s \rangle = \vec{v}_i \cdot \nabla \langle n_i \rangle + \alpha_i \langle n_i \rangle \quad . \tag{3.23}$$

Now assuming that $\langle n_i \rangle$, $\langle n_s \rangle$ grow as $e^{2\vec{\gamma} \cdot \vec{r}}$ as before, (3.23) becomes

$$2\vec{v}_s \cdot \vec{\gamma} \langle n_s \rangle = 2\vec{v}_i \cdot \vec{\gamma} \langle n_i \rangle + \alpha_i \langle n_i \rangle \quad .$$

But

$$2\vec{v}_s \cdot \vec{\gamma} = v_s \, g_s$$
$$2\vec{v}_i \cdot \vec{\gamma} = v_i \, g_i \quad .$$

Therefore, a relationship between $\langle n_i \rangle$ and $\langle n_s \rangle$ is derived;

$$\langle n_i \rangle = \frac{v_s}{v_i} \left(\frac{g_s}{g_i + \alpha} \right) \langle n_s \rangle \quad . \tag{3.24}$$

To calculate the idler power, we recall that[43]

$$\frac{\langle n \rangle}{V} = \frac{I\eta}{\hbar \omega c} \quad , \tag{3.25}$$

where I is the intensity and V is a volume whose linear dimension $L(V = L^3)$ is large compared to a wavelength, but small compared to the growth of the wave (i.e. $L \ll \frac{1}{g}$) .

Using (3.24) and (3.25) yields

$$\frac{P_i \, L_i}{P_s \, L_s} = \frac{\omega_i}{\omega_s} \left(\frac{g_s}{g_i + \alpha_i} \right) \quad ,$$

where P_i and P_s are the generated idler and signal power respectively, and where L_i and L_s are "small" distances along the direction of

propagation of ω_i and ω_s respectively. But

$$L_i = \frac{L_s}{\cos \varphi}$$

from geometric considerations; and therefore, after using (3.19) we get the result:

$$\boxed{\frac{P_i}{P_s} = \left(\frac{\omega_i}{\omega_s}\right) \left(\frac{g_s \cos \varphi}{g_s \cos \varphi + \alpha_i}\right)} \qquad . \qquad (3.26)$$

Examining the limiting case of (3.26), it is found that in the low-loss region $(\alpha_i \to 0)$

$$P_i = \frac{\omega_i}{\omega_s} P_s \qquad ,$$

the Manley-Rowe limit. In the high-loss limit,

$$\frac{P_i}{P_s} = \frac{\omega_i}{\omega_s} \frac{g_s \cos \varphi}{\alpha_i} \qquad .$$

We now calculate the signal gain in the high-loss limit. In this limit, the proper assumptions for the photon numbers are

$$\langle n_p \rangle , \langle n_s \rangle \gg 1$$
$$\gg \langle n_i \rangle \qquad .$$

Insertion of these assumptions into (3.22a) immediately yields

$$g_s = \frac{K\langle n_p \rangle}{c/\eta_s} \qquad . \qquad (3.27)$$

Note that in the high loss region g_s is proportional to pump intensity $(\alpha \langle n_p \rangle)$, in agreement with the classically derived result.

2. Spontaneous Scattering

The assumptions for the photon numbers $\langle n \rangle$ for the three waves in spontaneous scattering require a more detailed explanation. As in the stimulated case, $\langle n_p \rangle \gg 1$, having a value of $\sim 10^4$ for a 1 watt pump. Since spontaneous scattering efficiencies are typically $\sim 10^{-6}$, it may appear plausible to set $\langle n_s \rangle$, $\langle n_i \rangle \ll 1$. However, $\langle n \rangle$ is composed of two components; one due to scattering and the other arising from the Bose distribution (black body) which is given by

$$\bar{n} = \frac{1}{e^{\hbar\omega/kT} - 1} \quad , \tag{3.28}$$

where k is Boltzmann's constant and T is the temperature in $^\circ$K.

For room temperature, $\bar{n}_s \approx 0$, since ω_s is an optical frequency and $\hbar\omega_s \gg kT$. On the other hand, $\bar{n}_i$ may be equal to or greater than 1 depending upon the particular value of ω_i .

Therefore, the proper assumptions for spontaneous scattering are

$$\langle n_p \rangle \gg 1$$

$$\langle n_s \rangle = \langle \bar{n}_s + n_s(z_s) \rangle \ll 1$$

$$\langle n_i \rangle = \langle \bar{n}_i + n_i(z_i) \rangle \approx \bar{n}_i \quad .$$

Assuming the steady state and inserting the assumptions above, we find that (3.22a,b) become

$$v_s \frac{\partial \langle n_s \rangle}{\partial z_s} = K(\langle n_i \rangle + 1) \langle n_p \rangle = -v_p \frac{\partial \langle n_p \rangle}{\partial z_p} = v_i \frac{\partial \langle n_i \rangle}{\partial z_i} + \alpha_i v_i \langle n_i \rangle \quad .$$

$$\tag{3.29}$$

To arrive at an expression for the scattering cross-section, we solve (3.29) for n_p assuming $\langle n_i \rangle = \overline{n}_i$ = constant. This gives

$$\langle n_p(z_p) \rangle = \langle n_p(0) \rangle\, e^{-\frac{K(\overline{n}_i + 1)\eta_p z_p}{c}} \equiv \langle n_p(0) \rangle\, e^{-N\sigma^1 z_p} \quad .$$

(3.30)

The right hand equality is a statement of the standard definition of the scattering cross-section of a material with N scatters per unit volume.[44] The superscript 1 in σ^1 indicates that this is the cross section for a single mode, and integration over the total number of modes is required to obtain the total cross-section (σ). Since $N\sigma$ typically has a value of about 10^{-7} cm^{-1}, $\langle n_p(z_p) \rangle \approx \langle n_p(0) \rangle$ and $\langle n_p \rangle$ can be treated as a constant.

From (3.30), we get

$$\sigma^1 = \frac{K(\overline{n}_i + 1)}{N\, c/\eta p} \quad ,$$

and comparison of this to (3.27) yields

$$\boxed{\sigma^1 = \frac{g_s(\overline{n}_i + 1)\eta p}{N \langle n_p \rangle \eta_s}} \quad .$$

(3.31)

The solution for $n_s(z_s)$ is

$$\langle n_s(z_s) \rangle = \frac{K(\overline{n}_i + 1)\langle n_p \rangle}{c/\eta_s}\, z_s \quad .$$

(3.32)

Thus, the number of photons (in a single mode) at ω_s grows linearly with distance. Using representative values of the parameters in (3.32) leads to $\langle n_s \rangle \approx 10^{-6}$ for a 1 cm long crystal. This justifies the assumption $\langle n_s \rangle \ll 1$.

- 42 -

Finally, the solution for $n_i(z_i)$ is

$$\langle n_i(z_i) \rangle = \frac{K\langle n_p \rangle}{\alpha_i v_i - K\langle n_p \rangle} \left\{ 1 - e^{-\frac{\alpha_i v_i - K\langle n_p \rangle}{v_i} z_i} \right\} \ .$$

$$(3.33)$$

For spontaneous processes, $\alpha_i v_i \gg K\langle n_p \rangle$; this reduces (3.33) to

$$\langle n_i(z_i) \rangle = \frac{K\langle n_p \rangle}{\alpha_i v_i} \left(1 - e^{-\alpha_i z_i} \right) \ . \qquad (3.34)$$

Also, since typically $\alpha_i = 10^2 - 10^5 \ cm^{-1}$, (3.34) indicates that

$$\langle n_i(z_i) \rangle = \frac{K\langle n_p \rangle}{\alpha_i v_i} = \text{constant} \qquad (3.35)$$

for

$$z_i > \sim 10^{-2} \ cm \ .$$

Thus, the number of photons at ω_i builds up to the value given in (3.35) in a very short distance and remains constant at this level. Increasing the length of the crystal beyond several "absorption lengths" (where the "absorption length" $= 1/\alpha_i$) does not increase the number of idler photons. Physically, this result is due to the fact that at the value of $\langle n_i \rangle$ given by (3.35) the absorption and generation rates of idler photons are equal and hence there is no further change in the idler photon number.

Substituting representative values in (3.35), we get $\langle n_i(z_i) \rangle \approx 10^{-9}$, justifying the assumption $\langle n_i(z_i) \rangle \ll 1$.

The results of this section are plotted in Fig. 3.2.

- 43 -
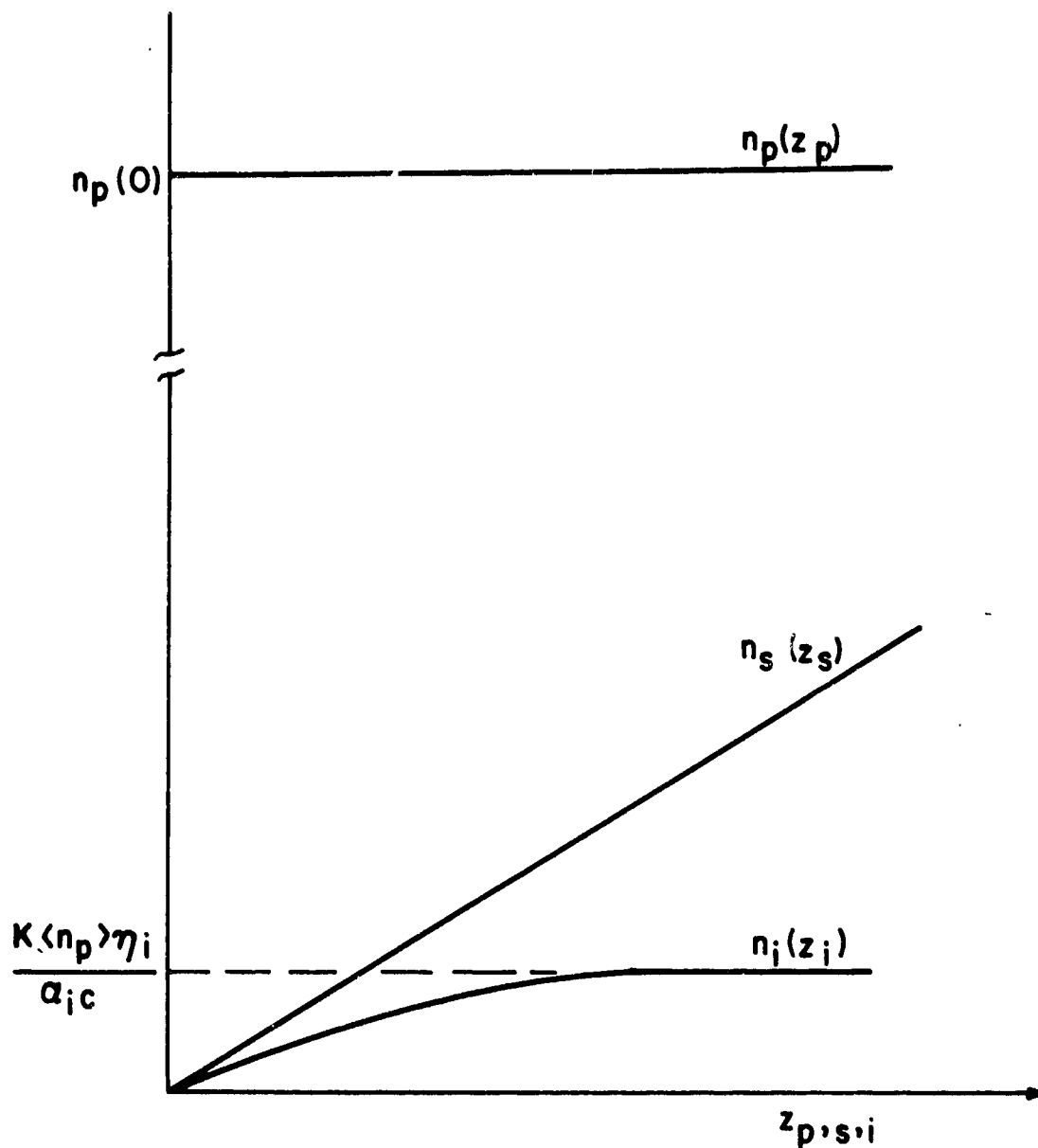
FIG. 3.2--The variation of photon numbers of pump, signal and idler, as a function of distance, for spontaneous scattering. The signal photon number grows linearly with distance, while the idler photon number reaches a constant value after a short interaction distance.

3. Applications

Using the results of the previous sections, expressions relating the stimulated gain coefficient and spontaneous scattering parameters will now be derived. These will be used in the calculation of the material nonlinear coefficients and in comparing the results of spontaneous scattering measurements to the developed theory.

a) Relationship of Scattering Cross-section to Stimulated Gain

The total cross-section per unit solid angle and per unit frequency range $(d\sigma/d\Omega d\omega)$ is obtained by writing

$$\frac{d\sigma}{d\Omega d\omega} = \sigma^1 \frac{dp(\omega)}{d\Omega d\omega} \quad , \qquad (3.36)$$

where

$$\frac{dp(\omega)}{d\Omega d\omega}$$

is the number of modes per unit solid angle per unit frequency range, and is given by[45]

$$\frac{dp(\omega)}{d\Omega \, d\omega} = \frac{V}{(2\pi)^3} \left(\frac{\omega_s^2 \, \eta_s^2}{c^3} \right) \quad . \qquad (3.37)$$

Using the result for σ^1 (3.31), we get after using (3.27),

$$\frac{d\sigma}{d\Omega \, d\omega} = \frac{k(\overline{n}_i + 1)V \, \omega_s^2 \, \eta_s^2}{N(c/\eta_p)(2\pi)^3 \, c^3} = \frac{g_s(\overline{n}_i + 1) \, \eta_p \eta_s^2 \, \omega_s^2 \, V}{Nc^3 <\eta_p>} \quad ,$$

and substituting (3.25) we obtain the result

$$\frac{d\sigma}{d\Omega\ d\omega} = \frac{g_s\ k_s^2\ \hbar\omega_p\ (\bar{n}_i + 1)}{(2\pi)^3\ N\ I_p}$$

(3.38)

since

$$k_s = \frac{\omega_s\ \eta_s}{c} \quad .$$

This is the derivation of the result quoted as (36) in HG. The total cross-section is obtained by integration over frequency and solid angle.

b) Calculation of $S/Ld\Omega d\omega$

A quantity which is often measured is the ratio of scattered signal power to pump power per unit crystal length per unit frequency range and per unit solid angle; that is,

$$\frac{P_s}{P_p\ Ld\Omega d\omega} \equiv \frac{S}{Ld\Omega d\omega} \quad ,$$

where

$$S = \frac{P_s}{P_p} \quad .$$

(3.39)

From (3.31) and (3.32), we get

$$\frac{\langle n_s \rangle}{Ld\Omega d\omega} = \frac{N\eta_s}{\eta_p}\langle n_p \rangle \frac{d\sigma}{d\Omega d\omega} \quad .$$

- 46 -

Therefore,

$$\frac{S}{L d\Omega d\omega} = \frac{\omega_s}{\omega_p} N \frac{d\sigma}{d\Omega d\omega} \quad .$$

And substituting (3.38),

$$\boxed{\frac{S}{L d\Omega d\omega} = \frac{g_s \, \hbar \, \omega_s^3 \, (\bar{n}_i + 1) \eta_s^2}{(2\pi)^3 \, I_p \, c^2}} \qquad (3.40)$$

This shows the familiar ω_s^4 dependence of the scattered power in the high-loss region, (i.e. near resonance) since in this region $g_s \propto \omega_s$ [(3.25) and (3.27)] .

c) Calculation of $S/L d\Omega$

A convenient experiment is the measurement of right-angle scattering (i.e. $\theta = 90^\circ$). The results of these measurements are given in terms of a quantity $S/L d\Omega$,[46] where integration over frequency of $S/L d\Omega d\omega$ is performed by assuming a Lorentzian lineshape for the mode of interest. This will now be applied to (3.40):

$$\frac{S}{L d\Omega} = \int\limits_{\text{MODE}} \frac{g_s \, \hbar \, \omega_s^3 \, (\bar{n}_i + 1) \eta_s^2}{(2\pi)^3 \, I_p \, c^2} \, d\omega_i \quad . \quad (3.41)$$

Making the assumption of a "narrow" mode (that is, ω_s , η_s and $\bar{n}_i$ are assumed constant for the range of integration), (3.41) becomes

$$\frac{S}{L d\Omega} = \frac{\hbar \, \omega_s^3 \, \eta_s^2 \, (\bar{n}_i + 1)}{(2\pi)^3 \, I_p \, c^2} \int\limits_{\text{MODE}} g_s \, d\omega_i \quad .$$

This integrates to

$$\frac{S}{Ld\Omega} = \frac{\hbar \, \omega_s^3 \, \eta_s^2 (\bar{n}_i + 1)\Gamma \, g_s(\omega_0)}{16\pi^2 \, I_p \, c^2} \qquad (3.42)$$

since

$$g_s = \frac{\pi\Gamma}{2} \, g_s(\omega_0) \, \mathcal{L}(\omega_0 \, , \, \omega_i)$$

for a Lorentzian, and $\int \mathcal{L}(\omega_0 \, , \, \omega_i) \, d\omega_i = 1.$[47]
   Note that this agrees with the previously quoted result.[48]
(The linewidth there is defined as 2Γ ; hence the appearance of
the numerical factor of 8 in the cited reference.)

4. Calculation of Spontaneously Scattered Idler Power

The idler power (per unit pump power, solid angle and frequency
range) generated in spontaneous scattering will now be calculated.
Using the expressions for idler and signal photon numbers, (3.32)
and (3.35), and (3.25), it follows immediately that

$$\frac{P_i}{P_p \, d\Omega \, d\omega} = \left(\frac{\omega_i}{\alpha_i \, \omega_s}\right) \left(\frac{S}{Ld\Omega d\omega}\right) \qquad . \qquad (3.43)$$

A certain amount of care must be exercised in the application of
this equation to an experimental situation. This is discussed in
detail in Chapter V and in Appendix E.

5. Calculation of the Nonlinear Coefficients

This section is devoted to the development of a method for the
calculation of the nonlinear coefficients (d_E' and d_Q') of a material.

The method involves the calculation of d_Q' and d_E' separately the former is evaluated from right-angle scattering measurements; while the latter is computed from the measured second-harmonic generation coefficient. It is then shown how these computed co-efficients are related to the low-frequency electro-optic coefficient.

a) Calculation of d_Q'

To compute d_Q', the derived expressions for the on-resonance stimulated gain are equated. Starting with (3.15c)

$$g_s(\omega_0) = \frac{\omega_s \, \Omega_p^2 \, |A_p|^2 \, d_Q'^2}{\eta_s c \, \omega_0 \, \Gamma} \quad ,$$

and substituting (3.3) applied to the pump wave

$$\left[i.e., \quad |A_p|^2 = \frac{2\pi I_p}{c \eta_p} \right] \quad ,$$

we get

$$g_s(\omega_0) = \frac{2\pi \, \omega_s \, S_j \, \omega_0 \, I_p \, d_Q'^2}{c^2 \, \eta_s \, \eta_p \, \Gamma} \quad ,$$

where $\Omega_p^2 \equiv S_j \, \omega_0^2$ has been used (see discussion before(2.12)). But from (3.42),

$$g_s(\omega_0) = \frac{16\pi^2 \, c^2 \, (S/Ld\Omega) \, I_p}{\hbar \, \omega_s^3 \, \eta_s^2 \, (\overline{n}_i + 1)\Gamma} \quad ;$$

therefore,

$$\boxed{ d_Q' = \pm \left[\frac{8\pi c^4 \, \eta_p \, (S/Ld\Omega)}{S_j \hbar \omega_0 \, \omega_s^4 \, \eta_s(\overline{n}_i + 1)} \right]^{1/2} } \qquad (3.44)$$

b) <u>Calculation of d_E'</u>

The constant d_E' is related to usual second-harmonic d_{ijk} in the following way:

Going back to the derivation of the polarization terms, we see that the contribution due to d_E' is

$$P(\omega_s) = \frac{d_E'}{4\pi} E(\omega_p) E(\omega_i)^* .$$

Recalling the definition of d_{ijk},[69] and the discussion following (3.2), it is seen that

$$\boxed{d_E' = 16\pi\, d_{ijk}} \tag{3.45}$$

c) <u>Comparison to the Electro-optic Coefficient</u>[49]

Again returning to the original derivation of the polarization terms, we see that (neglecting the second-order term in d_Q')

$$P(\omega_s) = \frac{1}{4\pi} \left(d_E' + \sum_j \frac{\Omega_{p_j}^2\, d_{Q_j}'}{D_j(\omega_i)^*} \right) E(\omega_p)\, E(\omega_i)^*$$

$$= d'\, E(\omega_p)\, E(\omega_i)^*$$

where

$$d' = \frac{1}{4\pi} \left[d_E' + \sum_j \frac{\Omega_{p_j}^2\, d_{Q_j}'}{D_j(\omega_i)^*} \right] .$$

Far below the lowest resonant frequency (i.e., $\omega_i \ll \omega_{0_j}$)

$$D_j(\omega_i)^* = \omega_{0_j}^2 \quad ;$$

$$\therefore\quad d' = \frac{1}{4\pi} \left(d_E' + \sum_j \frac{\Omega_{p_j}^2}{\omega_{0_j}^2} d_{Q_j}' \right) = \frac{1}{4\pi} \left(d_E' + \sum_j \epsilon_j\, d_{Q_j}' \right) .$$

$$\tag{3.46}$$

(Note the similarity of this expression to (2.12),

$$\epsilon_{DC} = \epsilon_\infty + \sum_j S_j \Bigg).$$

But, from (3.9c),

$$d'_{Low\ freq} = 2\ \chi_{Low\ freq}$$

and from Butcher,[50]

$$\chi_{Low\ freq} = \frac{r\eta^4}{8\pi} \quad,$$

where r is the electro-optic coefficient and η is the optical refractive index. Therefore,

$$d' = \frac{r\eta^4}{4\pi} \quad,$$

or

$$\boxed{d'_E + \sum_j S_j\ d'_{Q_j} = r\eta^4} \qquad (3.47)$$

Thus, the calculated values of d'_E and d'_Q can be compared to the measured electro-optic coefficient through (3.47).

An alternate method for evaluating the ratio of d'_E/d'_Q is given in the literature.[37,51] This method, which compares the intensities of spontaneous scattering at the transverse resonant frequency and the longitudinal resonant frequency, was first applied to GaP. While this approach works well for a material with a single mode (such as GaP), the mathematics associated with applying it to a multimode material is rather complicated, and the solutions which are obtained are of restricted validity. Therefore, it is not used in this work.

d) Calculation of the Raman Susceptibility

Using the previous results, the Raman susceptibility is calculated by substituting (3.44) into (3.9b); this yields

$$\chi_R''(\omega_0) = \frac{c^4 \, \eta_p (S/L d\Omega)}{2\hbar\omega_s^4 \, \eta_s (\bar{n}_i + 1)\Gamma} \qquad (3.48)$$

In summary, this chapter contains the analysis of the stimulated and spontaneous scattering processes. The first part is devoted to a classical analysis of stimulated scattering. The important result of this part is the derivation of gain expressions for multimode materials which are valid over the entire mode. The latter half of the chapter contains a quantum mechanical analysis. The spontaneous scattering cross-section is calculated, and the cross-section is related to the stimulated gain expression. Methods for evaluating the nonlinear coefficients are developed, and an expression relating these coefficients to the electro-optic coefficient is presented.

We now turn to the application of these general results to the specific case of the transverse modes in $LiNbO_3$, since the experiments which will be described involved interactions with these modes.

CHAPTER IV

APPLICATION TO THE TRANSVERSE MODES IN LiNbO$_3$

A. INTRODUCTION

In this chapter, the calculations of the previous chapter
are applied to the transverse modes in LiNbO$_3$. Some background
material, pertinent to this work, is presented briefly, along with
the dispersion curve for the A$_1$-symmetry modes. Then the nonlinear
coefficients are calculated and compared to the measured electro-
optic coefficier   Finally, the scattering parameters for the two
important transverse modes—the 248 cm^{-1} and 628 cm^{-1} modes— are
caculated.

B. BACKGROUND

LiNbO$_3$ has been studied extensively and many of its properties
are described in the literature.[31,34,52,53] A brief summary of the
properties important for this work is given below.

LiNbO$_3$ is a uniaxial crystal in point group C$_{3v}$, with the
axis of symmetry defined as the c-axis. If a light beam traveling
through the material is polarized perpendicular to the c-axis (E $\perp$ c),
the appropriate index of refraction is η_0 , the ordinary index. If
the beam is polarized so that E $\parallel$ c , $\eta = \eta_e$, the extraordinary
index. Similarly, the normal modes of vibration of the crystal are
classified according to their symmetry with respect to the axes of
symmetry (the c-axis and the three mirror planes). Vibrations which
are symmetric with respect to both the c-axis and the mirror planes
are classified as A$_1$-modes. The existence of infrared and Raman activity
can be determined from Hertzberg[54] and it is found that the A$_1$ modes
are both infrared and Raman active. This ensures the existence of
d$_E{}'$ and d$_Q{}'$ and the possibility of producing tunable signals in
interactions with these modes.

The appropriate dispersion curve is the one obtained for $E \parallel c$, since the properties of this curve are determined by the A_1-symmetry modes. All of the quantities needed to evaluate the propagation characteristics have been measured by Barker and Loudon[31] and are tabulated in Fig. 4.1.

Plots of k_i' and k_i'' as functions of ν_i were obtained from Eq. (2.11), where k_i' and k_i'' are the real and imaginary parts of the propagation constant respectively. These computer-generated curves are shown in Fig. 4.2. The two large "bumps" on the k_i' plot are associated with the 248 cm^{-1} and 628 cm^{-1} vibrational frequencies. Therefore, the region for $\nu_i \approx 248$ cm^{-1} is called the "248 cm^{-1} mode" and similarly for $\nu_i \approx 628$ cm^{-1}, the region is called the "628 cm^{-1} mode." Consideration of the scattering from these two modes is the subject of the remainder of this study.

The wave vector matching condition is now imposed. The solution of Eq. (2.14) (see Fig. 2.4) yields a family of phase-matching lines. (Note that these lines depend upon the choice of pump frequency.) The values for η_p and η_s were taken from the data of Hobden and Warner,[55] using the equation for η_e. The computer generated phase-matching lines for a ruby laser pump $(\lambda_p = 6943$ Å$)$, superimposed on the A_1-symmetry dispersion curve, are shown in Fig. 4.3.

C. CALCULATION OF THE NONLINEAR COEFFICIENTS

In this section, the calculations of the nonlinear coefficients for the A_1-symmetry modes of $LiNbO_3$ are presented. The results are restricted to interactions in which all waves are polarized parallel to the c-axis, (extraordinary waves). This conforms to the experimental situation described in Chapter V.

Therefore, the pertinent nonlinear constants are those with subscript 333* (or 33 in contracted notation).[56]

_____

*In the conventional notation, the z-direction is taken along the c-axis, and this direction is also denoted by the numeral 3. Hence, d_{333} is the appropriate constant when all fields and polarizations are along the c-axis.

Mode Frequency	Oscillator Strength	Linewidth
ν_{oj}	S_j	Γ_j
(cm^{-1})		(cm^{-1})
248	16.0	21
274	1.0	14
307	0.16	25
628	2.55	34
692	0.13	49

$$\varepsilon_\infty = 4.6$$

$$\varepsilon_{DC} = \varepsilon_\infty + \sum_j S_j = 24.44$$

$$k^2 = \frac{\omega^2 \varepsilon(\omega)}{c^2} = \frac{\omega^2}{c^2}\left(\varepsilon_\infty + \sum_j \frac{S_j \nu_{oj}^2}{\nu_{oj} - \nu^2 - i\nu\Gamma_j}\right)$$

FIG. 4.1--Linear properties of A_1-symmetry mode: of $LiNbO_3$, as determined by infrared reflectivity measurements of Barker and Loudon.[31] The mode at 692 cm^{-1} has been identified as a combination band, since group theory predicts the existence of only four fundamental A_1 symmetry modes. Its contribution to the dielectric constant must be included.
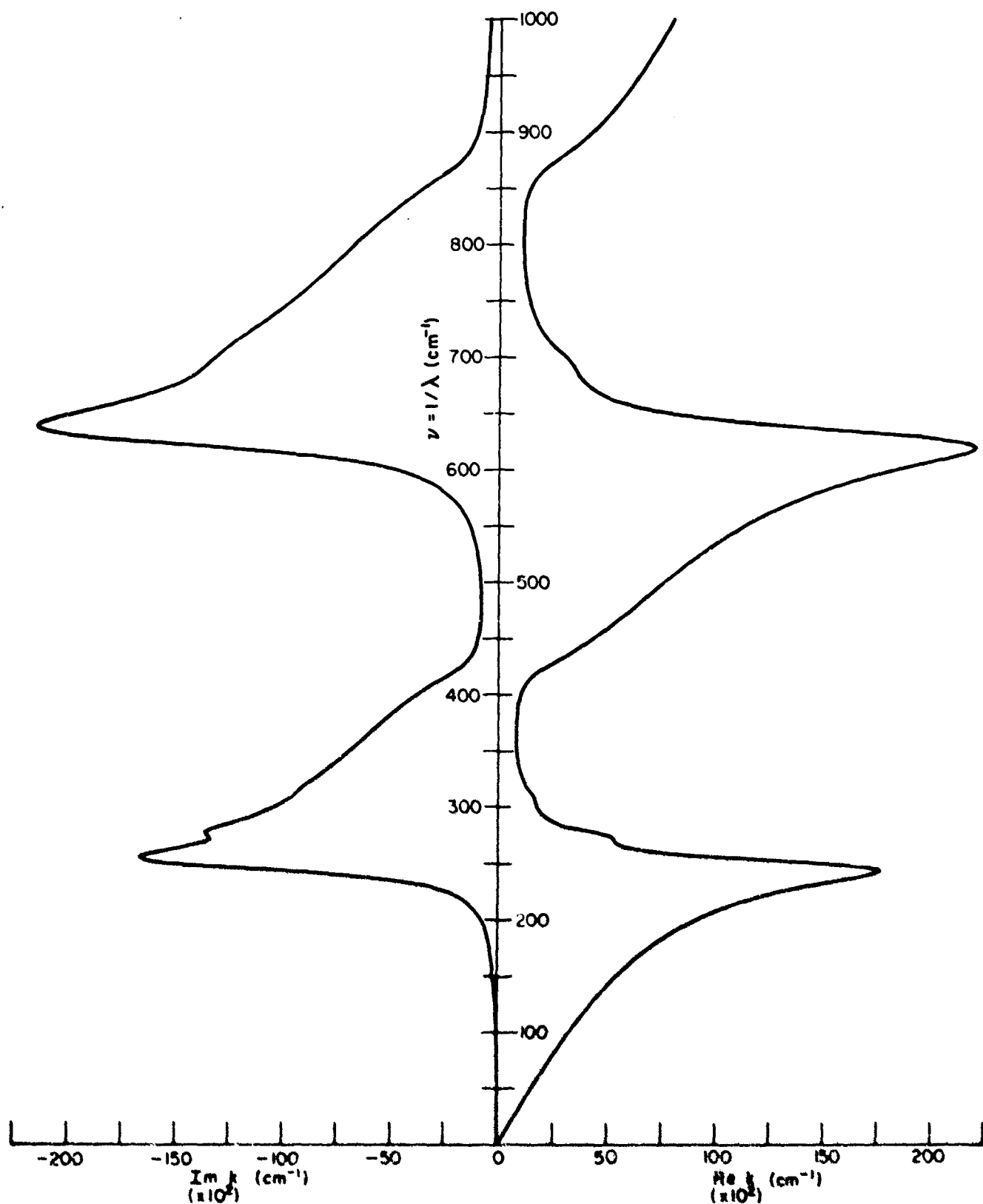
FIG. 4.2--The right side of the figure is the dispersion curve for the A_1-symmetry modes of $LiNbO_3$; the left side shows frequency vs electric field loss. The curves were generated from a computer program, using the data of Fig. 4.1.

$\underline{d'_E}$:

From Eq. (3.45),

$$d'_E = 16\Pi d_{33} = 5.28 \times 10^{-6} \text{ esu} \quad ,$$

where the latest published measurement of d_{33} has been used.[37]

$\underline{d'_Q}$:

From Eq. (3.44),

$$|d'_Q| = \left[\frac{3\pi c^4 \eta_p (S_{33}/Ld\Omega)}{S_j \hbar\omega_0 \omega_s^4 \eta_s (\bar{n}_i + 1)} \right]^{1/2} \text{ esu} \quad .$$

The values of $S_{33}/Ld\Omega$ for the modes of LiNbO$_3$ have been measured[40] and the resulting values for d'_Q are tabulated in Fig. 4.4.*

Raman susceptibility:

The Raman susceptibility is calculated from Eq. (3.48) using the measured values of $S_{33}/Ld\Omega$. The results are tabulated in Fig. 4.4.

Finally, these results are compared to the measured electro-optic coefficient through Eq. (3.47). Turner has reported[45]

$$r_{33} = 30.8 \times 10^{-10} \text{ cm/v} = 9.24 \times 10^{-7} \text{ esu} \quad ,$$

---

*There is an arbitrariness in the determination of the sign of d'_Q . The approach of Kaminow and Johnston[46] will be followed in this regard. This leads to negative values of d'_Q for the 274 cm^{-1} and 307 cm^{-1} modes. It should be pointed out that GaP has a negative value of d'_Q (or equivalently a ratio of $(d'_E/d'_Q) < 0$).[54] In addition, it should also be noted that arbitrarily choosing the signs of each d'_Q to be positive would increase the calculated electro-optic coefficient by only about 20%.
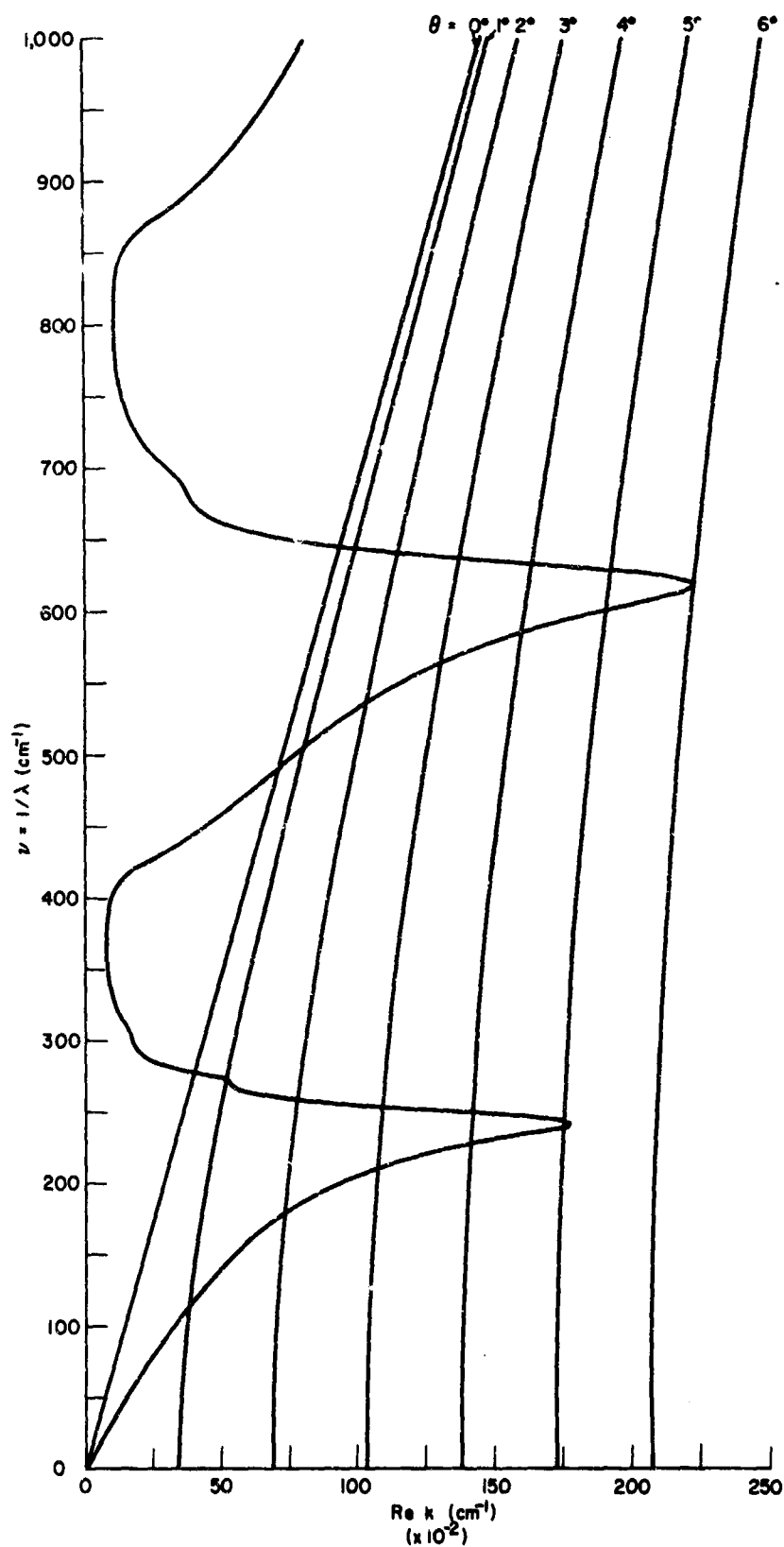
- 57 -

FIG. 4.3--The phase-matching lines for a ruby laser pump ($\lambda_p = 6943$ Å) are super-imposed on the dispersion curve of Fig. 4.2. The optical refractive index data of Hobden and Warner[55] were used.

- 58 -

ν_o	S	Γ	Ω_p^2	$\bar{n}_1 + 1$	$S_{33}/Ld\Omega$	$d_Q'^d$	$\chi_R''(\nu_o)$
			$\times 10^{-4}$		$\times 10^{+6}$	$\times 10^{+6}$	$\times 10^{+12}$
Units cm^{-1}		cm^{-1}	cm^{-2}		cm^{-1}sr^{-1} esu	esu	esu
248	16.00	21	98.5	1.43	16.0	+ 1.2	5.3
274	1.00	14	7.5	1.34	4.0	- 2.3	2.1
307	00.16	25	1.5	1.25	0.95	- 2.8	0.3
628	2.55	34	100.0	1.05	10.2	+ 1.8	3.1

$$d_E' = 5.28 \times 10^{-6} \text{ esu}$$

$$d_E' + \sum_j S_j d_{Q_j}' = 2.53 \times 10^{-5} \text{ esu}$$

^{d}See text for discussion of sign of d_Q'.

Fig. 4.4--Tabulated properties of the A_1-symmetry modes of LiNbO$_3$. The values of d_E', d_Q' and $\chi_R''(\nu_o)$ are the significant results of this section.

and therefore

$$\eta^4 r_{33} = 2.36 \times 10^{-5} \text{ esu} \quad .$$

A comparison of this result to the calculated value of $d_p' + \sum_j S_j d_{Q_j}'$ (Fig. 4.4) shows the two to be in excellent agreement.

D. SCATTERING PARAMETERS FOR THE 248 CM^{-1} AND 628 CM^{-1} MODES

Using the constants calculated in the previous section and the development of Chapter III, we devote this section to the computation of the scattering parameters for the 248 cm^{-1} and 628 cm^{-1} transverse modes in $LiNbO_3$. With reference to Fig. 4.2, several comments are in order before proceeding with the calculation. These comments are intended to point out two distinctions between the modes, which are pertinent to these calculations:

a) The absorption $(\alpha_i = 2 k_i'')$ along the 628 cm^{-1} mode is high over the entire mode, varying from 14×10^2 cm^{-1} at the $\theta = 0^\circ$ point to 200×10^2 cm^{-1} for phase-matching at 6°. Since stimulated gains are of the order of 1-10 cm^{-1} for pump powers available from standard Q-switched lasers, the idler loss is always much greater than the gain and the high loss approximation, Eqs. (3.15) or (3.18b), is valid over the entire mode.

The high-loss approximation does not apply to the case of the 248 cm^{-1} mode however, since the loss varies from approximately zero to 50×10^2 cm^{-1} over the near-forward scattering region. Hence, the more general expression is required.

b) Referring to the $\theta = 0$ line in Fig. 4.3, it is seen that collinear scattering from the 628 cm^{-1} mode is possible and indeed has been observed.[22,23] For the 248 cm^{-1} mode, on the other hand, collinear forward scattering is not obtainable, since the intersection of the $\theta = 0$ line occurs at $v_i = 0$. Thus, the collinear gain

expression, Eq. (3.16), is not strictly applicable at any point on this mode.

Using calculated coefficients, numerical values for the signal stimulated gain (g_s) were computed for the two modes and the results are plotted in Fig. 4.5. These curves are for a pump power density of 5×10^8 W/cm^2, typical of focused Q-switched lasers and the approximate power density used in the experiments to be described later. Note, that for all points on the dispersion curve, except those very near to $\nu_i = 0$, g_s is greater for scattering from the 248 cm^{-1} mode than for the 628 cm^{-1} mode.

Figure 4.6 shows the calculated idler power (divided by signal power) as a function of frequency for stimulated scattering from the two modes. Again, it is noted that in scattering from the 248 cm^{-1} mode, the ratio P_i/P_s exceeds that from the 628 cm^{-1} mode by more than an order of magnitude.

Similar plots for the spontaneous case are given in Figs. 4.7 and 4.8 where $P_s/P_p L \, d\Omega d\omega$ and $P_i/P_p d\Omega d\omega$ are plotted for both modes. As for the stimulated process, the scattered power (both signal and idler) is greater for the 248 cm^{-1} mode than the 628 cm^{-1} mode. The shape of the curve for the 628 cm^{-1} mode in Fig. 4.7 has been verified expermentally by Puthoff, et al,[17] whose measurements indicated a nearly constant signal power with frequency in spontaneous scattering for this mode.

In the next chapter, we shall compare the theoretical predictions to the experimental results. The agreement between theory and experiment will be seen to be good for both stimulated and spontaneous scattering.
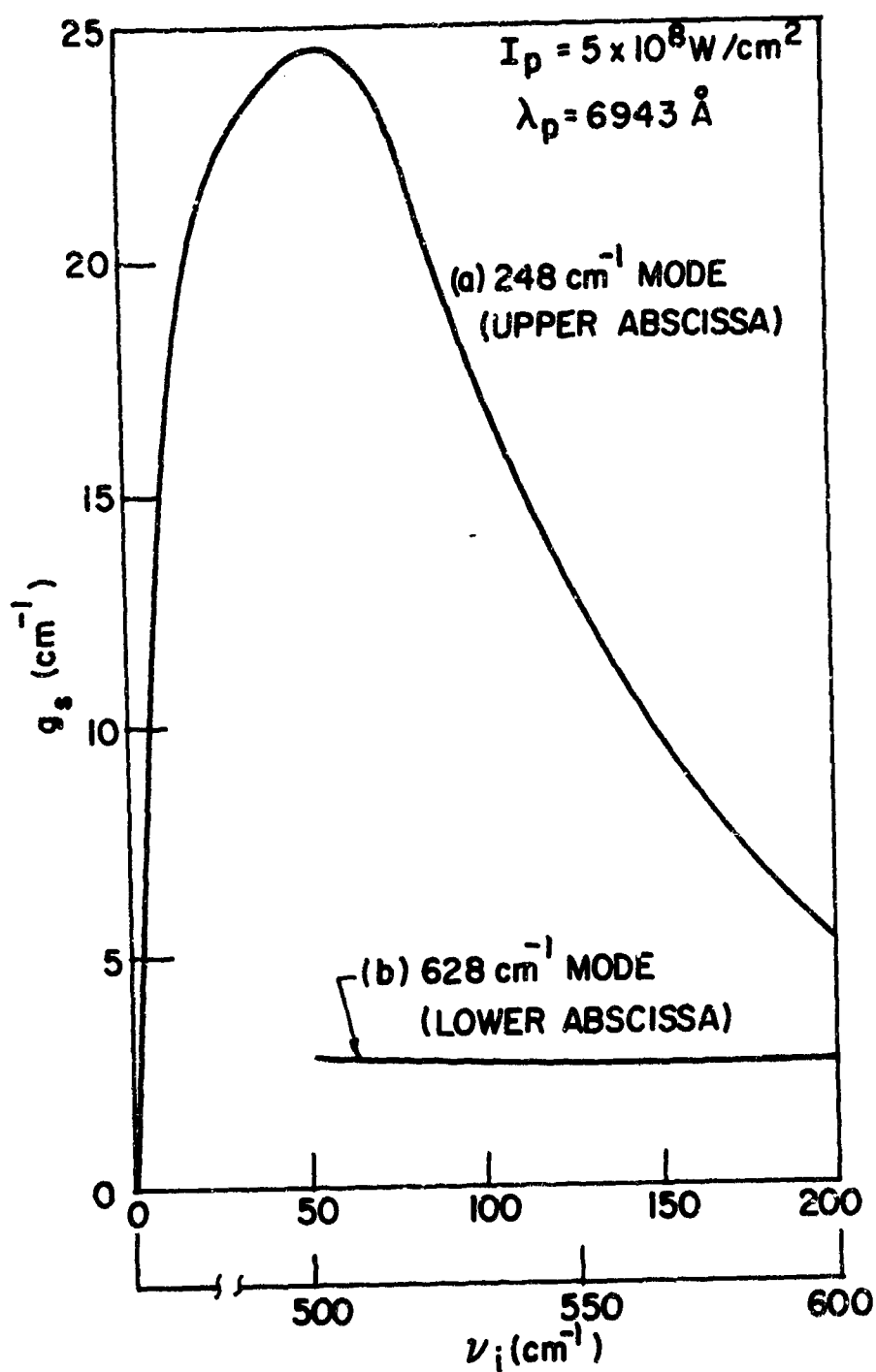
FIG. 4.5--Plots of stimulated gain coefficient (g_s) as a function of idler frequency for the 248 cm^{-1} mode (Curve a) and the 628 cm^{-1} mode (Curve b). Equation (3.20) and the calculated constants of Fig. 4.4 were used to plot the curves.
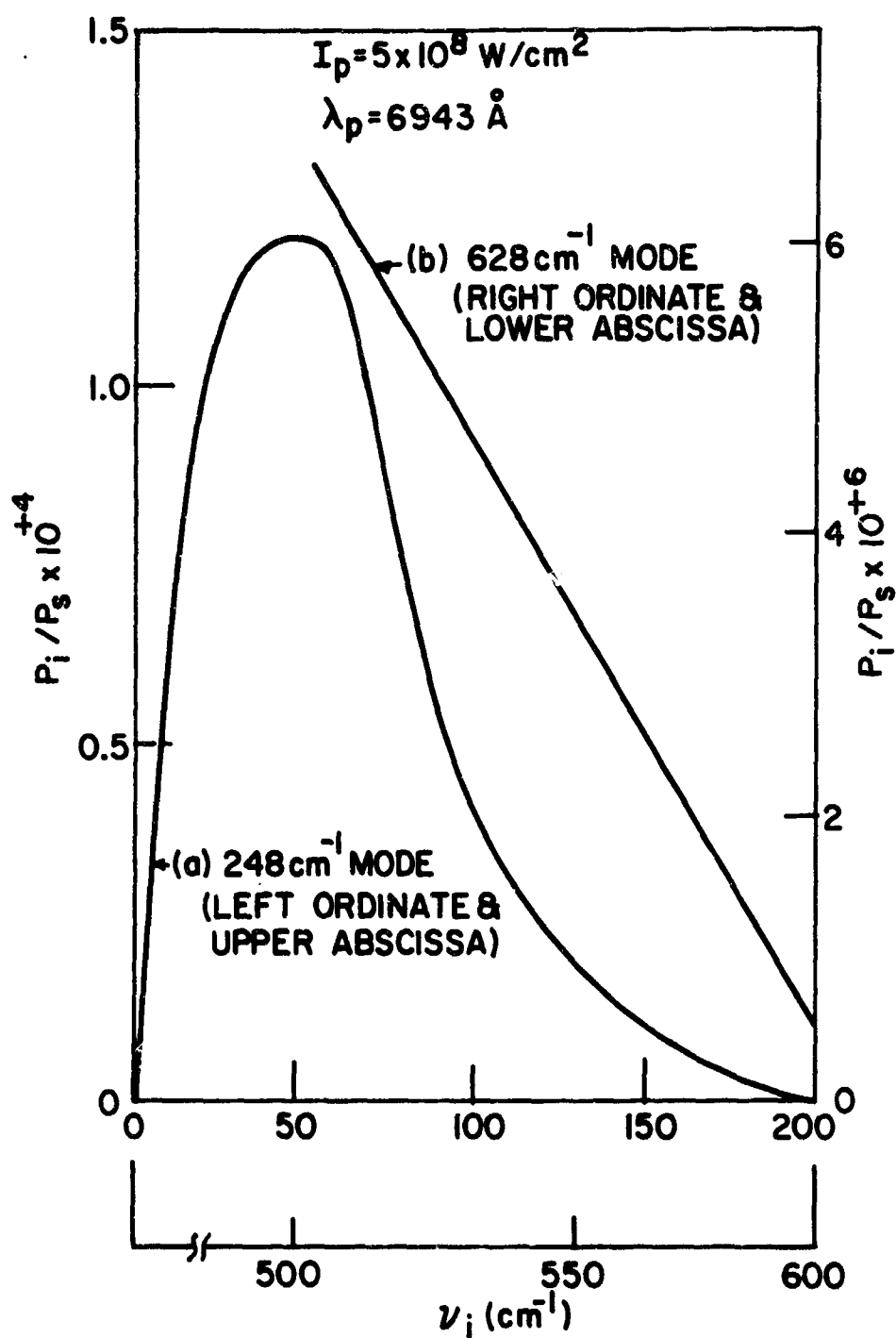
FIG. 4.6--Idler power (divided by signal power) generated in stimulated scattering from the 248 cm^{-1} mode (Curve a) and the 628 cm^{-1} mode (Curve b). Note the use of different ordinates for the two modes. Equation (3.26) and the calculated constants of Fig. 4.4 were used to plot the curves.

FIG. 4.7--Signal power (per unit pump power, crystal length, solid
angle, and bandwidth) generated in spontaneous scattering
from the 248 cm^{-1} mode (Curve a) and the 628 cm^{-1} mode
(Curve b). Note the use of a logarithmic ordinate scale.
For small ν_i, Curve a "turns around" and intersects the
origin; this has been omitted for clarity. Equation (3.40)
...nd the calculated constants of Fig. 4.4 were used to p'..t
the curves.

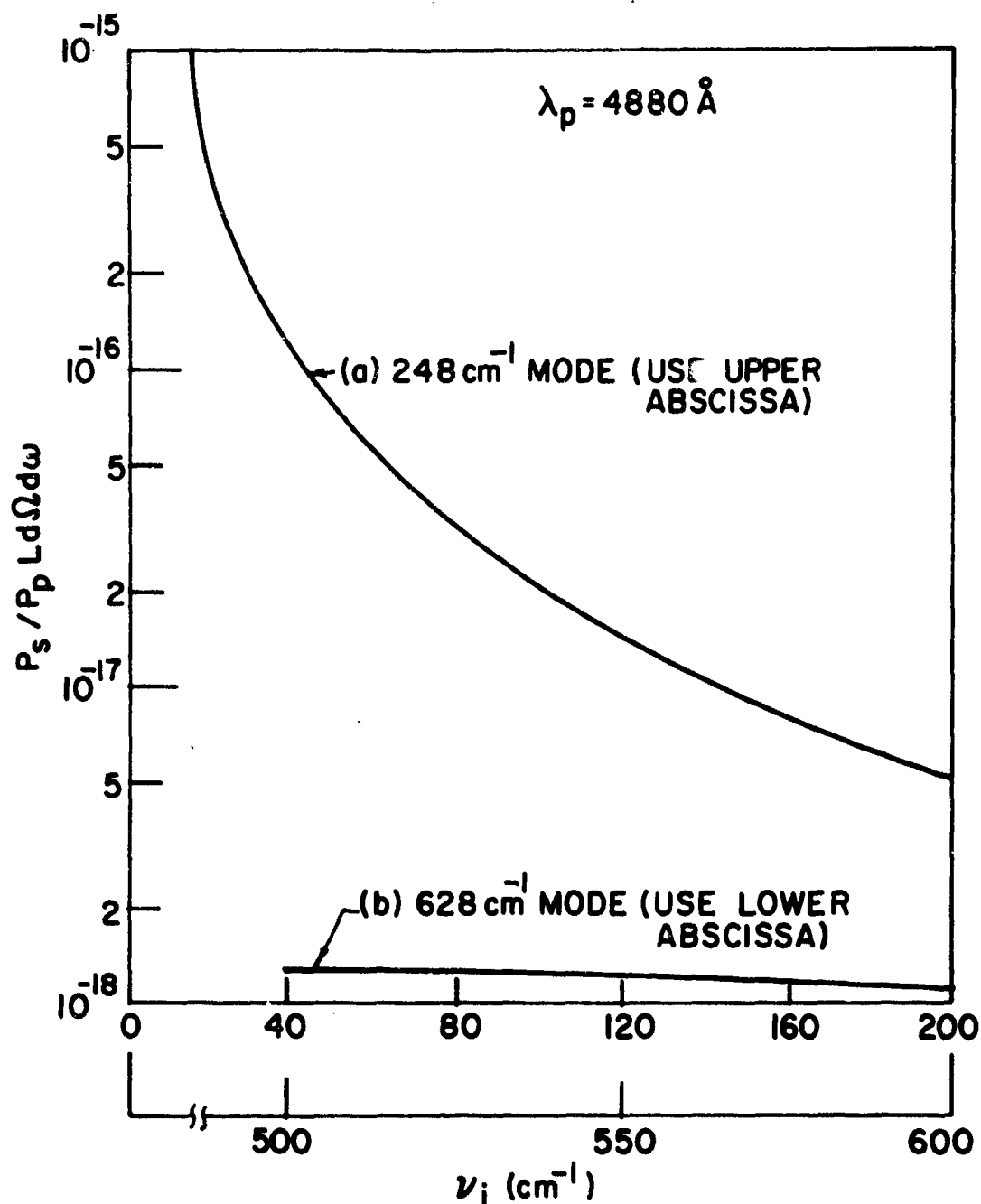FIG. 4.8--Idler power (per unit pump power, solid angle and bandwidth) generated in spontaneous scattering from the 248 cm⁻¹ mode (Curve a) and the 628 cm⁻¹ mode (Curve b). The ordinate scale is logarithmic. For small ν_i, Curve a "turns around" and intersects the origin; this has been omitted for clarity. Equation (3.43) and the calculated constants of Fig. 4.4 were used to plot the curves.
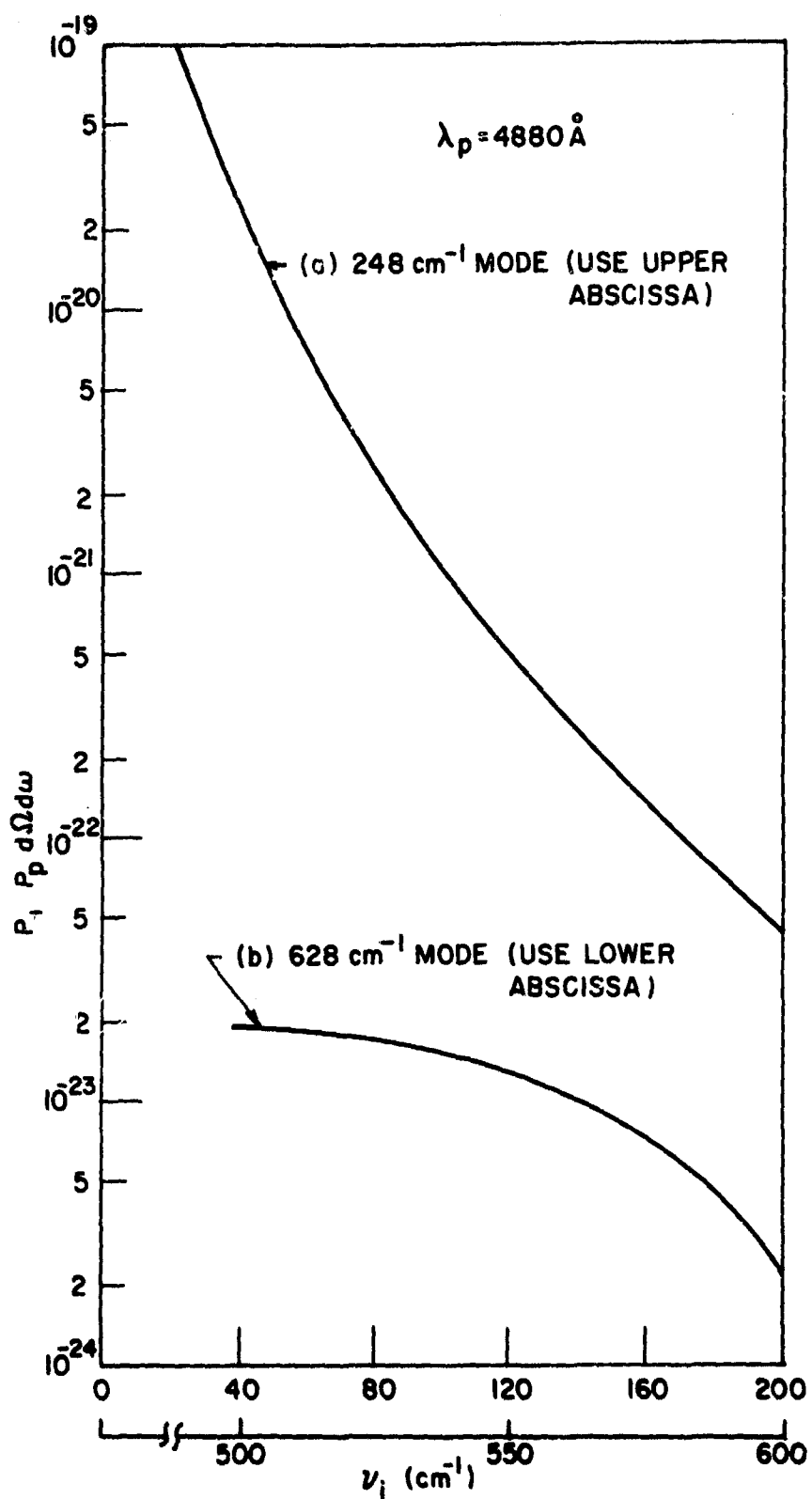
CHAPTER V

EXPERIMENTAL EFFORT

A.   INTRODUCTION

The experimental effort was divided into three areas:

a) The first set of experiments was an attempt to detect the idler (infrared) power generated in spontaneous scattering from the 628 cm^{-1} mode. An argon-ion laser was built, and a phase-sensitive detection system was assembled. This experimental set-up is adaptable to a wide variety of scattering measurements. The experiment was not definitively successful, in that the detection of the idler could not be conclusively verified.

b) Next, a series of stimulated scattering experiments using a Q-switched ruby laser were performed. The most significant experiments yielded tunable stimulated optical emission in scattering from the 248 cm^{-1} mode. No external resonator was required to produce the tunable output. In addition, the idler wave involved in this process was detected. All of the measured parameters agree reasonably well with the theory presented in the previous chapters.

c) Finally, measurements of spontaneous scattering from the 248 cm^{-1} mode were made. Both the frequency and magnitude of the scattered signal as a function of phase-matching angle θ were measured and found to agree well with prediction.

B.   INFRARED GENERATION BY SPONTANEOUS SCATTERING FROM THE 628 cm^{-1} MODE.

At the start of the experimental program, tunable stimulated Raman scattering had not as yet been observed. Measurements of the tunable signal in spontaneous scattering from the 366 cm^{-1} mode in GaP,[32] the 414 cm^{-1} mode in ZnO,[59] and the 628 cm^{-1} mode in $LiNbO_3$,[17] had recently been performed. Starting with the results of the last work, the objective of the first part of the experimental program was the detection of the tunable idler power generated in spontaneous scattering from the 628 cm^{-1} mode in $LiNbO_3$. The two quantities

of interest are the frequency tuning and the idler power.

The tuning curve is obtained from the computer generated data used to plot Fig. 4.3. Since the three wave vectors are available for each value of θ , the angle φ is calculable. The result is plotted in Fig. 5.1. Note that φ is large over most of the tuning range. Due to the large index of refraction at the idler, most of the infrared power would undergo total internal reflection upon striking a surface normal to the incident laser beam. For this reason, the crystal was cut at $45°$ at the output face as shown in Fig. 5.2. The calculated external tuning curve is also shown in this figure and it is seen that a tuning range of 525 cm^{-1} to 595 cm^{-1} (17 μ to 19 μ) is expected.

The scattered infrared power was calculated from the results of Chapter IV, with particular reference to Fig. 4.8, where $P_i/P_p \, d\Omega d\omega$ is plotted as a function of ν_i . However, we are interested in the scattered idler power in a specified frequency interval and solid angle as a function of φ' (defined in Fig. 5.2). This is shown in Appendix E to be:

$$P_i \;=\; \left(\frac{P_i}{P_p\,d\Omega d\omega}\right)\left(\frac{\Delta\omega_i P_p}{(d\varphi/d\theta)}\right)\left(\frac{H}{r}\right)\left(\frac{\Delta\varphi'}{\eta_i}\right) \qquad . \qquad (5.1)$$

In the above expression:

P_i is the idler power in a frequency range $\Delta\omega_i$ scattered into an aperture of height H at a distance r from the crystal output, $\Delta\varphi'$ is the angle increment corresponding to $\Delta\omega_i$ (see Fig. 5.2) ,

and

$d\varphi/d\theta$ is calculated from Fig. 5.1.

A sketch of the geometry is given in Appendix E. Carrying through this calculation for $\frac{H}{r} = 0.1$ and $P_p = 0.5$ W we get a total power over the tuning range of about 3×10^{-12} watts. If the range is
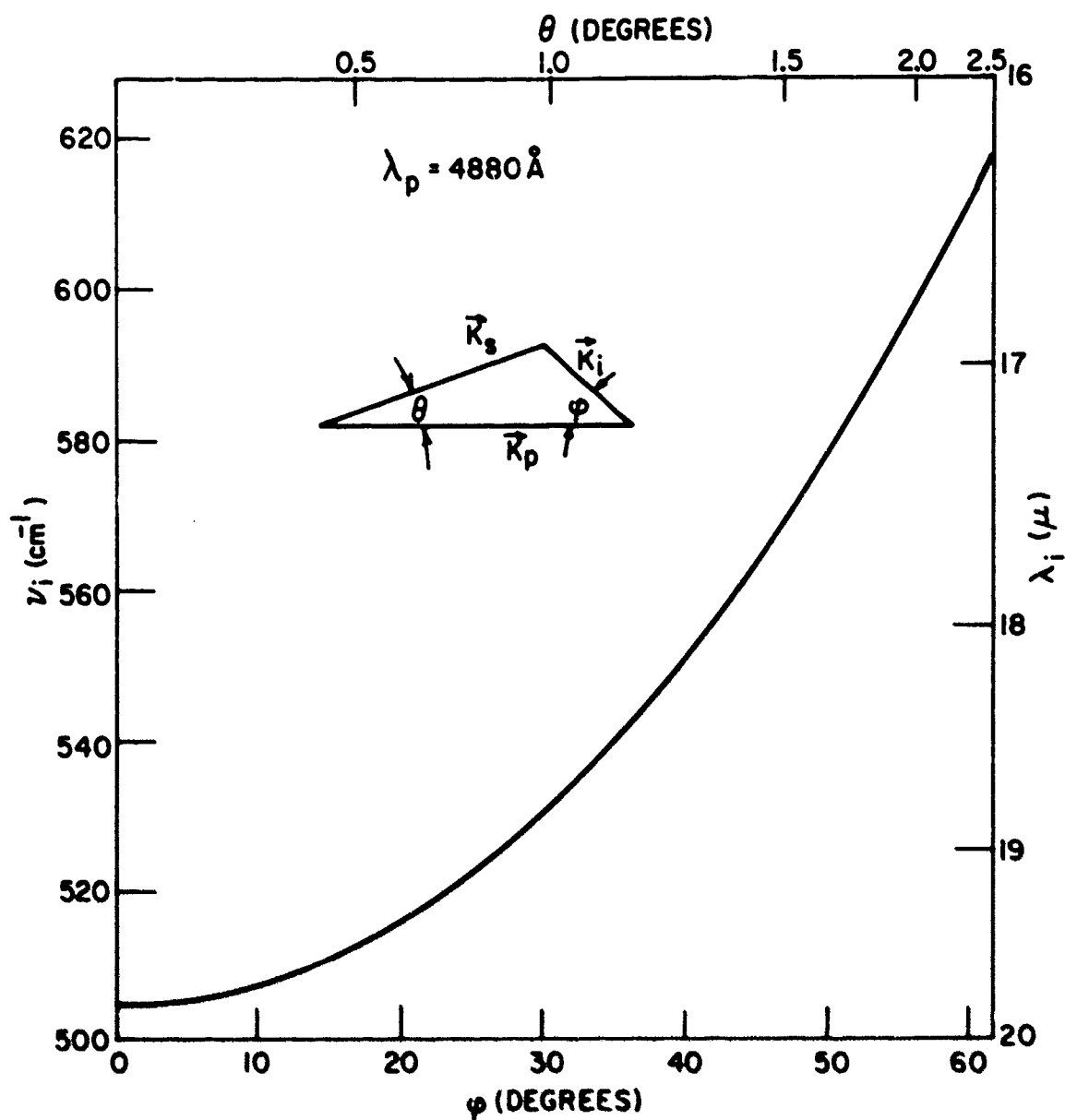
FIG. ?.1.--Idler frequency vs the angle φ for scattering from the
29 cm⁻¹ mode, using an argon laser pump (λp = 4880 Å).
The idler wavelength is shown at the right; the phase-
matching angle θ is shown at the top. φ and θ are
defined in the phase-matching triangle.

- 68 -

FIG. 5.2--Idler frequency vs the external angle for scattering from the 628 cm^{-1} mode. The 45° cut was taken in the output face of the crystal to maximize the tunability. From Snell's law, $\sin \varphi' = \eta_i \sin (\varphi - 45°)$.

divided into six segments, (each encompassing a $\Delta\varphi'$ of about 15° and a Δv_i of 10 cm^{-1}), the power in each segment is about 0.5×10^{-12} watts. As will be described later, this is only slightly above the limit of detectability of the phase sen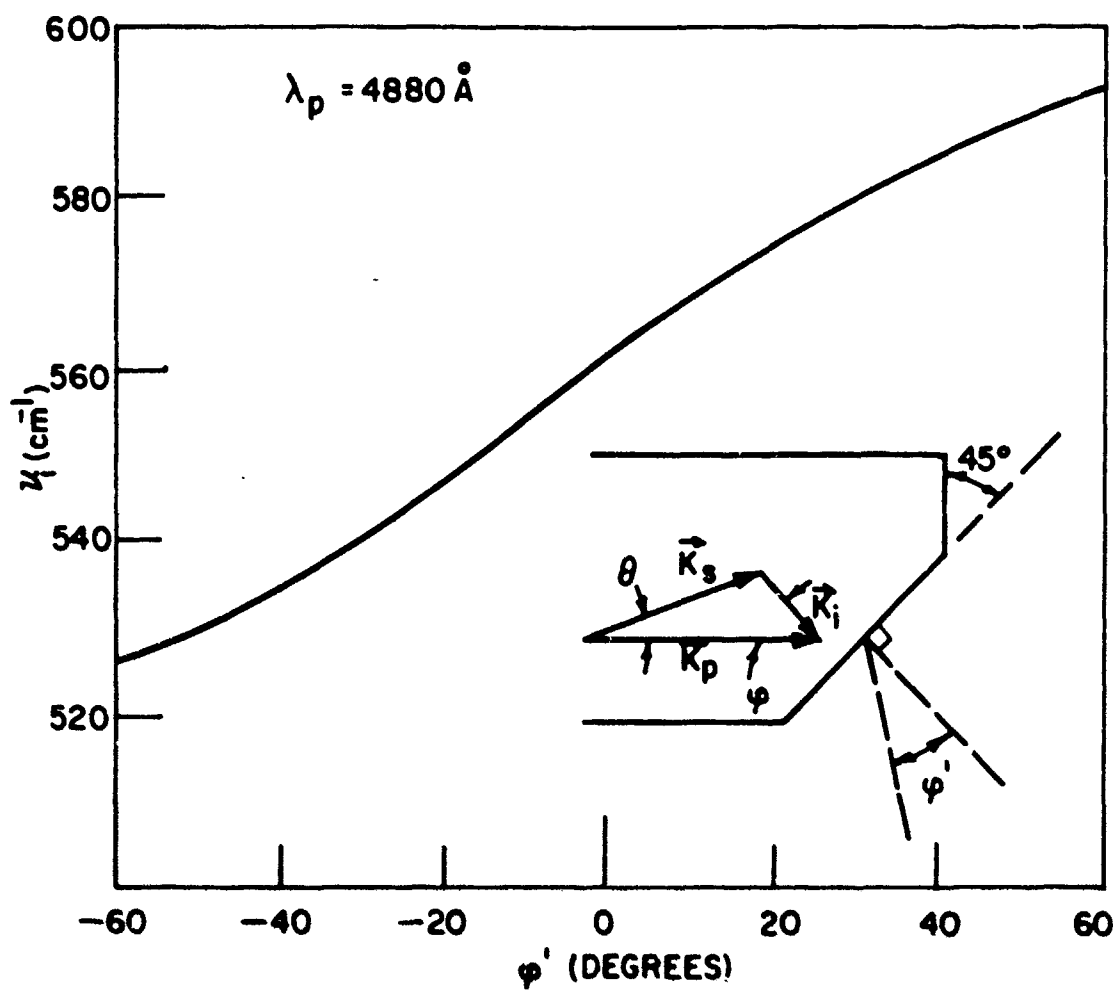sitive detection system employing the Ge:Cu detector. Even though the probability of success of the experiment appeared marginal, the significance of the result (if achievable) justified the experimental attempt. In addition, the calculated tuning curve is valid for stimulated scattering, and would be useful in such experiments.

Most of the previously reported scattering measurements[17,32,59] used a He-Ne laser (6328 Å) as the pump source. The use of an argon laser instead has the following advantages:

a) The argon laser has a power output of about an order of magnitude greater than the highest power conventional He-Ne laser. It is comparatively easy to get an output of 500 mW at 4880 Å using the argon laser, while 100 mW is the output of the highest power commercially available He-Ne laser. Since the scattered power is proportional to pump power, this advantage is obviously significant.

b) The shorter wavelength is also an advantage for two reasons. First, scattered power is proportional to the fourth power of a signal frequency [see (3.40)]. This yields about a factor of 3 increase in scattering efficiency for a 4880 Å pump compared to a 6328 Å source. Secondly, since most phototubes are more sensitive in the green-blue spectral region than in the red, it is possible to detect weaker scattered optical signals with a 4880 Å pump.

c) Finally, several wavelengths are available from an argon laser (including the two strong lines at 4880 Å and 5145 Å). This may be useful in certain experiments.

For these reasons, the argon laser was selected as a pump source We also decided to construct the laser in-house, employing rf excitation,[60] and incorporating several features not available in commercial units:

(1) A self contained vacuum system, including both roughing and Vac-ion pumps. This system allows for adjustment and monitoring of operating gas pressure as well as regular "flushing" of the system.

(2) Isolated supplies of argon gas. This permits operation of the system with other gases, e.g., krypton.

(3) Ball-socket construction of end windows allows for relatively easy cleaning and/or replacement of Brewster angle windows.

(4) Interchangeable parts. A spare laser tube was built and was easily installed into the system after failure of the initial tube.

(5) Mirror flexibility. The external mirror mounts provide simplicity of alignment and adjustments of the optical cavity, as well as easy interchangeability. The system operates with a 6m spherical (~5% transmission) output mirror. The back mirror is either a totally reflecting flat which yields output at all wavelengths simultaneously or a prism with a totally reflecting back face which allows lasing action at a single wavelength only. In this latter configuration, the output wavelength can be changed from one of the lasing lines to another simply by rotating the prism.

In addition, the in-house construction of the laser resulted in a working system at considerably less expense than comparable commercially available lasers. A photograph of the laser system is shown in Fig. 5.3. (An aluminum box was built around the laser, subsequent to the taking of the photograph, to reduce pickup in the detection system.)

The laser performance was very close to the design goals, with a total power output of about 1.25 watts; the power was divided among the various wavelengths as shown:

Wavelength ($\overset{o}{A}$)	Power (MW)
4727	50
4765	130
4880	600
4965	100
5018	20
5145	340

FIG. 5.3--Photograph of the argon laser system. The excitation is supplied
by a 3 MHz oscillator (shown in background center). The interchangeable
Brewster's angle windows are at the ends of the tube. The coated prism is
in the mirror mount at the far left of the table; the beam emerges from the
output mirror, which is at the far right of the table. The system is evacu-
ated with a roughing pump (not visible) and a Vac-ion pump (near center of
photograph). The argon gas is stored in the flasks seen in the foreground;
the hoses are for water cooling of the tube.

The limitation on the power output of the laser was imposed by the oscillator: its maximum output was about 5 KW.

Detection of the scattered signals was accomplished using a phase-sensitive detection system, employing a lock-in amplifier (Princeton Applied Research Corp., Model HR-8). The main features of this technique, which is described in detail in the literature,[61-63] are summarized below:

The signal, which is chopped at a fixed frequency, is amplified in a low-noise signal amplifier whose center frequency and bandwidth are variable. Simultaneously, the chopper generates a reference signal (by means of a light bulb and phototube) which is amplified in a reference channel. The reference and signal are then mixed and a dc output, proportional to the magnitude of the signal and the cosine of the phase angle between the signal and reference, is obtained. This is then passed through RC low pass filtering.

The primary advantage of this system is that it can extract weak signals from the noise background. This is accomplished primarily by narrowing the bandwidth of the signal channel to eliminate white noise and by synchronously comparing the signal and reference.

The detector employed in the experiment varied with the type of measurement being made. For optical measurement, a photomultiplier tube was used, while for the infrared measurements, a Ge:Cu semi-conductor detector cooled to liquid helium temperature was employed. This is described in more detail below.

The experimental apparatus is shown in Fig. 5.4. The laser beam was chopped at a 1 kHz rate, while a reference signal was simultaneously generated. The laser beam then entered the $LiNbO_3$ crystal as an extraordinary wave and was totally internally reflected at the 45° cut in the output face. The acceptance angle of the idler output was determined by an aperture, and the detected band of idler frequencies was varied by translation and rotation of the adjustable mirror. After passing through a $\frac{1}{4}$ meter Jarrel Ash monochromater, which had a grating blazed at 18 μ, the signal was detected in the Ge:Cu detector; the output of this detector was fed into the signal channel of the lock-in
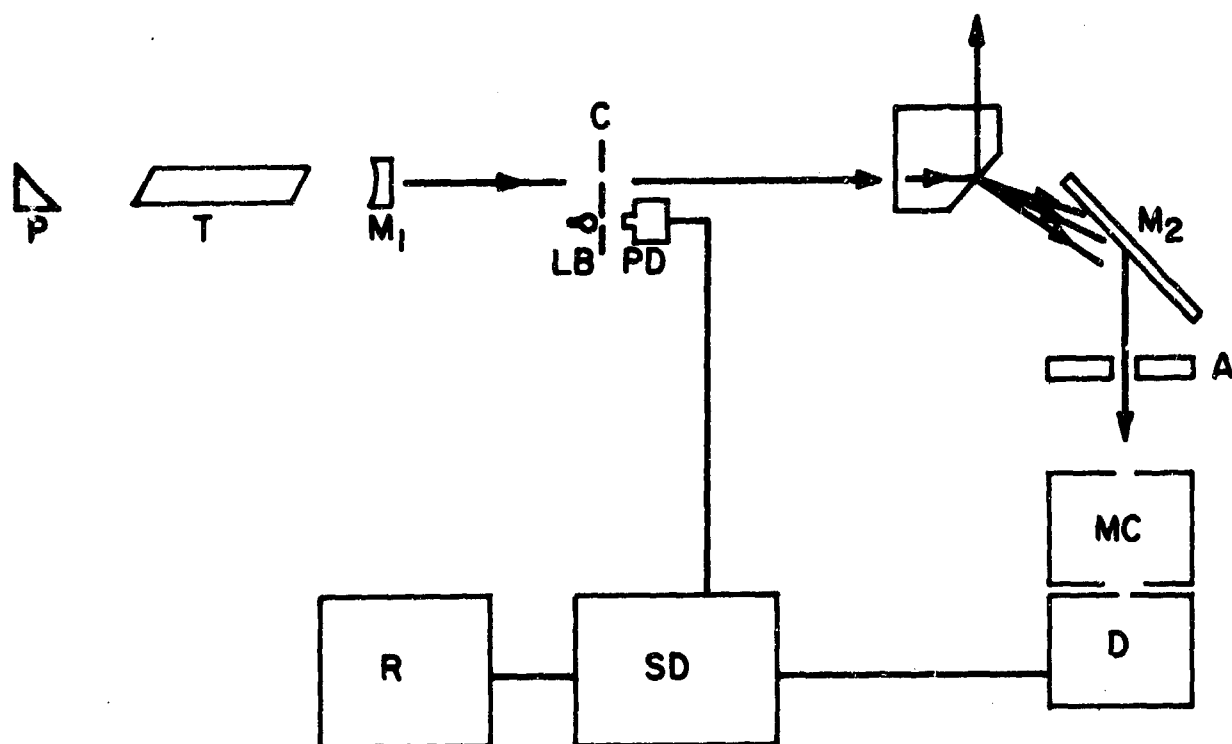
FIG. 5.4--Experimental apparatus for detecting scattered idler radiation.
The laser (shown schematically as a tube, T , a mirror, M_1 , and a
coated prism, P) output beam (about 500 mW of power at 4880 Å) was chop-
ped at a 1 kHz rate by the chopper, C , while a reference signal was
generated simultaneously as the photodetector, PD , detected the chop-
ped output of a light bulb, LB . The beam passed through the $LiNbO_3$
crystal, XTAL , as an extraordinary wave (the laser polarization and
the c-axis of the crystal were both normal to the paper). The laser beam
was totally internally reflected at the 45° cut in the output face. The
idler radiation was reflected by the rotatable, translatable mirror, M_2 ,
through the aperture, A . It then passed through the monochromator,
MC , and was detected by the Ge:Cu detector, D , which was cooled to
$4^\circ K$ in a dewar. The detector output and the reference signal were fed
into the PAR Model HR-8 synchronous detector, SD ; the output of the
detection system was monitored by a chart recorder, R .

amplifier. Finally, the dc output of the amplifier was recorded on a chart recorder.

The performance of the detector was one of the crucial parameters affecting the success of the experiemnt. A Ge:Cu detector, purchased from Santa Barbara Research Center, a subsidiary of Hughes Aircraft Company, was used. The properties of this type of detector have been discussed in the literature.[64,65] Its most significant features, as far as this experiment was concerned, were its high detectivity and responsivity, low noise equivalent power and speed of response. Its major disadvantage, as compared to a Golay cell, for example, is that cooling to 4.2°K is required. Based upon the detector parameters supplied by the manufacturer, it was estimated that by using the phase-sensitive detection system it would be possible to detect a signal of approximately 10^{-13} watts. This is only a factor of two larger than the expected power output through the aperture in Fig. 5.4.

With the experimental set-up shown, no idler signal was observed. Since the calculations indicated that the signal power was marginal for detection, this result, although disappointing, was not too surprising. Attempts to focus the signal using Ge lenses failed, (probably because of line-up inaccuracies). Finally, the mirror, aperture, and the monochromator were removed and the crystal was mounted inside the dewar at a distance of about $\frac{1}{4}$ inch from the detector. For this configuration, the solid angle viewed by the detector (and hence the signal power) was increased by about two orders of magnitude, and the losses in the path from the crystal to the detector were eliminated. Signals were now observed at about the predicted level. However, it was then ascertained that the Ge:Cu detector was sensitive to visible radiation. Since the infrared signal was predicted to be about 12 orders of magnitude below the pump power, it was difficult to rule out the possibility that the detector was responding to stray pump light, rather than to infrared radiation. Various attempts to prevent the visible radiation from reaching the detector were then made, but the results were inconclusive.

In summary, it could not be conclusively established that the detection of the infrared power had been achieved.

C. TUNABLE OPTICAL AND INFRARED GENERATION BY STIMULATED SCATTERING FROM THE 248 cm^{-1} MODE.

The reports[22,23] of stimulated scattering from LiNbO$_3$ led to a redirection of the experimental effort to the study of tunable infrared power in _stimulated_ scattering from the 628 cm^{-1} mode. Early in the course of the stimulated experiments, a new process-tunable, stimulated optical scattering from the 248 cm^{-1} mode, _without_ an external resonator- was observed. In addition, the tunable infrared wave generated in this process was detected. The experiments have been reported,[24] and a more detailed account has been given by Yarborough.[66] The highlights of the experiments, particularly those features which relate to the theory developed in this work, are summarized below.

The experimental apparatus is shown in Fig. 5.5. The pump was a Q-switched ruby laser emitting ~ 20 nsec pulses with a peak power of approximately 1 MW and a spot size at the laser of about 2 mm. A lens focused the beam into a 3.3 cm a-axis crystal, with the laser polarized along the c-axis. The end faces of the crystal were polished flat and parallel to within a few seconds of arc. Temporal behavior of the input pump, output pump, and signal was recorded with photodiodes and the wavelengths were recorded on film at the output of a 1 m grating spectrometer. The spatial separation of the beams was detected by photographing the beams on a screen.

Figure 5.6 shows the output wavelengths and spatial distributions of the signal for two different angles of incidence, ϕ , between the pump beam and surface normal. A 50-cm focal-length lens was used in both cases. With this focal-length lens, crystal damage was not observed. Figure 5.6(a) shows the spectrometer output for the case of normal incidence $\phi = 0°$, and 5.6(b) shows the corresponding spatial separation at a distance of 5.6 m from the crystal. This separation implies an angle of 0.42° between the signal and pump beams inside the crystal. The observed frequency shift in this case is 50 cm^{-1}, and the observed spatial separation agrees with this shift. This point is plotted as point A on the dispersion curve in Fig. 5.7. Figures 5.6(c) and 5.6(d) show the spectral and spatial outputs from the crystal for an angle of incidence $\phi = 2.30°$. The observed
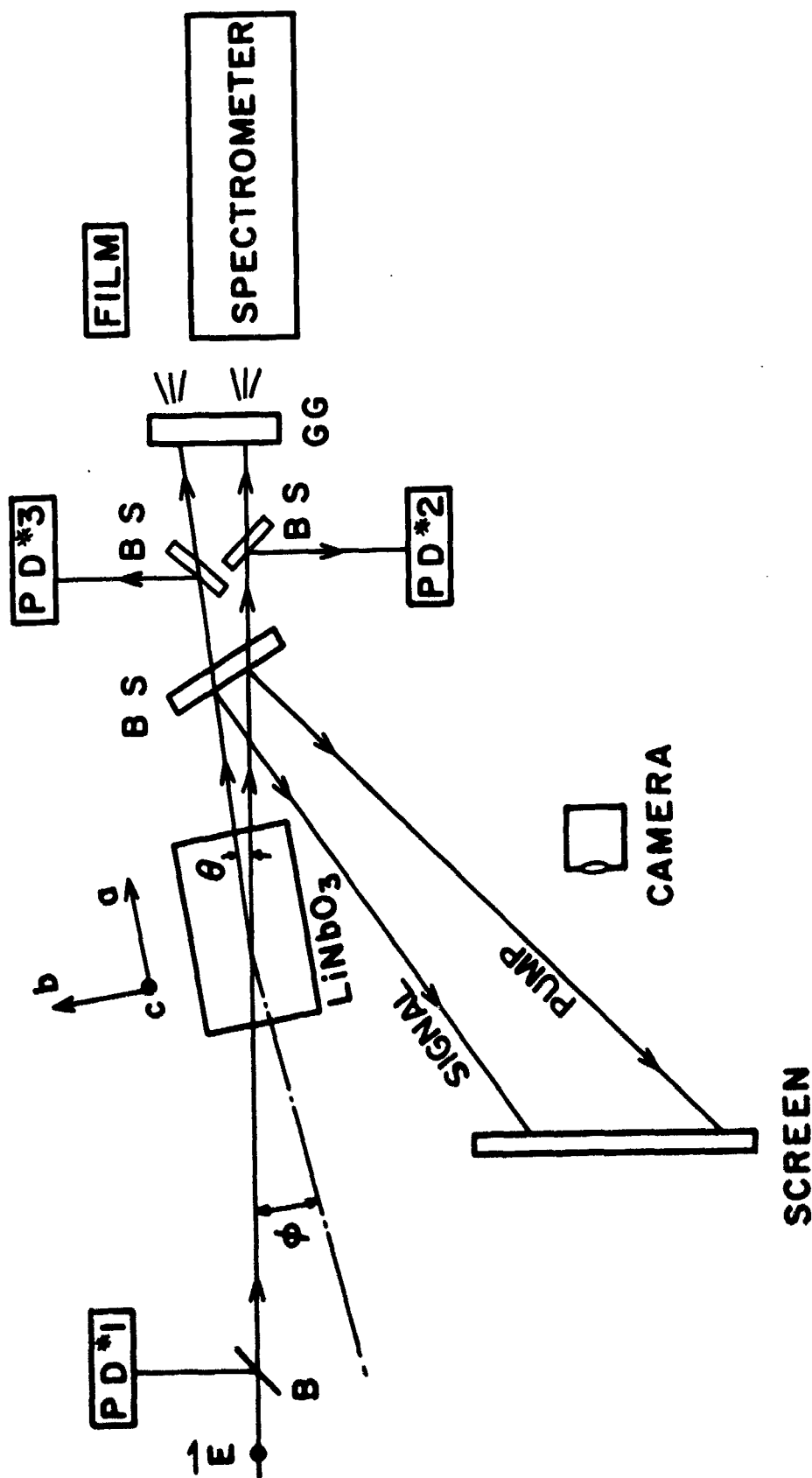
FIG. 5.5.--Schematic diagram of experimental apparatus for signal measurements in the stimulated scattering experiment. The angle between the pump beam and crystal surface normal is designated by ∅ ; the internal angle between pump and signal (phase-matching angle) is θ . Beam splitters are denoted by BB , and angle between pump and signal is θ . Beam splitters are denoted by BB , and GG is a ground glass screen (used to uniformly illuminate the slit of the spectrometer). Photodiodes to monitor input pump, output pump, and signal are designated as PD # 1, 2, and 3, respectively. The wave-lengths were measured photographically at the spectrometer output.
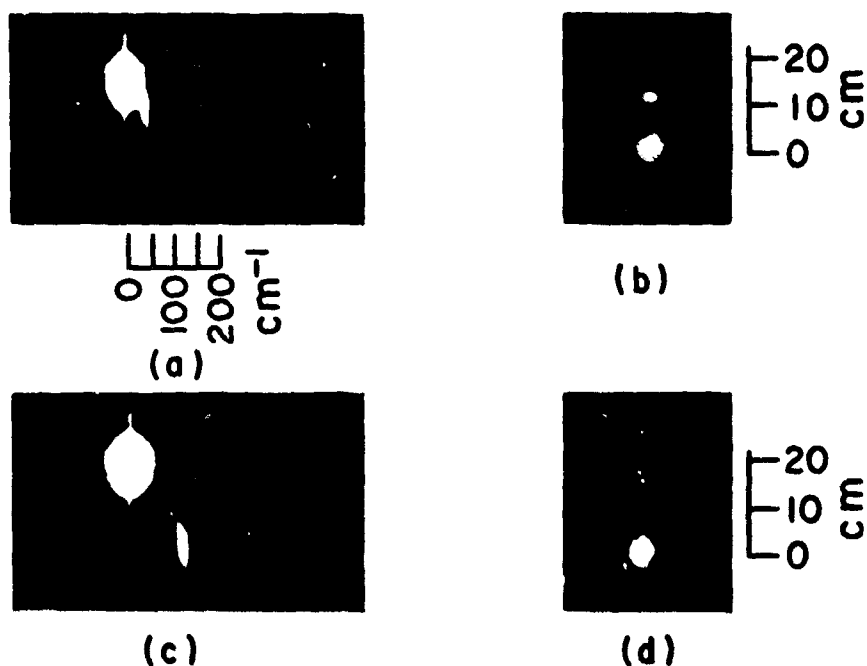
- 77 -

FIG. 5.6--Photographs of signal wavelength and spatial shifts. The wave-
lengths were photographed at the spectrometer output ($\underline{a}$ and $\underline{c}$);
the spatial positions of the beams were photographed at a dis-
tance of 5.6 meters from the crystal ($\underline{b}$ and $\underline{d}$). $\underline{a}$ and $\underline{b}$ are for
$\phi = 0^{\circ}$ (normal incidence); $\underline{c}$ and $\underline{d}$ are for $\phi = 2.3^{\circ}$. The
wavelength and spatial photographs are in good agreement with the
predictions from the dispersion curve (see Fig. 5.5). For these
pictures, the laser power was about 600 kW and was focused by
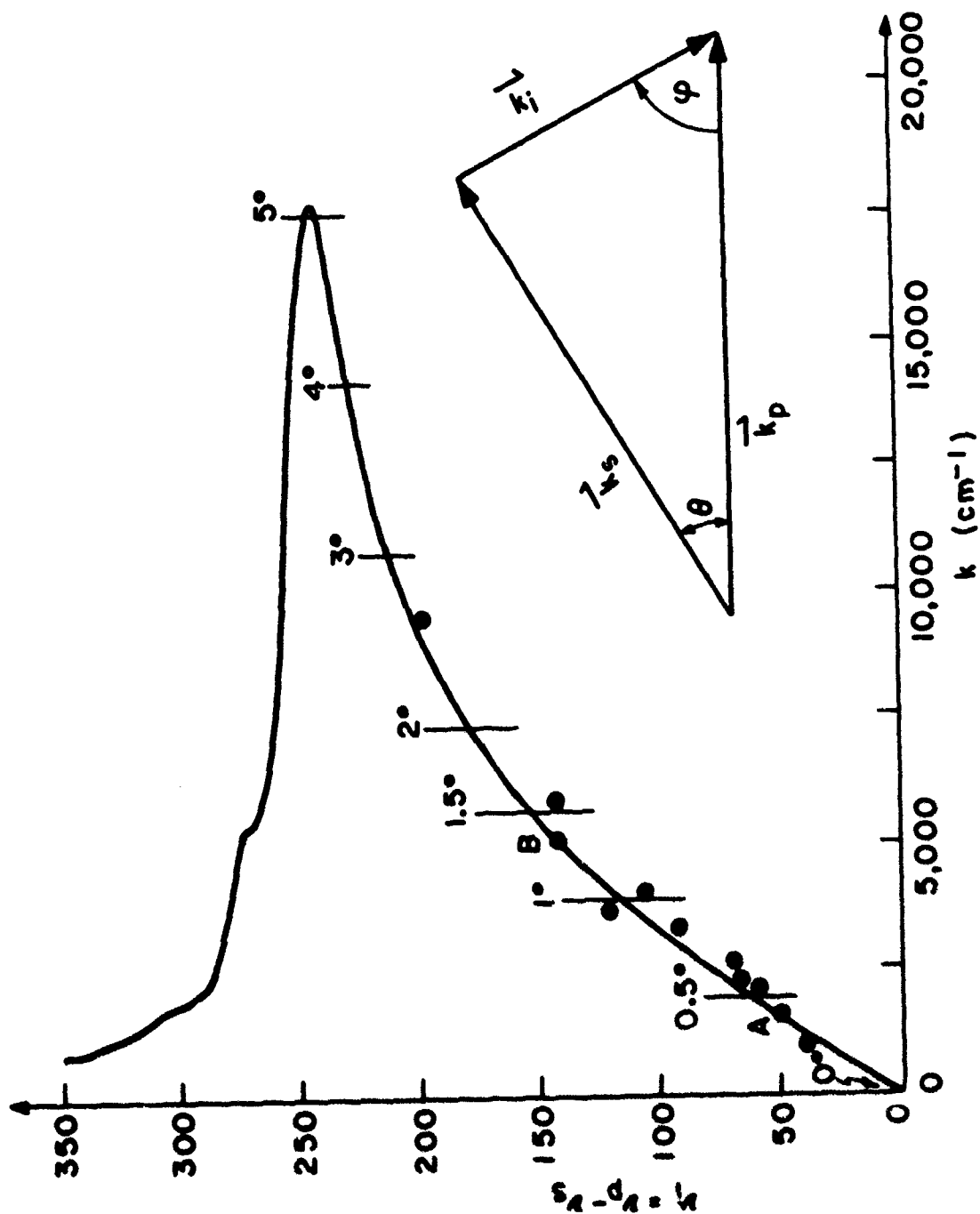a 50 cm lens.

Fig. 3.2. Dispersion curve for the A_1-symmetry modes of LiNbO$_3$ in the vicinity of the 243 cm^{-1} mode. The dots correspond to experimentally-observed points.

- 90 -

frequency shift in this case is 134 cm^{-1}, and again the spatial separation agrees with the observed shift. This point has been plotted as B on the dispersion curve. In both Figs. 5.6(b) and 5.6(d), the lower beam is the laser and the upper beam is the signal. Other measured points have also been plotted in Fig. 5.7.

Figure 5.8 shows the typical temporal response. Figure 5.8(a) shows the incident pump pulse, 5.8(b) the transmitted pump pulse, and 5.8(c) the corresponding signal pulse. For this particular case, the conversion was about 60%. The maximum conversion observed was approximately 70%.

In Fig. 5.9 the observed signal frequency shift, (and corresponding idler wavelength), is shown as a function of the angle of incidence of the laser beam relative to the normal to the crystal surface. The presence of the parallel crystal faces makes possible the tuning of the signal as the angle of incidence is varied. When the crystal was repolished so that there was an angle of 1.5° between opposite crystal surfaces, it was no longer possible to tune the signal by varying ϕ. In addition, it was necessary to increase the pump intensity in order to obtain a comparable signal intensity.

Good agreement with the tuning curve of Fig. 5.9 has been obtained by the "two-bounce" theory of Yarborough.[66] This theory assumes that the signal beam makes two forward passes through the pump beam inside the crystal. The second forward pass is due to a reflection from the output crystal surface and a re-reflection at the input surface. This explains the role of the parallel crystal faces in the tuning of the signal frequency. By using the appropriate crystal dimensions and pump beam spot size, a good fit is obtained to the measured tuning curve.

An estimate of the gain constant can be made from the experimental parameters.[66] The result is $g_s \approx 5$ cm^{-1}, assuming normal incidence of the pump and assuming that the "two-bounce" theory is valid.

Direct detection of the infrared idler was accomplished with the experimental set-up shown in Fig. 5.10. As shown, a 60° cut was made in the corner of the output end of the crystal to allow the idler wave to emerge approximately normal to the crystal surface, thus minimizing reflection loss at the crystal-air interface. To filter out stray optical signals, a strip of black polyethylene was placed in the light
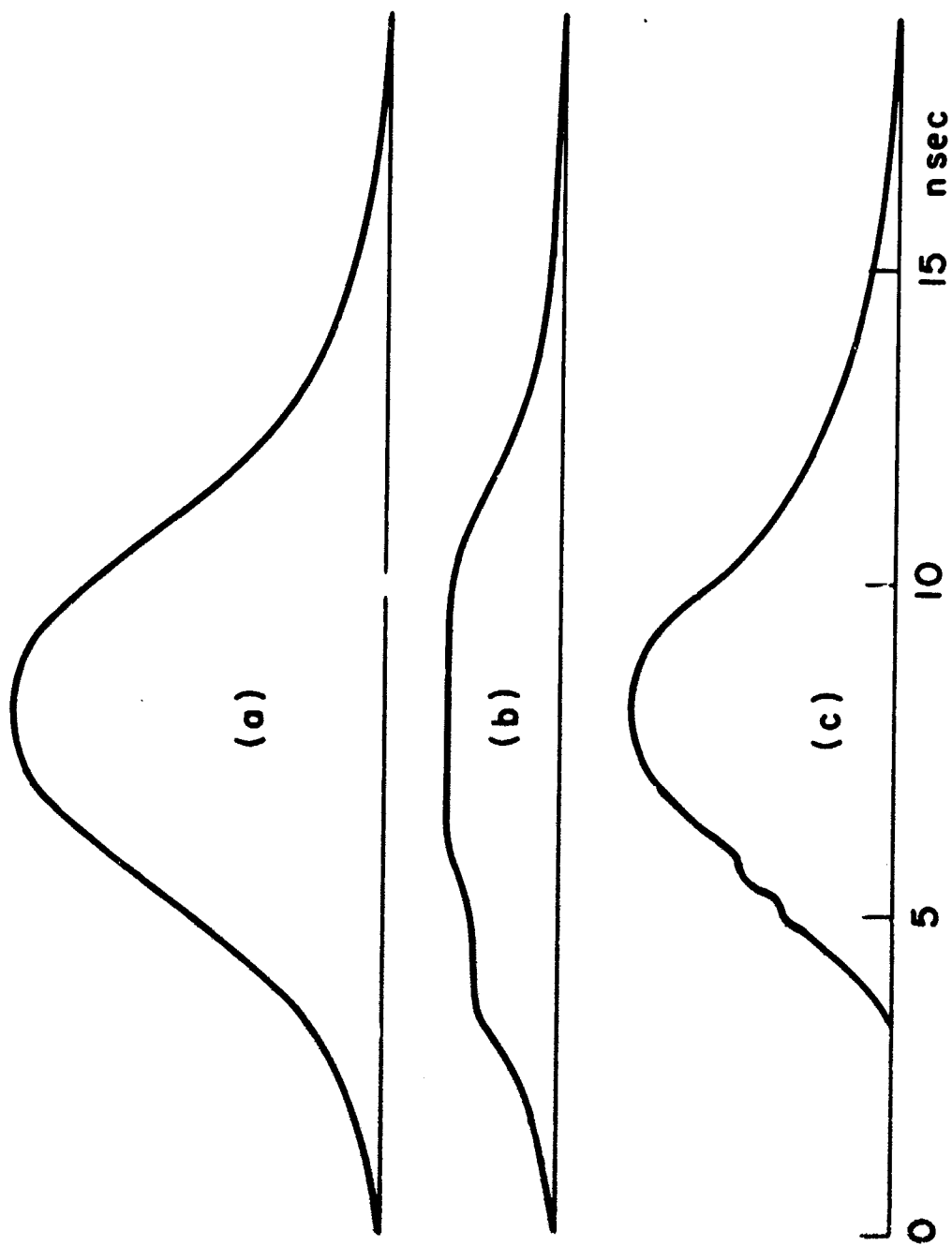
FIG. 2.4--Photodiode outputs for $\delta = 1°$. The laser power was about 1.3 MW and was focused with a 30-cm lens. (a) is the pump pulse at the crystal input; (b) is the pump pulse at the crystal output and (c) is the signal pulse. The conversion efficiency for this case was about 50%.
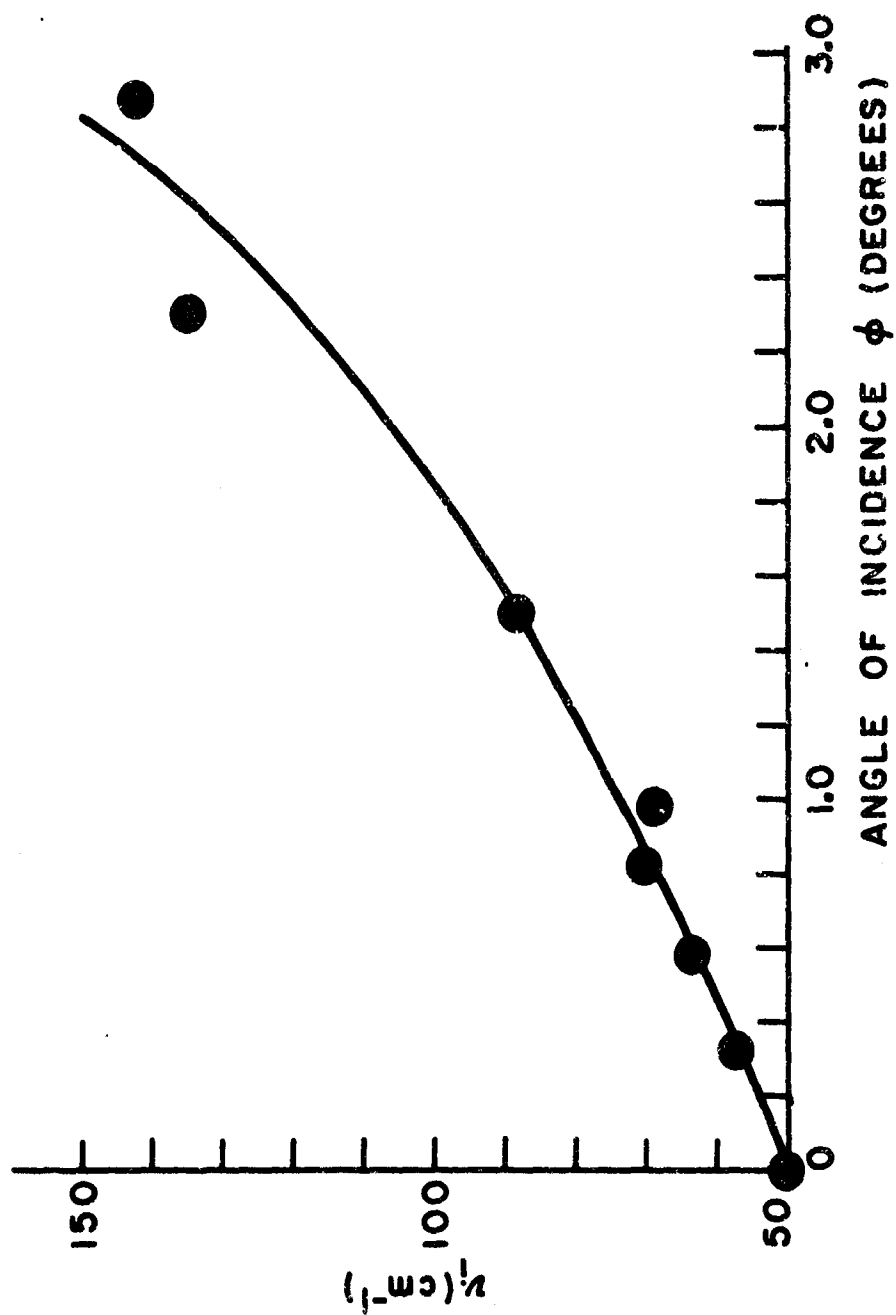
FIG. 5.9--Measured tuning curve as a function of angle of incidence, ϕ . The idler frequency is determined from energy conservation ($\nu_i = \nu_p - \nu_s$) ; the idler wavelength is given by $\lambda_i = 1/\nu_i$.

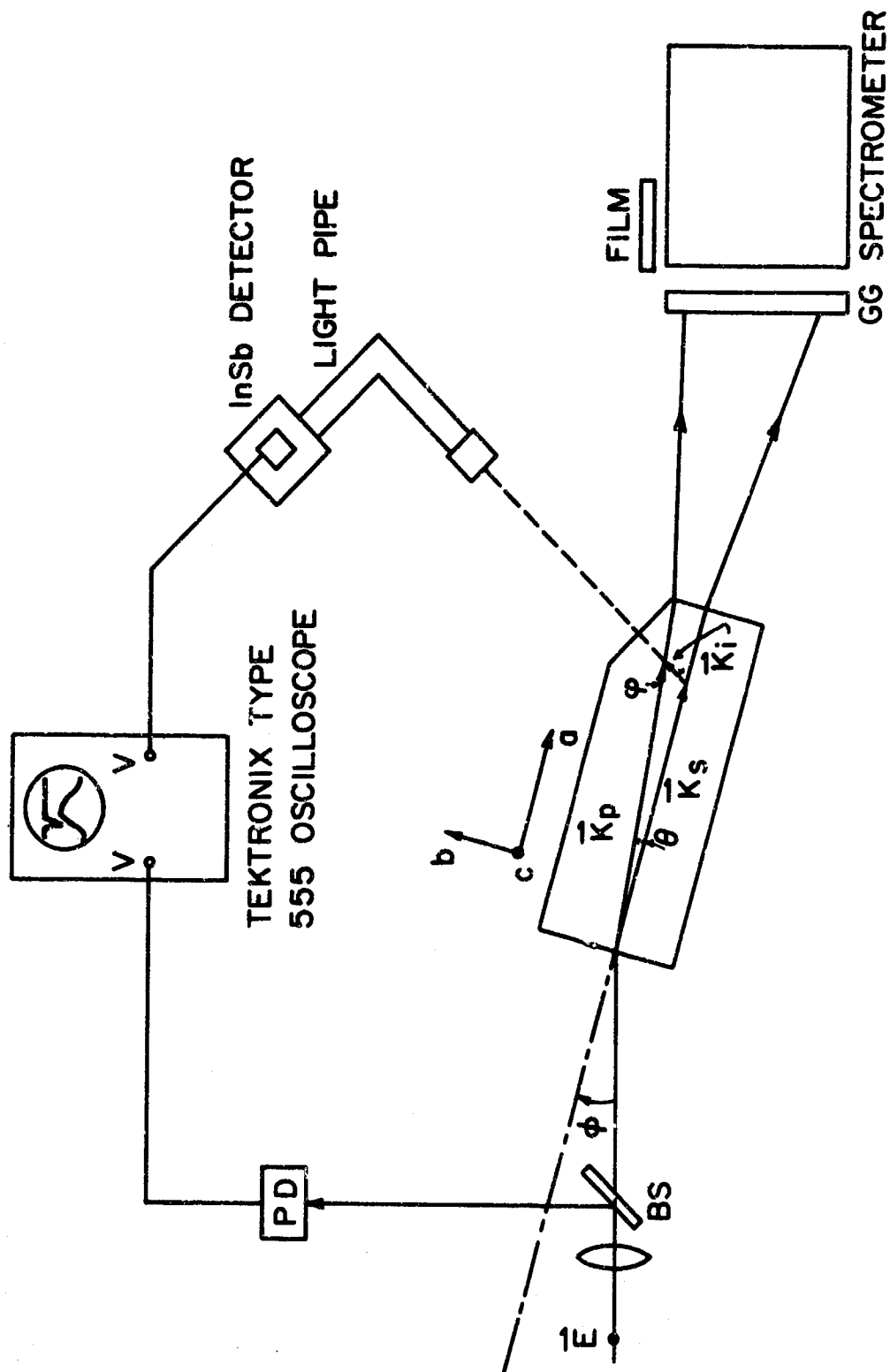FIG. 5.10—Experimental apparatus used to detect the idler power in the stimulated scattering experiment. The corner of the output face of the crystal was cut at 50° to allow the idler to emerge approximately normal to the crystal surface. The InSb detector was cooled to about 1.5°K in a helium dewar. BS is a beam splitter, PD a photodiode, and GG is a ground glass screen (used to illuminate uniformly the spectrometer slit).

pipe leading to the InSb detector, cooled to 1.5°K. The output of the detector was monitored on a Tektronix Type 555 oscilloscope. Figure 5.11 shows the idler pulse accompanying a pump-to-signal frequency shift of ~ 50 cm^{-1}, which corresponds to an idler wavelength of 200 μ. Based upon measurements of the pump and signal pulses using photodiodes [Figs. 5.8(a) -5.8(c)], the idler pulse duration is expected to be about 20 nsec. The idler pulse stretching may be attributed to detector and circuit response times.

Since the detector properties were only approximately known, it was difficult to determine a precise value for the peak power of the idler. The best estimate (based upon the detector responsivity) was that the observed idler power was approximately 5 W.

While the experimental results are important taken by themselves, their major significance for this work are in their comparison with the calculations presented in the previous chapters. Along this line, the following points are significant:

(1) The experimental results confirm that, for near-forward scattering, the gain for the 248 cm^{-1} mode is significantly higher than that of the 628 cm^{-1} mode, since tunable near-forward scattering from the 628 cm^{-1} mode was not observed.

(2) For the case of normal pump incidence, the experimentally inferred idler frequency is 50 cm^{-1}. Referring to Fig. 4.5 it is seen that the calculations show g_s to have a maximum at $\nu_i \approx 50$ cm^{-1}. For other than normal incidence, the frequency of the signal output is determined primarily by the feedback provided by the crystal surfaces.

(3) The calculated value of g_s for $\nu_i = 50$ cm^{-1} and a pump intensity of 5×10^8 W/cm^2 is about 24 cm^{-1} (see Fig. 4.5). If the transverse intensity distribution of the Gaussian pump beam had been included in the theory, the calculated gain would be reduced by about a factor of 2.[67] In addition, the effect of 50% pump depletion can be included in a very approximate manner by using a constant pump intensity of three-quarters of its input value. This would reduce the calculated gain by about 25%. Also, surface reflections should be taken into account. The net effect of including these factors is to reduce g_s to about 8 cm^{-1}, which is in reasonable agreement with the experimentally determined value of 5 cm^{-1}.
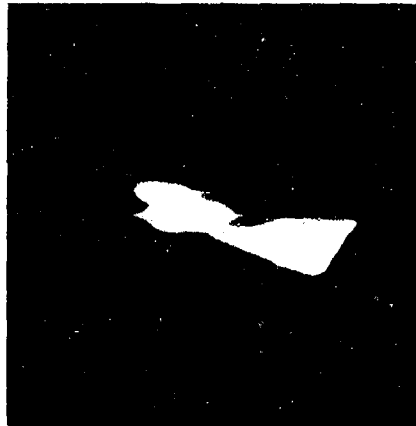
(a)
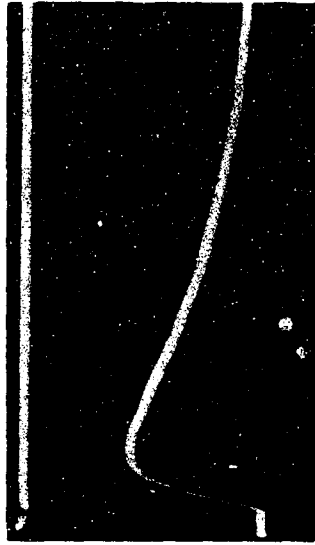
(b)

FIG. 5.11--Photographs of pump and signal wavelengths (a) and pump and idler pulse shapes (b). The pump-to-signal frequency shift is about 50 cm^{-1}; this indicates that the idler wavelength is about 200 μ. The sweep speed in (b) is 500 nsec/cm. The idler pulse is stretched out due to detector and detector circuit responses. The peak power of the idler beam is about 5 W (based upon the detector responsivity).

(4) The tuning curve agrees with that predicted by the intersection of the phase-matching lines with the theoretical dispersion curve. A more precise confirmation of this agreement is provided by the spontaneous scattering experiments described later.

(5) The temporal response pictures point out two significant facts. First, a complete theory clearly must include pump depletion. Second, the fact that the depletion of the pump occurs within the first few nanoseconds of the pulse indicates that the use of a steady state theory (for the remainder of the pulse) is reasonable.

(6) The detection of the idler is of itself significant theoretically, since this represented the first confirmation of its existence in near-forward scattering from vibrational modes. In addition, the measured idler power of ~5 W is consistent with the predicted power of about 60 W, (see Fig. 4.6), when reflections at the crystal-air-interface (~50%) and absorption in the crystal path length from the generating volume to the crystal surface are taken into account.

In summary, the experimental observations were found to be in good agreement with the calculations.

D.   SPONTANEOUS SCATTERING FROM THE 248 cm^{-1} MODE.

The final experiments which were performed involved measurements of the optical (signal) power which is generated in spontaneous scattering from the 248 cm^{-1} mode. The purpose of this effort was two-fold:

(1) Accurate measurements of the signal frequency as a function of scattering angle could be made to verify more precisely that the tuning does follow the theoretical dispersion curve.

(2) The variation in the magnitude of the scattered signal power as a function of idler frequency could be ascertained and compared to calculations.

The experimental set-up was the same as that described previously (see Fig. 5.4), with the following exceptions:

a)   The crystal was 3 cm long with polished front and back faces.

b)   Standard optical gratings were used in the Jarrel-Ash
monochromators, and two of the latter were used in tandem. This
reduced the monochromator bandwidth to ~5 Å and allowed for the
detection of weak signals at frequencies close to a strong pump.

(3) The detector was an RCA 7200 photomultiplier tube.

The results of these experiments are shown in Figs. 5.12,
5.13, and 5.14. In Fig. 5.12, measured points are plotted on the
dispersion curve described in Chapter IV. Within experimental error,
the measured points fall directly on the calculated curve.

The agreement with theory in this case is better than that
obtained in the stimulated experiment. This is simply because
the frequency measurements are more accurate in the spontaneous
experiments, due to the more precise measuring techniques which
were used.

The smallest measureable pump-to-signal frequency shift was
about 40 cm^{-1} ($\Delta\lambda \approx$ 10 Å), corresponding to θ = 0.22° . This was
limited by the presence of the strong pump signal.

The output of the detection system was plotted on a chart
recorder for each setting of the angle θ . These are shown in
Fig. 5.13, where all of the chart records have been drawn in one
sketch. In this case, meaningful data could be obtained only for
frequency shifts greater than about 110 cm^{-1} (25 Å).*

The magnitude of the scattered signal (taken from the chart
recordings) is plotted in Fig. 5.14, along with the calculated
curve (redrawn from Fig. 4.7). The data are normalized so that
the measured point A lies on the calculated curve. The agreement
between measurement and calculation is again quite good.

In summary, therefore, it can be said that the theory for
scattering from optical modes developed in Chapter III and the
experimental results described in Chapter V are in good agreement.
This indicates that the process of tunable signal and idler generation
in scattering from crystal optical modes is reasonably described by
the material in this report.

---

*With a recently reported detection technique,[68] it may be possible
to extend the data to within 25 cm^{-1} of a strong pump.
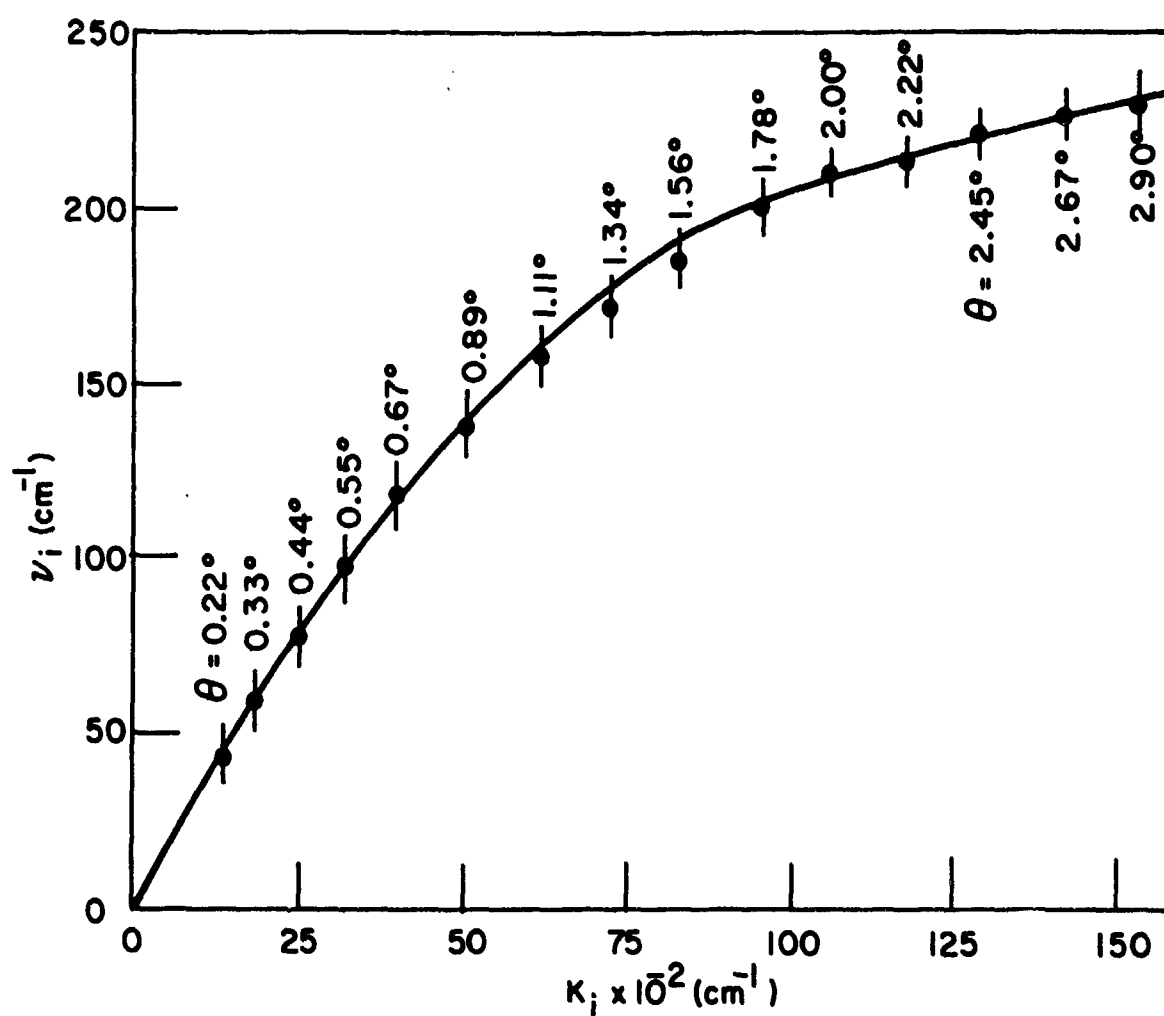
FIG. 5.12--Results of spontaneous scattering experiment, showing measured frequency shifts plotted on the dispersion curve. The solid curve is the calculated dispersion curve (see Fig. 4.2), the short lines are the phase-matching lines for an argon laser pump (λ = 4880 Å), and the measured points are indicated by dots.
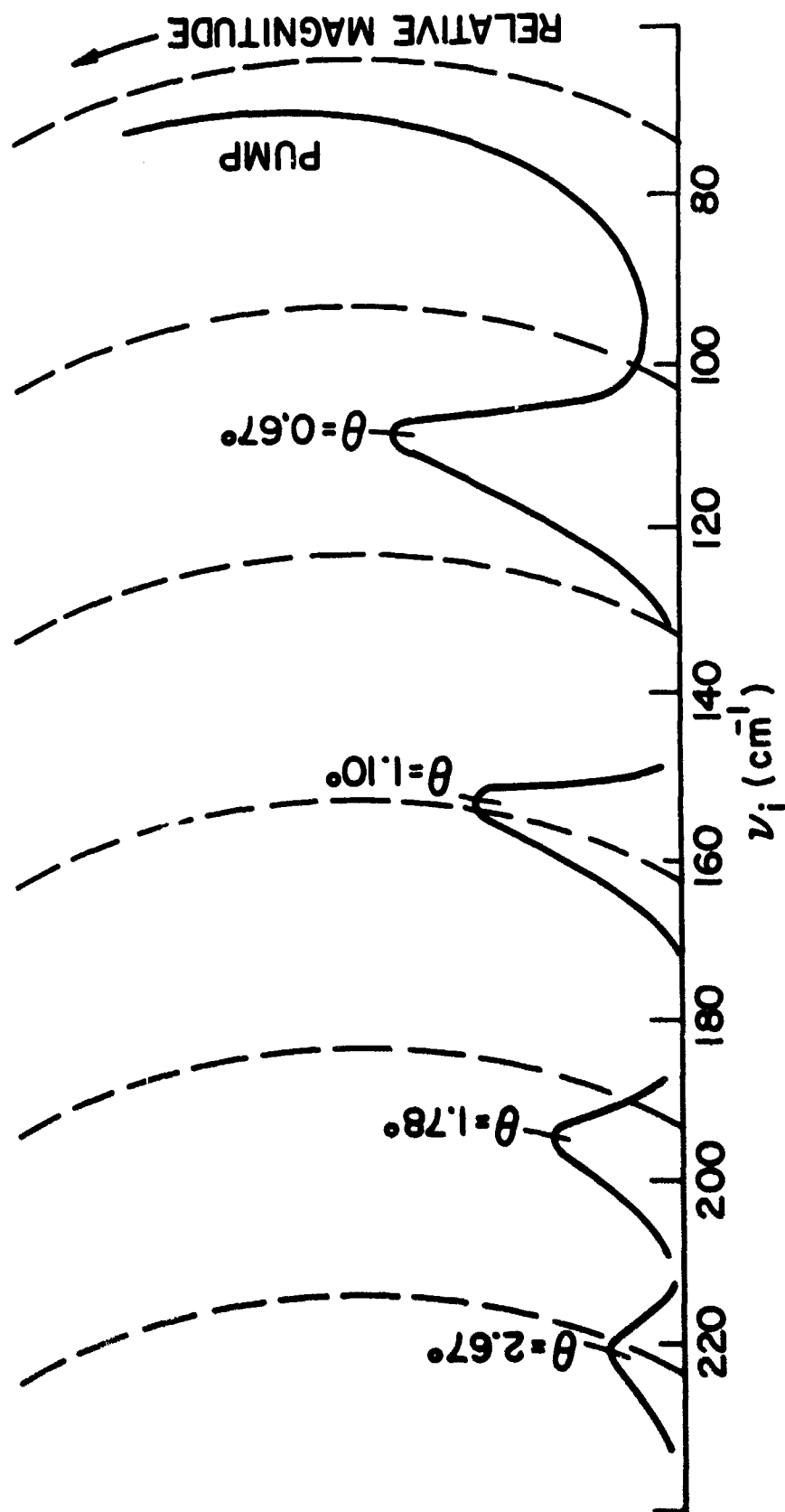
FIG. 5.13--Composite of recorder outputs for four values of θ, plotted vs idler frequency. The response due to the pump is shown at the far right; this response limited the range of the measurements to $\theta > 0.6°$ ($\nu_i \gtrsim 110$ cm). Due to the construction of the recorder (Esterline-Angus Model RD-49 A U), the lines of constant frequency are curved, as shown by the dashed lines.

FIG. 5.14-- Magnitude of scattered signal power as a function of idler
frequency. The dots are the measured points from Fig. 5.13; the curve is
a reproduction of a portion of the calculated curve of Fig. 4.7. The data
are normalized so that the measured point "A" lies on the calculated curve.

CHAPTER VI

CONCLUSIONS AND RECOMMENDATIONS

The contributions of this work are:

(1) Development of the theory for tunable, near-forward, stimulated and spontaneous light scattering and the application of the theory to the transverse modes in $LiNbO_3$.

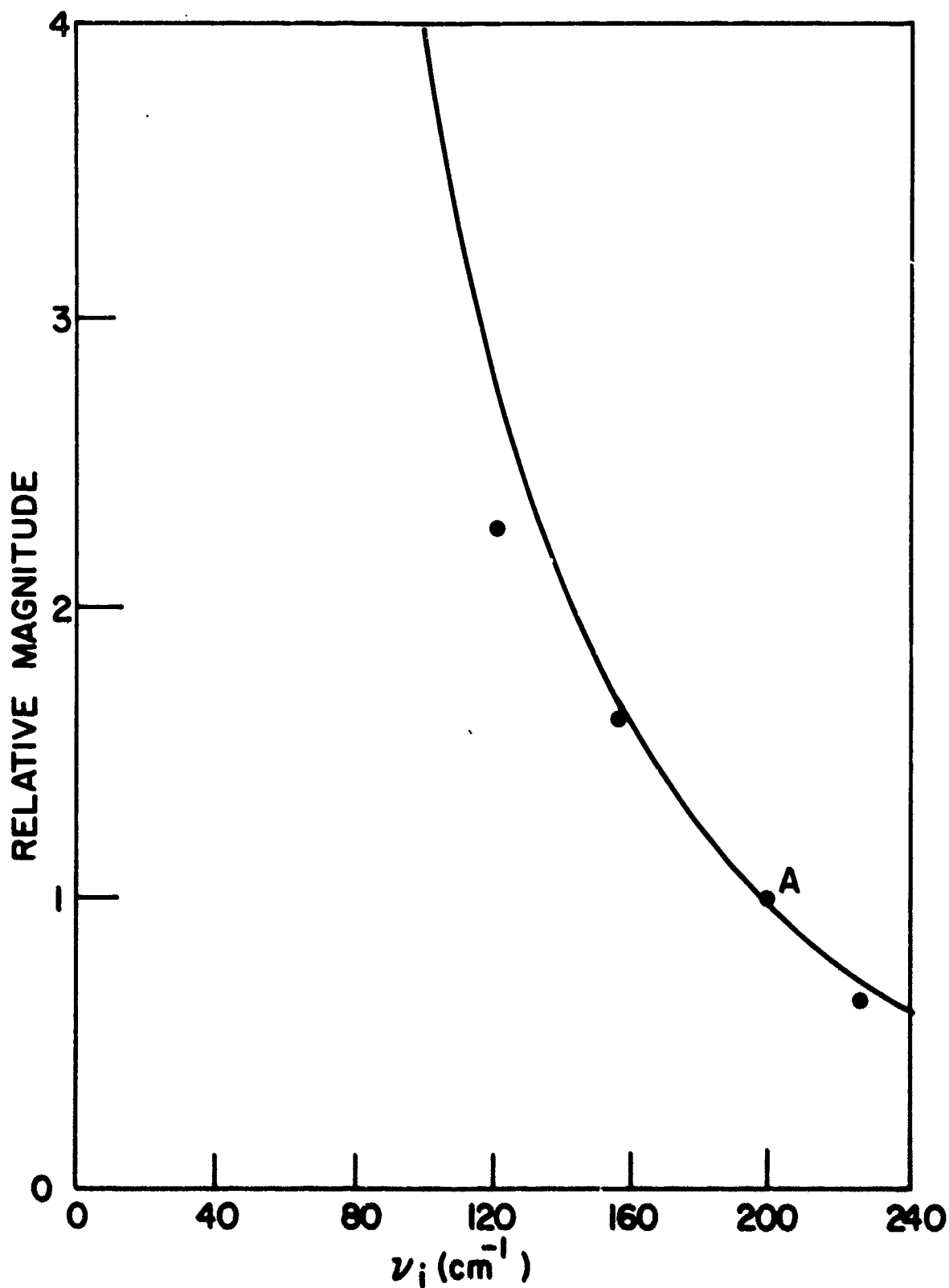(2) Observation of tunable, stimulated optical and infrared outputs in scattering from the 248 cm^{-1} mode in $LiNbO_3$, with experimental parameters in close agreement with predicted values.

(3) Construction of an experimental test set for performing spontaneous measurements, consisting of an argon laser and a phase-sensitive detection apparatus.

(4) Measurements of spontaneous scattering from the 248 cm^{-1} mode, accurately confirming both the predicted tuning characteristic in accordance with the infrared dispersion curve, and the calculation of the frequency dependence of the magnitude of the scattered signal.

With reference to further extensions of this work, the following suggestions are offered. The inclusion of the effects of pump depletion and transverse intensity variations of the beams would improve the validity of the calculations. On the experimental side, the characteristics of the idler radiation generated in stimulated scattering from the 248 cm^{-1} mode should be examined in more detail. In particular, better measurements of the power output should be made, along with studies of the linewidth of the radiation. In addition, the evaluation of other crystals will, without doubt, continued to play a central role in the field of nonlinear optics.

APPENDIX A

THE ENERGY DENSITY FUNCTION

In the energy density approach, the existence of a phenomenological energy density function (U) is assumed, and a method for directly deriving the driving terms (polarization and forces) is given. In particular, U is assumed to be a function of the lattice displacement coordinates Q and the electric fields E ; that is,

$$U = U(Q,E)   ,$$

and the function is defined such that the polarization at frequency ω_i , $P(\omega_i)$, and the force at frequency ω_i , $F(\omega_i)$, are given by:

$$P(\omega_i) = - \frac{\partial U}{\partial E(\omega_i)^*}$$

$$F(\omega_i) = - \frac{1}{N} \frac{\partial U}{\partial Q(\omega_i)^*}   , \tag{A.1}$$

where N is the number of unit cells per unit volume. The dimensions of U are energy per unit volume.

To illustrate the approach, we examine the linear problem, where only a vibration and an electric field at ω_i are considered. Since the polarization and the force will be linear in Q and E , we begin with a second order U [written as $U^{(2)}$], which is quadratic in Q and E . Using a slightly modified form of Kleinman's notation,[25] we get:

$$U^{(2)}(Q,E) = -\frac{1}{2} [Nb_{11}Q^2 + 2Nb_{12}QE + b_{22}E^2]   .$$

Writing Q and E as

$$Q = Q(\omega_i) + Q(\omega_i)^* \quad , \quad E = E(\omega_i) + E(\omega_i)^* \quad ,$$

and retaining only dc terms* in $U^{(2)}$, we get

$$U^{(2)} = - [Nb_{11}QQ^* + b_{22}EE^* + Nb_{12}(Q^*E+E^*Q)] \quad ;$$

and using (A.1),

$$P(\omega_i) = Nb_{12}Q + b_{22}E$$

$$F(\omega_i) = b_{11}Q + b_{12}E \quad .$$

Note that this yields the expected result. The polarization is given by two terms—one due to the vibration and the other being the frequency independent term. Similarly, the force is given by a term proportional to Q (the restoring force) and a term proportional to the electric field E .

To examine the first-order nonlinearity, we consider $U^{(3)}$, which is cubic in Q and E . This is given by

$$U^3(Q,E) = -\frac{1}{3} [f_1 Q^3 + 3f_2 Q^2 E + 3f_3 QE^2 + f_4 E^3] \quad . \quad (A.2)$$

For the case we are considering in the text, there are electric fields at ω_p , ω_s and ω_i , and a lattice displacement at ω_i . Therefore, we write

$$Q(lattice) = Q(\omega_i) + Q(\omega_i)^*, \quad E(pump) = E(\omega_p) + E(\omega_p)^*$$

$$E(idler) = E(\omega_i) + E(\omega_i)^*, \quad E(signal) = E(\omega_s)+E(\omega_s)^* \quad .$$

---

*By dc terms, it is meant terms which exhibit no frequency dependence. It can be shown[10] that only these terms in U lead to driving terms which can produce significant interaction.

Examining (A.2), we note that the dc terms can arise only from the QE^2 and the E^3 terms. Therefore, $U^{(3)}$ reduces to

$$U^{(3)} = - f_3[Q(\omega_i)^*E(\omega_s)^*E(\omega_p)+ c.c.]$$

$$- \frac{f_4}{3}[E(\omega_i)^*E(\omega_s)^*E(\omega_p)+ c.c.] \quad .$$

Defining $f_3 \equiv d_E$ and $f_4/3 \equiv NdQ$, we arrive at

$$U^{(3)} = - [d_E E(\omega_p)E(\omega_s)^*E(\omega_i)^*+ Nd_Q E(\omega_p)E(\omega_s)^*Q(\omega_i)^*] + c.c. \quad .$$

$$(A.3)$$

Equation (3.5) is an extension of (A.3) to a multimode material.

APPENDIX B

CALCULATION OF PHASE MATCHED GAIN IN "HIGH LOSS"
REGION FOR MULTI-MODE MEDIA

Setting $g_i = 0$ and $k_s^2 = (\omega_s^2/c^2)\,\epsilon_{\infty_s}$ (i.e., phase matching for the signal), we find that Eq. (3.14) becomes

$$ik_s g_s = \frac{\dfrac{\omega_i^2 \omega_s^2}{c^4}\,|A_p|^2\left[d_E' + \sum_j \dfrac{\Omega_{p_j}^2 d_{Q_j}'}{D_j(\omega_i)^*}\right]^2}{\dfrac{\omega_i^2}{c^2}\,\epsilon_i^* - k_i^2} - \frac{\omega_s^2}{c^2}\,|A_p|^2 \sum_j \frac{\Omega_{p_j}^2 d_{Q_j}'^2}{D_j(\omega_i)^*} \quad .$$

$$(B.1)$$

In the region where ω_i is outside the linewidth of each of the j modes,

$$D_j(\omega_i)^* = \omega_{0_j}^2 - \omega_i^2 + i\omega_i\Gamma_i \approx \omega_{0_j}^2 - \omega_i^2 \quad .$$

Also, the imaginary part of the second term on the RHS of (B.1) is small and can be neglected. Thus, we must consider only the imaginary part of the first term. This, in turn, is due to the imaginary part of its denominator. Expanding the denominator gives

$$\frac{\omega_i^2}{c^2}\,\epsilon_i^* - k_i^2 = \frac{\omega_i^2}{c^2}\left[\epsilon_{\infty} + \sum_j \frac{\Omega_{p_j}^2}{D_j(\omega_i)^*}\right] - k_i^2 =$$

$$\frac{\omega_i^2}{c^2}\left[\epsilon_{\infty} + \sum_j \frac{\Omega_{p_j}^2}{(\omega_{0_j}^2 - \omega_i^2)}\left(1 - \frac{i\omega_i\Gamma_j}{\omega_{0_j}^2 - \omega_i^2}\right)\right] - k_i^2 = -\frac{i\omega_i^3}{c^2}\sum_j \frac{\Omega_{p_j}^2 \Gamma_j}{(\omega_{0_j}^2 - \omega_i^2)^2} \quad ,$$

$$(B.2)$$

where the condition that (ω_i, k_i) lie on the undamped dispersion curve, that is,

$$k_i^2 = \frac{\omega_i^2}{c^2} \left(\epsilon_\infty + \sum_j \frac{\Omega_{P_j}^2}{\omega_{0_j}^2 - \omega_i^2} \right)$$

has been imposed.

Substitution of (B.2) into (B.1) yields the final result:

$$g_s = \frac{\omega_s |A_p|^2}{c\omega_i \eta_s} \left[\frac{1}{\sum_j \dfrac{\Gamma_i \Omega_{P_j}^2}{(\omega_{0_j}^2 - \omega_i^2)^2}} \right] \left(d_E' + \sum_j \frac{\Omega_{P_j}^2 \, d_{Q_j}'}{\omega_{0_j}^2 \, \omega_i^2} \right)^2 \qquad \text{(B.3)}$$

$$\omega_{0_j} + \Gamma_j < \omega_i < \omega_{0_j} - \Gamma_j$$

APPENDIX C

SOLUTION OF BOUNDARY VALUE PROBLEM TO
DETERMINE DIRECTION OF $\vec{\gamma}$

The direction of $\vec{\gamma}$ can be determined from an analysis of the boundary conditions which must be satisfied at the interface between the linear (air) and nonlinear media. The approach, which was suggested by Bloembergen and Pershan,[41] makes use of the fact that a necessary and sufficient condition for the requirement that the tangential components of the electric fields be continuous across a boundary is that the components of the momentum wave vector $(\vec{k})$ parallel to the boundary remain conserved.

This is now applied to the geometry of Fig. C.1. The boundary is the $y = 0$ plane, and the pump wave vector external to the nonlinear medium $(\vec{k}_p^e)$ makes an angle ϕ with the normal to the boundary. The phase-matching triangle inside the material is also shown.

For the purposes of this analysis, the space-dependent part of plane wave expressions for the signal and idler will be written

$$e^{i\vec{K}\cdot\vec{r}} = e^{i(\vec{K}' - i\vec{K}'')\cdot\vec{r}} \qquad ,$$
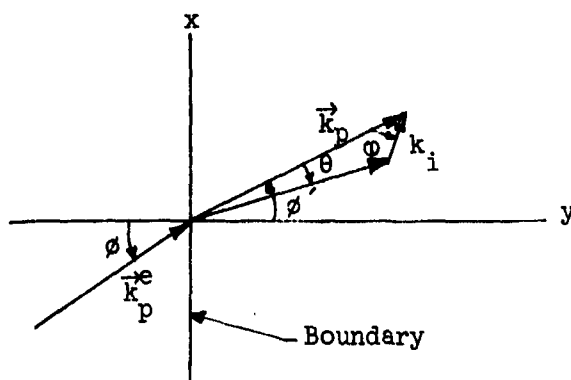

FIG. C.1--Sketch of the geometry for the boundary value problem.

where $\vec{k}'' = \vec{\gamma}$, used in the text. Continuity of the x-component wave vector leads to

$$\vec{k}_p^e \cdot \hat{x} \;=\; \vec{k}_p \cdot \hat{x} \;=\; \vec{k}_s \cdot \hat{x} + \vec{k}_i \cdot \hat{x} \qquad , \qquad (C.1)$$

where $\hat{x}$ is a unit vector in the x-direction. Since $\vec{k}_p^e$ is real, (C.1) yields

$$\vec{k}_p' \cdot \hat{x} \;=\; \vec{k}_s' \cdot \hat{x} + \vec{k}_i' \cdot \hat{x}$$

$$\vec{k}_s'' \cdot \hat{x} \;=\; -\vec{k}_i'' \cdot \hat{x} \qquad .$$

But, it has been shown [Eq.(3.11b)] that

$$\vec{k}_s'' \;=\; \vec{k}_i \; (=\vec{\gamma}) \qquad ;$$

$$\therefore \qquad \vec{k}_s'' \cdot \hat{x} \;=\; \vec{k}_i'' \cdot \hat{x} \;=\; 0 \quad ,$$

or $\vec{\gamma}$ lies along the normal to the boundary (the y axis in the geometry of Fig. C.1).

Recalling the definitions of g_i and g_s in Eq. (3.13), we obtain immediately the desired relationship:

$$g_i \;=\; g_s \; \frac{\cos\,(\varphi + \phi')}{\cos\,(\phi' - \theta)} \qquad . \qquad (C.2)$$

For near forward scattering and for near-normal incidence of the pump, Eq. (C.2) reduces to:

$$\boxed{g_i \;=\; g_s \, \cos\,\varphi} \qquad . \qquad (C.3)$$

APPENDIX D

SOLUTION FOR g_s IN NONCOLLINEAR LOW LOSS REGION

Setting $k_s^2 = (\omega_s^2/c^2)\,\epsilon_{\infty_s}$ in the secular equation (3.14) and substitution of $g_s = g_i/\cos\varphi$ yields:

$$\left(-k_i^2 - ik_i g_i + \frac{\omega_i^2}{c^2}\epsilon_i^*\right)\left[\frac{\omega_s^2}{c^2}(|A_p|^2)' \sum_j \frac{\Omega_{p_j}^2 dQ_j'^2}{D_j(\omega_i)^*} + ik_s g_i\right] =$$

$$\frac{\omega_i^2 \omega_s^2}{c^4}(|A_p|^2)'\left(d_E' + \sum_j \frac{\Omega_{p_j}^2 dQ_j'}{D_j(\omega_i)^*}\right)^2 \qquad , \qquad (D.1)$$

where

$$(|A_p|^2)' = |A_p|^2 \cos\varphi \quad .$$

Thus, g_s has been eliminated from the equation and proceeding as in Appendix B of HG gives:

$$g_i = \frac{\alpha_i}{2}\left[\left(1 + \frac{16\,\alpha_p'^2}{\alpha_i}\right)^{1/2} - 1\right] \qquad , \qquad (D.2)$$

where

$$\alpha_p'^2 = \alpha_p^2 \cos\varphi \qquad ;$$

and therefore

$$g_s = \frac{g_i}{\cos\varphi} = \frac{\alpha_i}{2\cos\varphi}\left[\left(1 + \frac{16\,\alpha_p'^2}{\alpha_i^2}\right)^{1/2} - 1\right] \qquad .$$

$$(D.3)$$

APPENDIX E

SCATTERED IDLER POWER

The idler power scattered into a small solid angle and frequency range is given by:

$$P_i\big)_{\Delta\Omega_i',\Omega\omega_i} = \left(\frac{P_i}{P_p\, d\Omega_i'\, d\omega_i}\right) P_p \Delta\Omega'\, \Delta\omega_i \qquad , \qquad (E.1)$$

where the prime indicates that the solid angle is measured outside the crystal (after refraction at the crystal surface).

For an aperture of height H located at distance r from the end face of the crystal, the accepted solid angle $\Delta\Omega_i'$ is (see Fig. E.1):

$$\Delta\Omega_i' \approx \frac{A}{r^2} \approx \frac{Hr\Delta\varphi'}{r^2} = \frac{H\Delta\varphi'}{r} \qquad ,$$

and

$$\therefore \quad P_i\big)_{\Delta\Omega_i',\Delta\omega_i} = \left(\frac{P_i}{P_p\, d\Omega_i'\, d\omega_i}\right) P_p \frac{H\Delta\varphi'}{r} \Delta\omega_i \quad . \qquad (E.2)$$

The expressions derived in the text, however, give the scattered power per unit solid angle, with the solid angle measured about the __signal__ propagation direction. To convert this to the form required for Eq. (E.1), we write:

$$\frac{P_i}{P_p\, d\Omega_i'\, d\omega_i} = \left(\frac{P_i}{P_p\, d\Omega\, d\omega}\right)\left[\frac{1}{\left(\dfrac{d\Omega_i'}{d\Omega}\right)}\right]\left[\frac{1}{\left(\dfrac{d\omega_i}{d\omega}\right)}\right] \quad . \qquad (E.3)$$

But

$$\left|\frac{d\omega_i}{d\omega}\right| = 1 \quad , \quad \frac{d\Omega_i'}{d\Omega} = \eta_i \frac{d\Omega_i}{d\Omega} = \eta_i \frac{d\varphi}{d\theta}$$
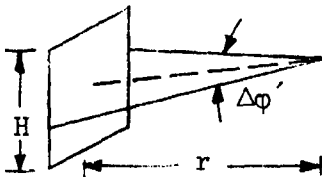
FIG. E.1--Sketch of geometry for the solid angle calculation.

Therefore,

$$P_i\Big)_{\Delta\Omega_i',\Omega\omega_i} = \left(\dfrac{P_i}{P_p\,d\Omega d\omega}\right)\ \dfrac{P_p\Delta\omega_i}{\dfrac{d\varphi}{d\theta}}\left(\dfrac{H}{r}\right)\left(\dfrac{\Delta\varphi'}{\eta_i}\right) \qquad , \qquad (E.4)$$

which is the desired result.

It should be recalled that specifying the solid angle $\Delta\Omega_i$ specifies the frequency range $\Delta\omega_i$ through the intersections of the phase-matching lines with the dispersion curve.

REFERENCES

1. C. V. Raman and R. S. Krishnan, Nature <u>121</u>, 501 (1928).

2. E. J. Woodbury and W. K. Ng, Proc. IRE (Corres.) <u>50</u>, 2367 (1962).

3. M. Geller, D. P. Bortfeld, and W. R. Sooy, Appl. Phys. Letters <u>3</u>, 36 (1963).

4. B. P. Stoicheff, Phys. Letters <u>7</u>, 186 (1963).

5. G. Eckhardt, D. P. Bortfeld, and M. Geller, Appl. Phys. Letters <u>3</u>, 136 (1963).

6. R. W. Minck, R. W. Terhune, and W. G. Rado, Appl. Phys. Letters <u>3</u>, 181 (1963).

7. R. W. Hellwarth, Phys. Rev. <u>130</u>, 1850 (1963).

8. R. W. Hellwarth, Appl. Optics <u>2</u>, 847 (1963).

9. H. J. Zeiger and P. E. Tannenwald, <u>Quantum Electronics, Proceedings of the Third International Congress</u>, eds., P. Grivet and N. Bloembergen, (Columbia University Press, New York, 1964), Vol. 2, 1588.

10. E. Garmire, F. Pandarese, and C. H. Townes, Phys. Rev. Letters <u>11</u>, 160 (1963).

11. C. Kittel, <u>Quantum Theory of Solids</u> (John Wiley and Sons, Inc., New York, 1963), pp. 37 ff.

12. K. Huang, Proc. Roy. Soc. (London) <u>A208</u>, 352 (1951).

13. M. Born and K. Huang, <u>Dynamical Theory of Crystal Lattices</u> (Clarendon Press, Oxford, 1954), pp 82 ff.

14. J. J. Hopfeld, Phys. Rev. <u>112</u>, 1555 (1958).

15. R. Loudon, Proc. Phys. Soc. <u>82</u>, 393 (1963).

16. R. H. Pantell and H. E. Puthoff, Proposal to the Office of Naval Research for Continuation of Microwave Research under Contract Nonr 225(48), NR 373-361 for period 1 January 1965 - 31 December 1965, Microwave Laboratory Proposal, Stanford University (1964).

17. H. E. Puthoff, R. H. Pantell, B. G. Huth, and M. A. Chacon, J. Appl. Phys. <u>39</u>, 2144 (1968).

18. P. N. Butcher, R. Loudon, and T. P. McLean, Proc. Phys. Soc. (London) 85, 565 (1965).

19. Y. R. Shen, Phys. Rev. 138, A1741 (1965).

20. F. DeMartini, J. Appl. Phys. 37, 2 (1966).

21. C. H. Henry and C. G. B. Garret, Phys. Rev. 171, 1058 (1968).

22. S. K. Kurtz and J. A. Giordmaine, Phys. Rev. Letters 22, 192 (1969).

23. J. Gelbwachs, R. H. Pantell, H. E. Puthoff, and J. M. Yarborough, Appl. Phys. Letters 14, 258 (1969).

24. J. M. Yarborough, S. S. Sussman, H. E. Puthoff, R. H. Pantell, and B. C. Johnson, Appl. Phys. Letters 15, 102 (1969).

25. D. A. Kleinman, Phys. Rev. 126, 1977 (1962).

26. M. Bloembergen, Nonlinear Optics (W. A. Benjamin, Inc., New York, 1968), Sec. 1.3.

27. J. D. Jackson, Classical Electrodynamics (John Wiley and Sons, Inc., New York, 1962).

28. L. Brillouin, Wave Propagation in Periodic Structures (McGraw-Hill Book Co., Inc, 1946).

29. C. Kittel, Introduction to Solid State Physics (Third Edition) (John Wiley and Sons, Inc., New York, 1967), pp. 150 ff.

30. A. S. Barker, Jr., Phys. Rev. 136, A1290 (1964).

31. A. S. Barker, Jr., and R. Loudon, Phys. Rev. 158, 433 (1967).

32. C. H. Henry and J. J. Hopfeld, Phys. Rev. Letters 15, 964 (1965).

33. This description is condensed from that given in R. H. Pantell and H. E. Puthoff, Fundamentals of Quantum Electronics (John Wiley and Sons, Inc., New York, 1969), pp. 229 ff.

34. H. E. Puthoff, Microwave Laboratory Report No. 1547, Stanford University (1967).

35. P. S. Pershan, Progress in Optics, E. Wolf, editor (North-Holland Publishing Co., Amsterdam

36. Reference 26, Section 1.2.

37. W. L. Faust and C. H. Henry, Phys. Rev. Letters 17, 1265 (1966).

38. Reference 34, Equations (4.10) and (4.11).

39. G. D. Boyd, W. D. Johnston, Jr., and I. P. Kaminow, IEEE J. Quant. Electr. QE-5, 203 (1969), for example.

- 103 -

40. Reference 21, Appendix B.

41. N. Bloembergen and P. S. Pershan, Phys. Rev. $\underline{128}$, 606 (1962).

42. R. H. Pantell and H. E. Puthoff, Fundamentals of Quantum Electronics (John Wiley and Sons, Inc., New York, 1969), pp. 239 ff. Note the difference in subscript notation between this reference and the present work.

43. Reference 42, p. 237.

44. Reference 42, p. 62.

45. Reference 42, pp. 179 ff. The factor of 2 , which was inserted to account for the two possible polarizations for the modes, has been omitted since scattered lines are highly polarized.

46. I. P. Kaminow and W. D. Johnston, Jr., Phys. Rev. $\underline{160}$, 519 (1967).

47. Reference 42, p. 65

48. W. D. Johnston, Jr. and I. P. Kaminow, Phys. Rev. $\underline{168}$, 1045 (1968).

49. This approach was first used in reference 46.

50. P. N. Butcher, Nonlinear Optical Phenomena, Bulletin 200, Engineering Experiment Station, Ohio State University, Columbus, Ohio (1965), Chapter 14.

51. W. L. Faust, C. H. Henry, and R. H. Eick, Phys. Re. $\underline{173}$, 781 (1968).

52. G. D. Boyd, R. C. Miller, K. Nassau, W. L. Bond and A. Savage, Appl. Phys. Letters $\underline{5}$, 234 (1964).

53. J. D. Axe and D. F. O'Kane, Appl. Phys. Letters $\underline{9}$, 58 (1966).

54. G. Hertzberg, Infrared and Raman Spectra of Polyatomic Molecules (D. Van Nostrand Co., Inc., New York, 1945), Vol. 2.

55. M. V. Hobden and J. Warner, Phys. Letters $\underline{22}$, 243 (1966).

56. J. F. Nye, Physical Properties of Crystals (Clarendon Press, Oxford, 1957), p. 113.

57. J. E. Bjorkholm, IEEE J. Quant. Electr. $\underline{QE-4}$, 970 (1968).

58. E. H. Turner, Appl. Phys. Letters $\underline{8}$, 303 (1966).

59. S. P. S. Porto, B. Tell, and T. C. Damen, Phys. Rev. Letters $\underline{16}$, 450 (1966).

60. J. P. Goldsborough, E. B. Hodges, and W. E. Bell, Appl. Phys. Letters $\underline{8}$, 137 (1966).

61. R. D. Moore, Electronics $\underline{35}$, 23, 40 (1962).

62. R. D. Moore and O. C. Chaykowdky, Technical Bulletin 109, Princeton Applied Research Corp., Princeton, New Jersey.

63. R. Brower, Electronics $\underline{41}$, 14, 80 (1968).

64. Solid State Research Report, February 1966, M. I. T. Lincoln Laboratory, Lexington, Mass., pp. 14-16.

65. T. M. Quist, Proc. IEEE $\underline{56}$, 1212 (1968).

66. J. M. Yaroborough, Microwave Laboratory Report No. 1816, Stanford University (1969).

67. W. D. Johnston, Jr., private communication.

68. R. R. Alfano, Appl. Optics $\underline{8}$, 2095 (1959)

69. S. E. Harris, Proc. IEEE $\underline{57}$, 2096 (1969).

70. Reference 42, Section 7.4.